Prediction Models of Inertial Particle Transport Using a Combined Lattice Boltzmann - Immersed Boundary Method

Original Citation:
Prediction Models of Inertial Particle Transport Using a Combined Lattice Boltzmann - Immersed Boundary Method / Ranaldo, Sergio. - ELETTRONICO. - (2019). [10.60576/poliba/iris/ranaldo-sergio_phd2019]

Availability:
This version is available at http://hdl.handle.net/11589/165747 since: 2019-03-13

Published version
DOI:10.60576/poliba/iris/ranaldo-sergio_phd2019

Publisher: Politecnico di Bari

Department of Mechanics, Mathematics and Management

MECHANICAL AND MANAGEMENT ENGINEERING

Ph. D. Program

SSD: ING-IND/06–FLUID DYNAMICS

Final dissertation

Prediction Models of Inertial Particle Transport Using a Combined Lattice Boltzmann - Immersed Boundary Method

---

by

Sergio Ranaldo

Referees:

Prof. Giacomo Falcucci

Phd Dott. Alessandro Coclite

Supervisors:

Prof. Giuseppe Pascazio

Coordinator of the Ph. D. Program:

Prof. Giuseppe Pompeo Demelio

Course n° 31, 01/11/2015-31/10/2018

Contents

List of Figures

Introduction

Low Reynolds number flows involve different fields of technical interest, such as flows confined to very small section ducts, or generally flows involving small geometries, such as those of interest in the biomedical field; or flows for which viscous forces have a dominant role as in the case of lubrication problems. Although the Navier-Stokes model is theoretically able to provide correct relations between the quantities of interest (fluid-dynamic variables), the solution of the problem using to this model presents different calculation difficulties. In fact, if non-stationary flows are taken into account, it can be shown that a low value of the Reynolds number implies considerable variations over time compared to spatial variations. Since, in general, a numerical algorithm is necessary to obtain a solution, this characteristic entails problems of stability and of computational costs, due to the need to accurately define the gradients in space and to a consequent adequate time step [1].

Among the alternative strategies, in the last two decades, the numerical technique based on the Boltzmann equation emerged as an effective alternative, particularly useful in the study of non-stationary flows of interest in the biological field [2], i.e. those for which the geometrical dimensions of the problem are very small.

Moreover, in this case, as shown in the first chapter, the same continuous model can be questioned. In fact, at very small scales the distance between the molecules constituting the fluid becomes sufficiently large, compared to the characteristic size of the problem, so that their mutual behavior can not be negletted; that is, the forces exchanged between them, in particular for their collisions, have to be modelled. In a numerical approach, spatial discretization implies distances between two neighboring points which, in the cases of interest in this thesis, must take into account these forces and their distribution, until the solution has physical confirmation.

With these considerations it can be said that many low Reynolds flows justify what is called *the mesoscopic approach* to the problem. It is placed in an intermediate position between the molecular dynamics, that is the description of the kinematic and dynamic behavior of the single molecules (position, trajectories, velocities and intermolecular forces) and the description based on the continuous fluid of the Navier-Stokes equations.

The model based on the Boltzmann equation provides a mesoscopic approach based on a probability density function, commonly called *distribution function.* Through a statistical description, it takes into account the local dynamic properties of the molecules and is subsequently linked to the macroscopic quantities of technical interest. The distribution function is the unknown of the equation and is defined in a space $\Re^3 \times \Re^3$ plus the time variable. Among the numerical methods proposed for the solution of the Boltzmann equation, suitable to the objectives of the present work, seems to be the Lattice-Boltzmann Method (LBM). It provides a spatial discretization with a Cartesian uniform mesh, the lattice, which has some advantages in setting the simulation. As described in chapter 3, the solver algorithm used is completely explicit; this feature, together with the lattice space discrtization, make the parallelization of

a code very simple and offer the possibility to divide the calculation on a large number of processors.
In the context of the low Reynolds number flows with small characteristic geometric dimension, the transport of nanoparticles and microparticles is a further technological topic. This is an unsteady problem that involves the study of the fluid structure interaction over time. In the biomedical field we remember the problems of drug delivery and the study of the behavior and interaction of membrane structures, such as cells and globules. In this work some methods are described for the study of low Reynolds number flows, involving the transport of rigid or deformable particles with the aim of carrying out three-dimensional simulations that are useful for understanding the influence of geometric parameters of the particles themselves and of the flow conditions. With this objective, a computational code with parallel capacities was developed, starting from a two-dimensional serial code, and validated through various tests. The original two-dimensional was in turn parallelized and used to carry out different simulations of scientific interest that contributed to the preparation of two publications.

The thesis develops in the following chapters:

1. Provides a theoretical basis of low Reynold number flows, gives a description of the mesoscopic approach up to the definition of the Boltzmann equation and to the description of its fundamental properties. It closes with the paragraphs that show the adherence to the continuous model, both in the case of the Euler and Navier-Stokes equations.

2. Describes the Lattice Boltzmann method used, the discretization of the terms of the Boltzmann equation and the quantities useful to carry out the correct simulations, both to respect the fluid-dynamic similitude and to avoid problems of stability of the chosen solver. The results of the classic lid driven cavity test are presented and compared with those published in the paper of Napolitano and Pascazio [40] in order to evaluate the fluid field solver.

3. Describes the immersed-boundary (IB) method implemented in the code useful to study the flow around particles. In the case of rigid bodies, the method offers the possibility of solving the equations of motion of the particles interacting with the flow. Two validation tests are presented with different geometries and flow conditions. Finally, the potentialities of parallelization of the algorithm are shown.

4. Describes the spring-network model used to consider deformations of membrane bodies containing fluid.
   A last three-dimensional test on the deformation of a capsule fill of fluid is presented and the results are compared with data available in the literature [53]. Finally, models and results of two-dimensional cases are described for which two papers have published.

Chapter 1

The Boltzmann Equation: Theory and Application to Low Reynolds Number Flows

1.1 Hints to the Kinetic Theory of Gases

The kinetic theory of gas [3] aims to describe the gas and some macroscopic properties through a microscopic statistical description, based on molecular properties. It is necessary to give a definition of physical system and some hypotheses at the basis of the dynamic properties of the system itself. With the term *gas* we indicate a set of molecules in random motion that occupy a volume V of arbitrary size, possibly limited by walls. We consider the following basic assumptions:

- The molecules interact through elastic collisions between themselves and with the boundary walls;
- The number of molecules N is so large that it is possible to define statiscal quantities;
- The average distance between the molecules is large compared to their linear size;
- The external forces and other interactions between the molecules are negligible.

With these hyphoteses it follows that there is no more likely position than another and that all the directions of the particles motion are equally probable. Consequently, the numeric density $\rho = N/V$ has to be considered uniform and also the momentum flux across a surface is therefore zero. However the average kinetic energy is not zero.

1.1.1 Average quantities and macroscopic quantities

The velocities and the momentum of the individual particles define some useful average quantities, among them it is important *the root Mean Square Velocity* defined as:

$$\left\langle v_{qm}^2 \right\rangle = \frac{1}{N} \sum_i \vec{v}_i^2 \tag{1.1}$$

where $\vec{v}_i$ is the velocity of *i-th* gas particle. From the hyphotesis of equal probability for the velocity direction derives that:

$$\left\langle v_{xi}^2 \right\rangle = \left\langle v_{yi}^2 \right\rangle = \left\langle v_{xi}^2 \right\rangle = \frac{1}{3} \left\langle v_{qm}^2 \right\rangle \tag{1.2}$$

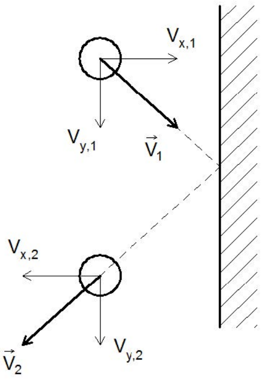

Figure 1.1: Pressure origin: particle impacting a wall

The quantity pressure p is correlated to the collisions of the gas molecules against the walls. In fact if we consider a cube of volume dv and of side dl containing the gas, and indicating with ds the generic wall, each molecule that elastically impacts the wall, bouncing, transfers to it a momentum in magnitude equal to $\Delta q_i = 2m|v_{dsi}|$, where v_{dsi} is the component of $\vec{v}_i$ normal to the wall ds (fig.1.1). The same gas particle impacts against the same wall after a time interval Δt_i necessary to travel twice the length of the cube side dl that contains it: $\Delta t_i = 2dl/|v_{dsi}|$.

The average force exerted by each individual molecule on the walls is given by:

$$\langle F_i \rangle = \left\langle \frac{\Delta q_i}{\Delta t_i} \right\rangle \tag{1.3}$$

$$\langle F \rangle = \sum_i \left\langle \frac{\Delta q_i}{\Delta t_i} \right\rangle \tag{1.4}$$

Since also for the normal direction must be $\left\langle v_{dsi}^2 \right\rangle = \frac{1}{3}\left\langle v_{qm}^2 \right\rangle$, then the total average force on each wall is:

$$\langle F \rangle = N \left\langle \frac{m v_{dsi}^2}{dl} \right\rangle = \frac{Nm\left\langle v_{qm}^2 \right\rangle}{3dl} \tag{1.5}$$

It is thus possible to write the pressure:

$$P = \langle F \rangle / ds = \langle F \rangle / dl^2 = \frac{Nm\left\langle v_{qm}^2 \right\rangle}{3dl^3} = \frac{Nm\left\langle v_{qm}^2 \right\rangle}{dV} = \frac{1}{3} m\rho \left\langle v_{qm}^2 \right\rangle \tag{1.6}$$

It is also possible to express internal energy as a function of the molecules' motion. With the assumptions made, it is linked only to kinetic energy. Considering we neglected external forces and other forces of interaction between the molecules and then forms of potential energy, and we considered point-like molecules, the energy due to the rotational or vibrational motion are not considered. So, for the internal energy U we can write:

$$U = \sum_i \frac{1}{2} mN \left\langle v_{qm}^2 \right\rangle = \frac{1}{2} m\rho V \left\langle v_{qm}^2 \right\rangle \tag{1.7}$$

1.2 The Mesoscopic Scale and the statistical approach

One can think of describing the gas state by calculating position and velocity of each single molecule; this involves the solution of the equations of motion:

$$\begin{aligned} \frac{d\vec{x}_i}{dt} &= \vec{v}_i, \qquad i = 1, \ldots, N \\ \frac{d\vec{v}_i}{dt} &= \frac{\vec{F}_i}{m_i},, \qquad i = 1, \ldots, N \end{aligned} \tag{1.8}$$

Equations (1.8) form a system of $6N$ differential equations, N being of the order of Avogadro's number for each mole of gas. This problem is difficult to solve not only for the number of equations but also for the uncertainty of the initial condition, which increases exponentially with respect to the number N and therefore would lead to an unacceptable error in the solution. It is therefore necessary to disengage from the identification of the individual particles and operate statistically in order to have an overall view sufficiently detailed but not particularly complex. For this purpose the objective becomes to know the distribution of particle velocities in volume and time in probabilistic terms, so that it also represents the density of them in the space. A probability density function f is then introduced, otherwise said *distribution function*, defined as the probability of finding a particle at a given time instant t, with a given velocity $\vec{v}$ and at a point $\vec{x}$ in the space, so $f = f(\vec{x}, \vec{v}, t)$. It is a function defined in the so called *Space of configurations* and in time [4]. Through the kinetic theory, this function allows to connect the microscopic description of the gas to the macroscopic one, obtaining the properties of practical interest. Through this definition it is possible to state that, having fixed a position $\vec{x}$ and a velocity $\vec{v}$, the number of molecules ΔN, present in a cube of $\Delta\vec{x}$ side, centered in $\vec{x}$, and having a velocity included in a dilated cube $\Delta\vec{v}$, side centered in $\vec{v}$ is:

$$\Delta N = Nf(\vec{x}, \vec{v}, t)\Delta\vec{x}\Delta\vec{v} \tag{1.9}$$

In the same way, considering the quantity $v = |\vec{v}|$, the probable number of molecules dN having speed between $\vec{v}$ e $\vec{v} + \vec{dv}$ is:

$$dN = Nf(\vec{x}, \vec{v}, t)d\vec{v} \tag{1.10}$$

The definition of distribution function can be seen as a connection between a microscopic environment, governed by the laws of molecular dynamic, and a macroscopic one, in which the gas is modeled by the continuum dynamic and its conservation laws such as the equation of Navier Stokes, the equations of state and the laws of thermodynamics. The two environments are distinguished by the different scales of length and time that must be taken into account in order to determine the physical quantities and the characteristic phenomena. About the microscopic scale, the lengths are of the order of the size of the molecules D_p, and the time intervals to be considered for the observation can be of the order of duration of the collision phenomenon, estimated by $t_c = D_p/v_{qm}$. On the other hand, the macroscopic scale is characterized by the length in which the gradients develop themselves and are interesting for their size. Typically this length is lower or grater, but comparable, with a geometric dimension L, characteristic of the fluid phenomenon under observation. About the time scale, it is necessary to evaluate if the fluid field is more influenced by inertial forces and pressure gradients or by viscous forces, in correspondence we can calculate the two time intervals $t_{conv} \sim L/u$ and $t_{diff} =\sim L^2/\nu$. The dimensionless number Re, the *Reynolds number*, defined by:

$$Re = \frac{uL}{\nu} = \frac{t_{diff}}{t_{conv}} \tag{1.11}$$

is an estimate of the relationship between the two time intervals. Low Reynolds numbers, for which the time scale is related to diffuse phenoena, are typical of microfluidic due to very low geometric dimensions. The kinetic theory and the distribution function aim to obtain the distribution of particles in a gas and their kinetic properties always in terms of distribution. The interest being in collection of particles, there is, indeed, no claim to track them individually. Then we place ourselves in a scale of length and in an intermediate time scale between the microscopic scale and the macroscopic one. It is called the mesoscopic scale. Because of the hypothesis of punctiform particles of negligible size in comparison with their mutual distance, it is possible to consider the lenght scale as the mean distance covered by a molecule between two succesive collision, called *mean free path* l_{mfp}. Since the duration of a collision can also be considered

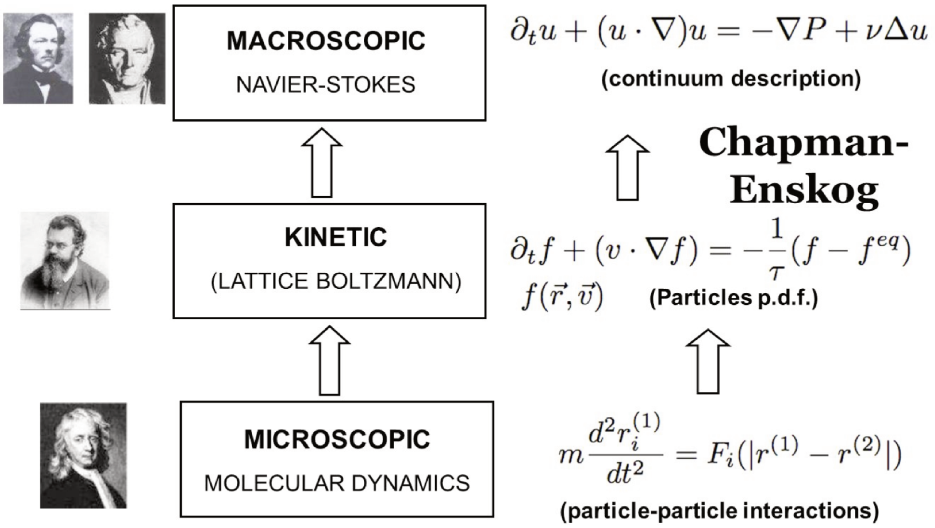

Figure 1.2: Molecular scale - Mesoscopic scale - Continuum scale

negligible, the time scale is the average time between two collisions *mean free time* t_{mfp}. In the case of microfluidics, the mean free path can be compared to the geometric dimension of the system and in this situation the mesoscopic scale is necessary, while the continuous macroscopic model may be insufficient. About this observation, the *Knudsen* dimensionless number is an important useful parameter:

$$Kn = \frac{l_{mfp}}{L} \tag{1.12}$$

With $Kn \sim 1$ is necessary to switch to mesoscopic scale, and use distribution function to describe the problem. Fig. 1.2 shows the three possible points of view to study a gas, one of their basic equations, and the scale in which they hold.

1.3 Distribution function - definition and properties

Given a volume of gas in motion with average velocity $\vec{u}$, we indicate with $\vec{\xi}$ the absolute velocity of the generic molecule and with $\vec{v}$ the velocity of the molecule relative to $\vec{u}$, so that $\vec{\xi} = \vec{u} + \vec{v}$, therefore the definitions and properties seen in the previous section are valid. The mesoscopic approach involves the definition of a probability distribution that can represent the state of fluid in space and time. With this purpose, we have introduced a function $f(\vec{x}, \vec{\xi}, t)$. As shown in the above sections it also can be seen as a generalized density measuring the number of particles for unit volume, both in geometric and velocity space, with a prescribed velocity $\vec{\xi}$, in a space point $\vec{x}$ at time t. According to the definition above, $f(\vec{x}, \vec{\xi}, t)\dot{d}\xi$ is the number of particles with a velocity between $\vec{\xi}$ and $\vec{\xi} + d\vec{\xi}$. Furthermore, $f(\vec{x}, \vec{\xi}, t) \cdot d\vec{\xi} d\vec{x}$ equals the mass of particles with a velocity between $\vec{\xi}$ and $\xi + d\vec{\xi}$ in the elementary volume $d\vec{x}$ at time t. Integrating f over the entire velocity field we find the number of particles in the point $\vec{x}$, *i.e.* the local flow density:

$$\rho(\vec{x}, t) = \int f(\vec{x}, \vec{\xi}, t) d\vec{\xi} \tag{1.13}$$

In similar way, by means of integration, we can find all the physical properties describing the local state of fluid, thus connecting the mesoscopic and macroscopic representations. These integrals, involving the distribution function f weighted by 1, $\vec{\xi}$, $\vec{\xi}^2/2$, are named *moments of f*. The first of them is the one just written, generally called *density.*

The quantity $\xi f(\vec{x}, \vec{\xi}, t) d\vec{\xi}$, is the *momentum density*, of particles within a certain infinitesimal velocity range. The *total momentum density* is obtained integrating over all velocities:

$$\rho u(\vec{x}, t) = \int \xi f(\vec{x}, \vec{\xi}, t) d\vec{\xi} \tag{1.14}$$

where $\vec{u}$ is the particles' average velocity, namely, the macroscopic *fluid velocity.*

In the same way multiplying $f(\vec{x}, \vec{\xi}, t)$ by $\xi^2/2$ and integrating, the *energy density* is defined:

$$\rho E(\vec{x}, t) = \frac{1}{2} \int |\xi|^2 f(\vec{x}, \vec{\xi}, t) d\vec{\xi} \tag{1.15}$$

The quantity E is defined *specific energy.*

For the hypothesis of spherical particles, the internal energy is due only to their translational motion, and we can also divide it into two terms. The first one is related to the global average velocity $\vec{u}$ (fluid velocity):

$$\frac{1}{2} \rho u^2 \tag{1.16}$$

The second one depends on the random motion of the particles, the *internal energy density ρe*, with quantity e called *specific internal energy.* It follows that:

$$\rho E = \rho(e + \frac{1}{2} u^2) \tag{1.17}$$

It can be observed that relative velocity $\vec{v}$ does not contribute to the momentum:

$$\int \vec{v} f d\vec{\xi} = \int (\vec{\xi} - \vec{u}) f d\vec{\xi} = \int \vec{\xi} f d\vec{\xi} - \int \vec{u} f d\vec{\xi} = \int \vec{\xi} f d\vec{\xi} - \vec{u} \int f d\vec{\xi} = \rho \vec{u} - \rho \vec{u} = 0 \tag{1.18}$$

Using this observation we can rewrite the energy density:

$$\begin{aligned} &\rho E(\vec{x}, t) = \frac{1}{2} \int (\vec{v} + \vec{u}) \cdot (\vec{v} + \vec{u}) f(\vec{x}, \vec{\xi}, t) d\vec{\xi} = \\ &\frac{1}{2} \int |v|^2 f(\vec{x}, \vec{\xi}, t) d\vec{\xi} + \vec{u} \cdot \int \vec{v} f(\vec{x}, \vec{\xi}, t) d\vec{\xi} + \frac{1}{2} u^2 \int f(\vec{x}, \vec{\xi}, t) d\vec{\xi} \implies \end{aligned}$$

$$\rho E(\vec{x},t) = \frac{1}{2}\int |v|^2 f(\vec{x},\vec{\xi},t)d\vec{\xi} + \frac{1}{2}\rho u^2 \tag{1.19}$$

With this relation and equation (1.17) it is possible to find the moment equation for *internal energy density*:

$$\rho e(\vec{x},t) = \frac{1}{2}\int |v|^2 f(\vec{x},\vec{\xi},t)d\vec{\xi} \tag{1.20}$$

1.4 Pressure, Temperature, and Heat Capacities in terms of Distribution Function

A relationship linking the pressure to the velocity square root has been shown, now it is also possible to find a relationship in terms of the distribution function. With this purpose, let a volume of gas with a zero average velocity, hypothesis not strictly necessary, but useful to shorten the calculations; Assume a Cartesian reference framem and a wall having normal x. Here, another hypothesis is that each velocity direction is equally probable; this is equivalent to assume that the distribution function is spherically symmetrical around $\vec{v} = 0$. Place dA = dydz, for an infinitesimal period dt, the total mass of particles having a particular velocity $\vec{\xi_i}$ is given by:

$$f(\vec{x},\vec{\xi},t)d\vec{\xi}d\vec{x}$$

If $d\vec{x} = dxdydz$ and the velocity component normal to wall is ξ_x, so that $d\vec{x} = \xi_x dtdydz$, and the total mass impacting against the wall is:

$$\xi_x f(\vec{x},\vec{\xi},t)d\vec{\xi}dtdydz$$

As previously seen, it has to be considered a velocity change of $2\xi_x$ to find the momentum change due to the wall, thus the force due to the molecules having velocity $\vec{\xi}$ is:

$$F_\xi = \frac{2\xi_x \cdot \xi_x f(\vec{x},\vec{\xi},t)d\vec{\xi}dtdydz}{dt} = 2\xi_x^2 f(\vec{x},\vec{\xi},t)d\vec{\xi}dydz \tag{1.21}$$

To find the total force exchanged by all particles we have to integrate equation (1.21) over all velocities that cause a collision, i.e. those for which $\xi_x > 0$. However, since f was assumed to be spherically symmetrical, we can consider all the velocities in the integration and divide by 2. So the total force on the wall and the related pressure are:

$$F = dydz\int \xi_x^2 f(\vec{x},\vec{\xi},t)d\vec{\xi}$$

$$p = \int \xi_x^2 f(\vec{x},\vec{\xi},t)d\vec{\xi}$$

Again because of f symmetry $\xi_x^2 = \frac{1}{3}\xi^2$, the pressure is:

$$p = \frac{1}{3}\int \xi^2 f(\vec{x},\vec{\xi},t)d\vec{\xi}$$

Also with the hypothesis of average gas velocity $u = 0$, it follows that $\vec{\xi} = \vec{v}$ and the pressure can be written:

$$p = \frac{1}{3}\int v^2 f(\vec{x},\vec{\xi},t)d\vec{\xi} = \frac{2}{3}\rho e \tag{1.22}$$

In addition to a relationship with the distribution function, an equation between pressure, density and specific internal energy has been obtained. It is an equation of state, that is possible to compare with the ideal gas law:

$$p = \rho RT = \rho\frac{K_B T}{m} \tag{1.23}$$

where $R = \frac{K_B T}{m}$ is the *specific gas constant*, T is the *temperature* and K_B is the *Boltzmann constant.* Comparing equations (1.22) and (1.23), one has:

$$\frac{2}{3}\rho e = \rho \frac{K_B T}{m} \quad \Longrightarrow e = \frac{3}{2}\frac{K_B T}{m} \tag{1.24}$$

In equation (1.24) the relation between specific energy and gas temperature is given. It is possible to calculate the *spcific heat capacity at constant volume* c_v and the *specific heat capacity at constant pressure* c_p:

$$C_v = \left(\frac{\partial e}{\partial T}\right)_V = \frac{3}{2}R = \frac{3}{2}\frac{K_B}{m} \tag{1.25}$$

For an ideal gas it is worth:

$$\begin{aligned} C_p - C_v = R = \frac{K_b}{m} \implies \\ C_p = \frac{5}{2}R = \frac{5}{2}\frac{K_B}{m} \end{aligned} \tag{1.26}$$

The ratio from the two capacities is often useful. For the monoatomic gas in this treatment it becomes:

$$\gamma = \frac{c_p}{c_V} = \frac{5}{3} \tag{1.27}$$

1.5 Distribution function and equilibrium

If a volume of gas with a certain initial distribution function is allowed to evolve for a sufficient time without external interactions, after a certain number of collisions it is possible to suppose that the molecules velocities are distributed in all directions around the velocity average $\vec{u}$. This situation could seen as an equilibrium state.

At equilibrium the distribution function, indicated as f^{eq}, depends on the relative velocity $\vec{v}$, with more precision the equality of f^{eq} for all directions implies that it depends only on the magnitude of $\vec{v}$, $f^{eq} = f^{eq}(|v|)$. With the aim of finding a relationship for the equilibrium distribution function, we consider the hypothesis that it assumes a separable form in the coordinates of $\vec{v}$:

$$f^{eq}(|v|) = f^{eq}(v_x)f^{eq}(v_y)f^{eq}(v_z)$$

For a constant $|v|$, also f^{eq} is constant and:

$$\ln f^{eq}(|v|) = \ln f^{eq}(v_x) + \ln f^{eq}(v_y) + \ln f^{eq}(v_z) = \text{const.}$$

This is possible only if:

$$\begin{aligned} \ln f^{eq}(v_x) = a - bv_x^2 = \\ \ln f^{eq}(v_y) = a - bv_y^2 = \\ \ln f^{eq}(v_z) = a - bv_z^2 \end{aligned}$$

with a e b constants not depending on $\vec{v}$. From this set of equation:

$$\ln f^{eq}(|v|) = 3a - b(v_x^2 + v_y^2 + v_z^2) = 3a - bv^2 \implies f^{eq}(|v|) = e^{3a}e^{-bv^2} \tag{1.28}$$

The constants a e b can be obtained by considering the moments of f^{eq}. Starting with density moment:

$$\rho = \int f^{eq}(|v|)d\xi = e^{3a}\int_{-\infty}^{\infty} e^{-bv_x^2}dv_x \int_{-\infty}^{\infty} e^{-bv_y^2}dv_y \int_{-\infty}^{\infty} e^{-bv_z^2}dv_z = e^{3a}(\frac{\pi}{b})^{\frac{3}{2}} \implies e^{3a} = \rho(\frac{b}{\pi})^{\frac{3}{2}}$$

The distribution function at equilibrium is:

$$f^{eq}(|v|) = \rho \left(\frac{b}{\pi}\right)^{\frac{3}{2}} e^{-bv^2} \tag{1.29}$$

Then is possible to obtain b from energy moment:

$$\rho e(\vec{x}, t) = \frac{1}{2} \int |v|^2 f^{eq}(|v|) d\vec{\xi}$$

Because of its spherical symmetry, f^{eq} is constant on spherical surface centered in $\vec{v} = 0$ and it is possible to substitute $d\vec{\xi}$ with $4\pi|v| \cdot |v|d|v| = 4\pi|v|^2 d|v|$ and to integrate on $|v|$ varying from 0 to $+\infty$:

$$\rho e(\vec{x}, t) = \frac{1}{2} \int_0^\infty |v|^2 f^{eq}(|v|) 4\pi|v|^2 d|v| = \frac{1}{2} \cdot 4\pi\rho \left(\frac{b}{\pi}\right)^{\frac{3}{2}} \int_0^\infty |v|^4 e^{-bv^2} d|v|$$

Recalling that:

$$\int_{-\infty}^\infty x^4 e^{-x^2} dx = \frac{3\sqrt{\pi}}{4}$$

after few algebraic passages the result is:

$$\rho e = \frac{3\rho}{4b} \implies b = \frac{3}{4e} = \frac{m}{2K_B T} \tag{1.30}$$

Substituting this expression in equation (1.28) for f^{eq}:

$$f^{eq}(|v|) = \rho \left(\frac{3}{4\pi e}\right)^{\frac{3}{2}} e^{-3|v|^2/4e} = \rho \left(\frac{\rho}{2\pi p}\right)^{\frac{3}{2}} e^{-\rho|v|^2/2p} = \rho \left(\frac{m}{2\pi K_B T}\right)^{\frac{3}{2}} e^{-m|v|^2/2K_B T} \tag{1.31}$$

This expression is called *Maxwell-Boltzmann distribution.* His behaviour, for three different values of temperature, is shown in fig. 1.3

Now it is possible to define the moments of distribution function at equilibrium. They are obtained, at different order, progressively weighting the integral with the vector $\vec{v}_i$ $i = 1, \ldots, n$, the results are tensors of $i - th$ order.

Starting with the zero order moment, it is the density:

$$\rho = \int f^{eq} d\vec{\xi} \tag{1.32}$$

For the first order, it is defined as for the general distribution function, but it is null:

$$\int v_1 f^{eq} d\vec{\xi} = 0 \tag{1.33}$$

This result is the same for all the odd order terms. In fact because of the symmetry of f^{eq} and the central symmetry of $\vec{v}_i$ around $\vec{v} = \vec{0}$ the integrand tensor in these cases is zero.

So the 2th order and 4th order tensors are written below.

$$\int v_1 v_2 f^{eq} d\xi = \frac{\rho}{2b} \delta_{12} \tag{1.34}$$

where δ_{12} is the second order tensor in which the generic element is given by the Kronecker delta.

$$\int v_1 v_2 v_3 v_4 f^{eq} d\xi = \frac{\rho}{2b^2} (\delta_{12}\delta_{34} + \delta_{13}\delta_{24} + \delta_{14}\delta_{23}) \tag{1.35}$$

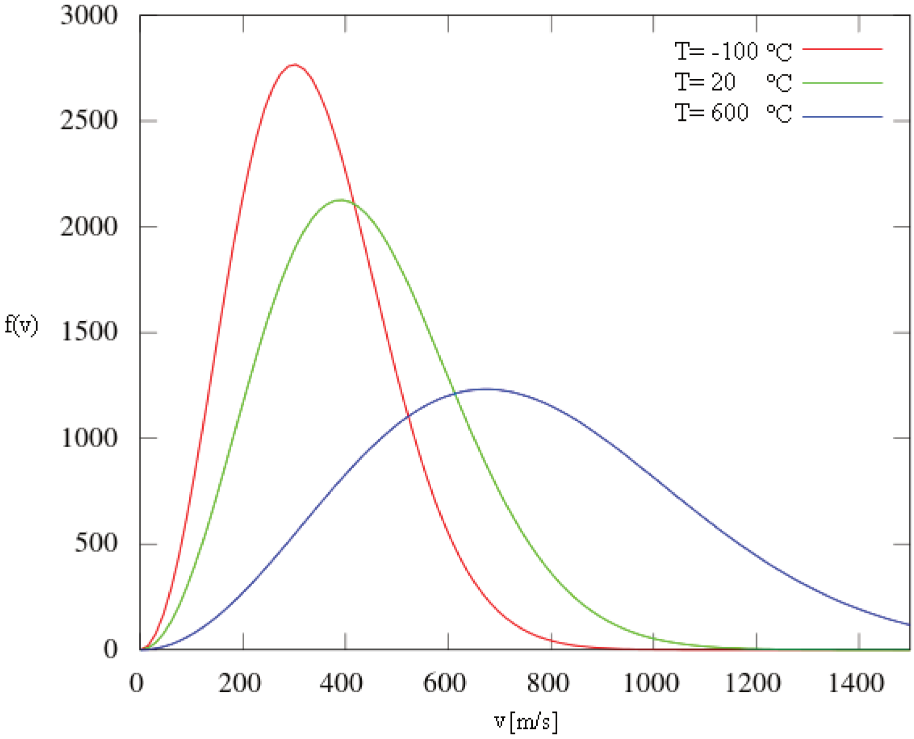

Figure 1.3: Maxwell-Boltzmann distribution function

1.6 The Boltzmann Equation

Given an elementary volume of gas $d\vec{x}d\vec{\xi}$, with the hypothesis of absence of collisions, the global number of particles dN has to be constant, it is possible to write:

$$f(\vec{x}+d\vec{x},\vec{\xi}+d\vec{\xi},t+dt)d\vec{x}d\vec{v}=f(\vec{x},\vec{\xi},t)d\vec{x}d\vec{v}$$

Dividing by $d\vec{x}d\vec{v}dt$ the total derivative of f is obtained and it is equal to zero:

$$\frac{df}{dt}=0$$

$$\frac{df}{dt}=\frac{\partial f}{\partial t}+\frac{\partial f}{\partial x}\frac{dx}{dt}+\frac{\partial f}{\partial y}\frac{dy}{dt}+\frac{\partial f}{\partial z}\frac{dz}{dt}+\frac{\partial f}{\partial \xi_x}\frac{\partial \xi_x}{dt}+\frac{\partial f}{\partial \xi_y}\frac{\partial \xi_y}{dt}+\frac{\partial f}{\partial \xi_z}\frac{\partial \xi_z}{dt}\implies$$

$$\frac{df}{dt}=\frac{\partial f}{\partial t}+\frac{d\vec{x}}{dt}\nabla f+\frac{d\vec{\xi}}{dt}\nabla_\xi f$$

From cinematic definition of velocity particles:

$$\vec{\xi}=\frac{d\vec{x}}{dt}$$

and from second Newton's law:

$$\frac{d\vec{\xi}}{dt}=\frac{\vec{F}}{\rho}$$

So, the following equation describes the evolution of the distribution function f in the absence of collisons:

$$\frac{\partial f}{\partial t}+\vec{\xi}\cdot\nabla f+\frac{F_1}{\rho}\cdot\nabla_\xi f=0 \tag{1.36}$$

In the presence of collisions it is not possible to state that the global number of molecules in the elementary volume $d\vec{x}d\vec{\xi}$ remains constant, because the interacting molecules may change direction and significantly modify the velocity vector $\vec{\xi}$ associated with them. The number and effects of collisions depend on the same distribution function calculated at a certain time t and at a point in space $\vec{x}$ but for all the velocities $\vec{\xi}$. It follows that a collision operator $\Omega(f)$ can be introduced into the evolution equation of f. The *Boltzmann Equation* is obtained:

$$\frac{\partial f}{\partial t} + \vec{\xi} \cdot \nabla f + \frac{\vec{F}}{\rho} \cdot \nabla_{\xi} f = \Omega(f) \tag{1.37}$$

Alternatively with compact notation:

$$\frac{\partial f}{\partial t} + \xi_1 \frac{\partial f}{\partial x_1} + \frac{\vec{F}}{\rho} \frac{\partial f}{\partial \xi_1} = \Omega(f) \tag{1.38}$$

1.7 The collision operator

To simplify the notation, we consider the case of average veocity $\vec{u}$ equal to zero so that the speed $\vec{\xi}$ is equal to $\vec{v}$. The distribution function varies over time through collisions, involving two modes of variation:

- particles with velocity $\vec{v}$ can be diffused at a different velocity $\vec{v}'$, in this case $f(\vec{x}, \vec{v}, t)$ decreases;
- particles with velocity $\vec{v}'$ assume velocity $\vec{v}$, with an increment of $f(\vec{x}, \vec{v}, t)$.

With these obseravations it's possible to write:

$$\frac{Df}{Dt} = -\Psi_{out} + \Psi_{in} \tag{1.39}$$

Let n be the spatial numerical density of the particles and r their radius, in the conditions of rarefied gas, is possible to write:

$$na^3 << 1$$

The particles occupy a negligible volume and move freely except when they are at a distance $2a$ and collide. The distance between two successive collisions λ is defined as *mean free path.* It is possible to prove that for rigid spherical particles it is equal to:

$$\lambda = \frac{1}{\sqrt{2}\pi a^2 n} \tag{1.40}$$

In the rarefied gas $\lambda >> a$ and even the probability of having collisions with more than two particles is totally negligible. We consider two colliding particles with velocities $\vec{v}$ and $\vec{v_1}$, in the elastic collisions the momentum and the kinetic energy are conserved before and after the impact, so indicating with $\vec{v}'$ and $\vec{v}_1'$ the velocities before and after the collision:

$$\vec{v} + \vec{v}_1 = \vec{v}' + \vec{v}_1'$$

$$\frac{1}{2}\vec{v}^2 + \frac{1}{2}\vec{v}_1^2 = \frac{1}{2}\vec{v}'^2 + \frac{1}{2}\vec{v}_1'^2$$

To obtain $\vec{v}'$ and $\vec{v}_1'$ two other conditions are necessary. One of them is given by the observation that central forces involve flat collisions, a second one is obtained by explaining the interaction potential that determines the trajectory after the impact. However, it is possible to operate without describing the potential and considering instead what is called *differential cross section.*

Consider a set of particles with velocity $\vec{v}_1$ and density δn_1 colliding with a second set with velocity $\vec{v}$ and density δn. A particle of the second set meets the flux $\phi = |\vec{v} - \vec{v}'|\delta n_1$ of particles of the first set. The number of collisions which diffuse the particles of the second set δn_c into a solid angle $d\theta$ is proportional to the number of particles of the second set, to the particle flow of the first and to the amplitude of the solid angle itself. The *differential cross section* is the proportionality factor, indicated with $d\sigma/d\theta$, and is a function of $\vec{v}$,$\vec{v}'$,$\vec{v}_1$,$\vec{v}_1'$.

$$\delta n_c = \frac{d\sigma}{d\theta}(\vec{v}, \vec{v}_1 \rightarrow \vec{v}', \vec{v}_1')\delta n|\vec{v} - \vec{v}'|\delta n_1 d\theta \tag{1.41}$$

With the aim of evaluating the terms Ψ_{in} and Ψ_{out}, the δn and δn_1 sets must be written according to the distribution function:

$$\delta n = f(\vec{x}, \vec{v}, t)d\vec{v}$$

$$\delta n_1 = f(\vec{x}, \vec{v}_1, t)d\vec{v}_1$$

Substituting these expressions in equation (1.41):

$$\delta n_c = \frac{d\sigma}{d\theta}(\vec{v}, \vec{v}_1 \rightarrow \vec{v}', \vec{v}_1')|\vec{v} - \vec{v}_1| f(\vec{x}, \vec{v}_1, t) f(\vec{x}, \vec{v}, t) d\theta d\vec{v} d\vec{v_1} \tag{1.42}$$

To obtain all the collisions in the volume $d\vec{x}d\vec{v}$ that scatter particles of the set δn out of velocity $\vec{v}$ must be added together, all possible deflections $d\theta$ on all velocities of various sets δn_1, for which we obtain:

$$\Psi_{out} = d\vec{x}d\vec{v} \int d\vec{v}_1 \int d\theta \frac{d\sigma}{d\theta}(\vec{v}, \vec{v}_1 \rightarrow \vec{v}', \vec{v}_1')|\vec{v} - \vec{v}_1| f(\vec{x}, \vec{v}_1, t) f(\vec{x}, \vec{v}, t) \tag{1.43}$$

A similar argument can be made for the particles of a $\delta n'$ set which instead acquire the velocity $\vec{v}$ after impact, striking those of a $\delta n_1'$ set:

$$\delta n_c' = \frac{d\sigma}{d\theta}(\vec{v}', \vec{v}_1' \rightarrow \vec{v}, \vec{v}_1)|\vec{v}' - \vec{v}_1'| f(\vec{x}, \vec{v}_1', t) f(\vec{x}, \vec{v}', t) d\theta d\vec{v}' d\vec{v}_1' \tag{1.44}$$

Considering that the elastic collisions between spherical particles are reversible (hypothesis that allowed to write conservation of momentum and energy), we can write for the term $d\sigma/d\theta$:

$$\frac{d\sigma}{d\theta}(\vec{v}, \vec{v}_1 \rightarrow \vec{v}', \vec{v}_1') = \frac{d\sigma}{d\theta}(\vec{v}', \vec{v}_1' \rightarrow \vec{v}, \vec{v}_1) \tag{1.45}$$

Also for conservation laws:

$$|\vec{v} - \vec{v}_1| = |\vec{v}' - \vec{v}_1'| \tag{1.46}$$

$$d\vec{v}' d\vec{v_1}' = d\vec{v} d\vec{v_1} \tag{1.47}$$

It follows that:

$$\Psi_{in} = d\vec{x}d\vec{v}_1 \int d\vec{v} \int d\theta \frac{d\sigma}{d\theta}(\vec{v}', \vec{v}_1' \rightarrow \vec{v}, \vec{v}_1)|\vec{v}' - \vec{v}_1'| f(\vec{x}, \vec{v}_1', t) f(\vec{x}, \vec{v}', t)$$

Using equations (1.46) and (1.47), Ψ_{in} becomes:

$$\Psi_{in} = d\vec{x}d\vec{v} \int d\vec{v}_1 \int d\theta \frac{d\sigma}{d\theta}(\vec{v}, \vec{v}_1 \rightarrow \vec{v}', \vec{v}_1')|\vec{v} - \vec{v}_1| f(\vec{x}, \vec{v}_1', t) f(\vec{x}, \vec{v}', t) \tag{1.48}$$

The *collision operator* or *collision integral* or *collision term* of the Boltzmann equation can be now written:

$$\Omega(f) = \frac{\partial f}{\partial t}_{coll} = \int d\vec{v}_1 \int d\theta \frac{d\sigma}{d\theta}|\vec{v} - \vec{v}_1|[f(\vec{x}, \vec{v}_1', t) f(\vec{x}, \vec{v}', t) - f(\vec{x}, \vec{v}_1, t) f(\vec{x}, \vec{v}, t)] \tag{1.49}$$

1.7.1 Collisional Invariants and Properties of the collision operator

The quantities conserved in the elastic binary collisions determine the *collisional invariants.* A collisional invariant is defined as a function $\chi(\vec{v})$ such that the integral over all velocities space of the function multiplied by the collision term must be zero:

$$\int \frac{\partial f}{\partial t}_{coll} \chi d\vec{v} = 0 \tag{1.50}$$

The integral is zero if $\chi(\vec{v})$ is one of the function:

$$\begin{cases} \chi = 1 \\ \chi = m \cdot \vec{v} \\ \chi = m \cdot \frac{v^2}{2} \end{cases}$$

The same is valid if the function is a linear combination of the above. With the aim to prove these properties for the conserved quantities, consider a generic function $\chi(\vec{v})$, the integral on velocity field is:

$$\int \chi(\vec{v})[f'f_1' - ff_1]|\vec{v}-\vec{v}_1|\frac{d\sigma}{d\theta}d\theta d\vec{v}d\vec{v}_1 \tag{1.51}$$

For elastic collisions the integral does not change by exchanging $\vec{v}$ and $\vec{v}_1$, and it is valid:

$$\int \chi(\vec{v})[f'f_1' - ff_1]|\vec{v}-\vec{v}_1|\frac{d\sigma}{d\theta}d\theta d\vec{v}d\vec{v}_1 = \int \chi(\vec{v}_1)[f'f_1' - ff_1]|\vec{v}-\vec{v}_1|\frac{d\sigma}{d\theta}d\theta d\vec{v}d\vec{v}_1$$

The same integral is written for the set with velocity $\vec{v}'$ and $\vec{v}_1'$:

$$\int \chi(\vec{v}')[ff_1 - f'f_1']|\vec{v}'-\vec{v}_1'|\left[\frac{d\sigma}{d\theta}d\theta\right]' d\vec{v}'d\vec{v}_1'$$

As seen in the previous section $|\vec{v}-\vec{v}_1| = |\vec{v}'-\vec{v}_1'|$ and $d\vec{v}'d\vec{v}_1{}' = d\vec{v}d\vec{v}_1$, and moreover for binary collisions it also must be:

$$\left[\frac{d\sigma}{d\theta}d\theta\right]' = \frac{d\sigma}{d\theta}d\theta$$

So the following equalities are valid:

$$\int \chi(\vec{v}')[ff_1 - f'f_1']|\vec{v}'-\vec{v}_1'|\left[\frac{d\sigma}{d\theta}d\theta\right]' d\vec{v}'d\vec{v}_1' = -\int \chi(\vec{v})[f'f_1' - ff_1]|\vec{v}-\vec{v}_1|\frac{d\sigma}{d\theta}d\theta d\vec{v}d\vec{v}_1$$

$$\int \chi(\vec{v}_1')[ff_1 - f'f_1']|\vec{v}'-\vec{v}_1'|\left[\frac{d\sigma}{d\theta}d\theta\right]' d\vec{v}'d\vec{v}_1' = -\int \chi(\vec{v}_1')[f'f_1' - ff_1]|\vec{v}-\vec{v}_1|\frac{d\sigma}{d\theta}d\theta d\vec{v}d\vec{v}_1$$

Wanting to evaluate the integral you can take advantage of the equalities and add it 4 times:

$$4\cdot\int \chi(\vec{v})[f'f_1' - ff_1]|\vec{v}-\vec{v}_1|\frac{d\sigma}{d\theta}d\theta d\vec{v}d\vec{v}_1 = \int \left[\chi(\vec{v}) + \chi(\vec{v}_1) - \chi(\vec{v}') - \chi(\vec{v}_1')\right][f'f_1' - ff_1]|\vec{v}-\vec{v}_1|\frac{d\sigma}{d\theta}d\theta d\vec{v}d\vec{v}_1$$

Always considering the situation of elastic collision, if the function $\chi(\vec{v})$ is one of the quantities conserved in the collision, it must be:

$$\chi(\vec{v}) + \chi(\vec{v}_1) - \chi(\vec{v}') - \chi(\vec{v}_1') = 0$$

So in this case the integral is zero and the function is a collisional invariant. In addition to the invariants linked to the characteristics of elastic collisions, another property that must have the collision term is that the distribution function in its evolution can not have a negative sign so as to have a physical meaning, $f(\vec{x},\vec{v},t) > 0$. It is possible to show this considering an initial state and a point $(\vec{x},\vec{v})$ of minimum for f, in which $f = 0$. For a minimum point it is:

$$\nabla f = 0; \quad \nabla_\xi f = 0$$

In this case the Boltzmann equation becomes:

$$\frac{\partial f}{\partial t} = \int d\vec{v}_1 \int d\theta \frac{d\sigma}{d\theta}|\vec{v}-\vec{v}_1|[f(\vec{x},\vec{v}_1',t)f(\vec{x},\vec{v}',t)]$$

But the right hand side is always positive, this implies that f can not decrease and therefore become negative. Yet, the collision term, as it was written, may show what is known as *the H-theorem*: Let functional $H(t)$:

$$H(t) = \int f ln f d\vec{v} \tag{1.52}$$

it is:

$$\frac{dH}{dt} \leq 0 \tag{1.53}$$

We restrict the case of homogeneous gas ($\nabla f = 0$)in the absence of external forces, again the Boltzmann equation gives:

$$\frac{\partial f}{\partial t} = \Omega(t)$$

Let consider the derivative of H:

$$\frac{dH}{dt} = \int (1 + lnf)\frac{\partial f}{\partial t} d\vec{v}$$

We explicate the collision term and place $\chi(\vec{v}) = 1 + lnf$, we have:

$$\frac{dH}{dt} = \int (1 + lnf)[f'f'_1 - ff_1]|\vec{v} - \vec{v}_1|\frac{d\sigma}{d\theta} d\theta d\vec{v} d\vec{v}_1$$

Evaluating the integral as seen above for collision invariants:

$$\frac{dH}{dt} = \frac{1}{4}\int (1 + lnf + 1 + lnf_1 - 1 - lnf' - 1 - lnf'_1)[f'f'_1 - ff_1]|\vec{v} - \vec{v}_1|\frac{d\sigma}{d\theta} d\theta d\vec{v} d\vec{v}_1 =$$

$$= \frac{1}{4}\int \left\{ ln\left[\frac{ff_1}{f'f'_1}\right][f'f'_1 - ff_1]\right\}|\vec{v} - \vec{v}_1|\frac{d\sigma}{d\theta} d\theta d\vec{v} d\vec{v}_1$$

The term $ln(ff_1/f'f'_1)[f'f'_1 - ff_1]$ is less or equal to zero, infact if we place $a = ff_1 > 0$ and $b = f'f'_1 > 0$ (because $f > 0$ in any case), we note that, the term is always negative if $a > b$ or $b > a$, and it is equal to zero only if $a = b$. So the integral is negative as dH/dt.

1.8 Macroscopic conservation equation

Considering the moments Boltzmann Equation terms is possible to find general conservation equation for the collision invatiants mass, momentum, and energy.

For the moments of f, a compact notation is now introduced:

$$\begin{aligned} M_0 &= \int f d\vec{\xi} = \rho \\ M_1 &= \int \xi_1 f d\vec{\xi} = \rho u_1 \\ M_{12} &= \int \xi_1\xi_2 f d\vec{\xi} = \rho u_1 u_2 - \int v_1 v_2 f d\vec{\xi} \\ M_{123} &= \int \xi_1\xi_2\xi_3 f d\vec{\xi} \end{aligned} \tag{1.54}$$

For force term, other useful momentum integrals involve derivative $\partial f/\partial \xi_1$:

$$\begin{aligned} &\int \frac{\partial f}{\partial \xi_1} d\vec{\xi} \\ &\int \xi_1 \frac{\partial f}{\partial \xi_2} d\vec{\xi} \\ &\int \xi_1\xi_1 \frac{\partial f}{\partial \xi_2} d\vec{\xi} \end{aligned}$$

Using the integration by parts, and considering that the integration surface would be for $|\vec{v}| \to \infty$, where it is possible to state that f is null with its derivatives, as well as the products $\xi_1 f$ and $\xi_1\xi_1 f$. So it is:

$$\begin{aligned} &\int \frac{\partial f}{\partial \xi_1} d\vec{\xi} = 0 \\ &\int \xi_1 \frac{\partial f}{\partial \xi_2} d\vec{\xi} = -\int \frac{\partial \xi_1}{\partial \xi_2} f d\vec{\xi} = -\rho\delta_{12} \\ &\int \xi_1\xi_1 \frac{\partial f}{\partial \xi_2} d\vec{\xi} = -\int \frac{\partial \xi_1\xi_1}{\partial \xi_2} f d\vec{\xi} = -2\rho u_2 \end{aligned} \tag{1.55}$$

1.8.1 Mass conservation

For all the terms of the Boltzmann equation, let's consider the zero order moment:

$$\frac{\partial}{\partial t}\int f d\vec{\xi}+\frac{\partial}{\partial x_1}\int \vec{\xi}_1 f d\vec{\xi}+\frac{\vec{F}_1}{\rho}\int \frac{\partial f}{\partial \xi_1}d\vec{\xi}=\int \Omega(f)d\vec{\xi}$$

The Integral on the left hand side is the first collisional invariant; on the right hand side the terms are:

- First is the partial time derivative of density;
- Second is the spazial derivative of momentum;
- Third term is zero as seen above.

So the equation becomes:

$$\frac{\partial \rho}{\partial t}+\frac{\partial \rho u_1}{\partial x_1}=0 \tag{1.56}$$

This is the *continuity equation.*

1.8.2 Momentum conservation

Considering the first moment for the terms of the Boltzmann Equation:

$$\frac{\partial}{\partial t}\int \xi_1 f d\vec{\xi}+\frac{\partial}{\partial x_2}\int \vec{\xi}_1\vec{\xi}_2 f d\vec{\xi}+\frac{\vec{F}_2}{\rho}\int \xi_1\frac{\partial f}{\partial \xi_2}d\vec{\xi}=\int \xi_1\Omega(f)d\vec{\xi}$$

Also here the Left hand side is zero because is the second collisional invariant. For the right hand side:

- The first Term is the partial time derivative of momentum;
- The second term is spazial derivative of M_{12};
- The third term is:

$$-\frac{F_2}{\rho}\rho\delta_{12}=-F_2\delta_{12}=-F_1$$

Replacing in the equation:

$$\frac{\partial \rho u_1}{\partial t}+\frac{\partial \rho u_1 u_2}{\partial x_2}=F_1-\frac{\int v_1 v_2 f d\vec{\xi}}{\partial x_2} \tag{1.57}$$

The equation can be recognized as the *momentum equation* considering that the term:

$$-\int v_1 v_2 f d\vec{\xi} \tag{1.58}$$

represents a diffusive term analogous to the *Cauchy stress tensor*, and is indicated below with ST. This result is the subject of a subsequent demonstration. Rewriting the momentum equation:

$$\frac{\partial \rho u_1}{\partial t}+\frac{\partial \rho u_1 u_2}{\partial x_2}=\frac{\partial ST}{\partial x_2}+F_1 \tag{1.59}$$

1.8.3 Energy conservation

Considering the integrals in the Boltzmann equation with the function $\xi_2\xi_2$:

$$\frac{\partial}{\partial t}\int \xi_2\xi_2 f d\vec{\xi} + \frac{\partial}{\partial x_1}\int \xi_1\xi_2\xi_2 f d\vec{\xi} + \frac{\vec{F_1}}{\rho}\int \xi_2\xi_2 \frac{\partial f}{\partial \xi_1} d\vec{\xi} = \int \xi_2\xi_2 \Omega(f) d\vec{\xi}$$

With procedure similar to the previous ones:

$$\frac{\partial \rho E}{\partial t} + \frac{1}{2}\frac{\partial M_{122}}{\partial x_1} = F_1 u_1$$

It's necessary to explicit the moment M_{122}:

$$\begin{aligned} M_{122} &= \int (u_1u_2u_2 + u_1v_2v_2 + 2v_1v_2u_2 + v_1v_2v_2) f d\vec{\xi} \\ &= \rho u_1|\vec{u}|^2 + 2\rho u_1 e + 2u_2\int v_1v_2 f d\vec{\xi} + \int \vec{v}|\vec{v}^2| f d\vec{\xi} \\ &= 2\rho u_1 E + 2u_2 \int v_1v_2 f d\vec{\xi} + \int v_1v_2^2 f d\vec{\xi} \end{aligned}$$

Dividing by two and substituting in the equation:

$$\frac{\partial \rho E}{\partial t} + \frac{\partial \rho u_1 E}{\partial x_1} = F_1u_1 - \frac{\partial}{\partial x_1}\left(u_2\int v_1v_2 f d\vec{\xi}\right) - \frac{\partial}{\partial x_1}\int v_1v_2^2 f d\vec{\xi}$$

The one obtained is the *energy conservation equation.* For the right hand side, the second term is related to the work developed by the Cauchy stresses, and the third can be seen as a diffusion of energy. The vector defined by the integral:

$$\int v_1v_2^2 f d\vec{\xi} \tag{1.60}$$

represents the diffusion of energy and is indicated below with symbol $\vec{Q}$. Considering the momentum equation multiplied by u_1, (obtaining the equation of conservation of mechanical energy), through a few substitution steps we obtain:

$$\frac{\partial \rho e}{\partial t} + \frac{\partial \rho u_1 e}{\partial x_1} = -\frac{\partial u_2}{\partial x_1}\int v_1v_2 f d\vec{\xi} - \frac{1}{2}\frac{\partial}{\partial x_1}\int v_1v_2^2 f d\vec{\xi} \tag{1.61}$$

This is the *internal energy conservation equation.*

1.8.4 Conservation equation and equilibrium - The Euler equation

The stress tensor ST and the diffusion of energy $\vec{Q}$ depend on the distribution function. It is possible to find a relationship with the other macroscopic variables only after having defined the distribution function in some way. A first assumption about the form of distribution function is that it is locally not so far from the function at equilibrium f^{eq}. With this idea is not so diffcult to find the expressions of ST and $\vec{Q}$

$$ST^{eq} = -\int v_1v_2 f d\vec{\xi} = -\frac{\rho}{2b}\delta_{12} = -p\delta_{12} \tag{1.62}$$

$$\vec{Q} = \frac{1}{2}\int v_1v_2v_2 f d\vec{\xi} = 0 \tag{1.63}$$

With this assumption, the momentum and internal energy conservation equations can be rewritten:

$$\frac{\partial \rho u_1}{\partial t} + \frac{\partial \rho u_1 u_2}{\partial x_2} = F_1 - \frac{\partial p}{\partial x_1} \tag{1.64}$$

$$\frac{\partial \rho e}{\partial t}+\frac{\partial \rho u_1 e}{\partial x_1}=-p\frac{\partial u_1}{\partial x_1} \tag{1.65}$$

This two equations in addiction to the continuity equation are known as *Euler equation* in the continuum approach of fluid dynamic. In order to obtain the Navier Stokes equations of the continuous model it is necessary not to neglect the terms relating to viscosity and heat diffusion and conduction, therefore the approximation $f \simeq f^{eq}$ can not be used. To describe these phenomena, it is therefore necessary to consider the evolution of the distribution function towards equilibrium.

1.9 Bhatnagar, Gross and Krook collision operator - BGK model

In 1954 the scientists P.L. Bhatnagar, E.P. Gross, and M. Krook introduced a simplified collision operator in the Boltzmann equation (called the BGK-model) [7] which satisfies the properties seen in section 1.7.1. The BGK collision term is defined by:

$$\Omega(f)=-\frac{f-f^{eq}}{\tau} \tag{1.66}$$

τ is called *relaxation time* This model greatly simplifies the integral of collision, and it preserves the collisional invariants, as it is easy to verify considering that they are valid for f and for f^{eq}, and therefore must be the same for the difference $(f-f^{eq})$.
To verify that the BGK model implies a tendency of f to relax at equilibrium, we consider the case of homogeneous gas without external forces but not in equilibrium. From homogeneity:

$$\vec{\xi}\cdot\nabla f=0$$

The equation is:

$$\frac{\partial f}{\partial t}=-\frac{f-f^{eq}}{\tau}$$

For which the solution is:

$$f(\xi,t)=f^{eq}(\xi)+\left(f(\xi,0)-f^{eq}(\xi)\right)e^{-t/\tau}$$

The solution $f(\xi,t)$ tends exponentially to coincide with f^{eq} with a time constant of τ.

1.10 The Chapman-Enskog expansion

It is possible to obtain the macroscopic Navier Stokes equations, through a procedure of expansion of the distribution function known as "Chapman Enskog expansion". Through the procedure, we obtain an approximation of the distribution function which, stopping already at the first term, allows, through the moments of f and conservation equations, to evaluate the terms neglected for the Euler equation.
The parameter for performing the expansion is the Knudsen number, while it is useful to write the Boltzmann equation with reference to dimensionless variables. Using the following definitions of some notable quantities:

- *characterist lenght* x_0;

- *characteristic velocity* ξ_0;

- *characteristic time* $t_0 (t_0 = x_0/\xi_0)$

- *mean free path* $x_{mfp} = l_{mfp}$

- *mean free time* $t_{mfp} = x_{mfp}/\xi_0$

It is thus possible to obtain the relationships between dimensional quantities and dimensionless quantity (indicated with n superscipt)

- $\vec{x} = \vec{x^n} x_0$

- $t = t^n x_0/\xi_0$

- $\vec{\xi} = \vec{\xi^n} \xi_0$

- $\tau = \tau^n x_{mfp}/\xi_0$

- $\vec{F} = \vec{F^n} \rho \xi_0^2/x_0$

- $f = f^n \rho/c_0^3$

Writing the Boltzmann Equation with the dimensionless variables, it become:

$$\frac{x_{mfp}}{x_0}\left(\frac{\partial f^n}{\partial t} + \xi_1^n \frac{\partial f^n}{\partial x_1^n} + \vec{F_1^n}\frac{\partial f^n}{\partial \xi_1^n}\right) = \frac{1}{\tau}\left(f^n - f^{n-eq}\right) \tag{1.67}$$

Remembering tath the Knudsen Number Kn is equal to x_{mfp}/x_0, the right hand side decreases with Kn, so for small Kn also the left hand side is small and it is possible to say that f can be approximated as f^{eq}. In this case also the Euler Equation is a valid approximation of the fluid dynamic. Increasing Kn the distribution function could be sensibly different from f^{eq} and a macroscopic model is needed in order to describe the phenomena related to non equilibrium such diffusion terms in the momentum and energy equation. It seems correct to express the distribution function as a power series expansion centered on the equilibrium function and considering the terms function of Kn. A parameter ϵ is introduced to express the dependence from Kn of the generic term of the series:

$$f = f^{eq} + \epsilon f^{(1)} + \epsilon^2 f^{(2)} + \dots \tag{1.68}$$

Truncating at the first term of the series the error is order ϵ, that is order Kn, truncating at second term the error is $O(Kn^2)$ and so on.
Substituting f in the Boltzmann equation with its expansion

$$\left(\frac{\partial}{\partial t} + \xi_1 \frac{\partial}{\partial x_1} + \vec{F_1}\frac{\partial}{\partial \xi_1}\right)(f^{eq} + \epsilon f^{(1)} + \epsilon^2 f^{(2)} + \dots) = -\frac{1}{\epsilon\tau}(\epsilon f^{(1)} + \epsilon^2 f^{(2)} + \dots) \tag{1.69}$$

it is possible to see this expression as a set of independent equations, one for each different order of Kn, so as to write one equation at $O(Kn^0)$, another at $O(Kn^1)$ and so on. This means to have an equation at the $O(Kn^0)$ level where on the left appears f^{eq} and on the right $f^{(1)}$, and it is possible to write $f^{(1)}$ function of f^{eq} . At the next level $O(Kn^1)$ one can write $f^{(2)}$ function of $f^{(1)}$, then $f^{(3)}$ function of $f^{(2)}$ and so on. This however means not to consider that the temporal derivative should be developed in different terms for each order of Kn, so it is not possible to state that the equation are rigorously independent.

As prevously seen, the moments of density, momentum,and energy of f^{eq} and f are the same, so another assumption is that the moments of each $f^{(i)}$ term of the series are zero and not only their sum.

$$\begin{gathered}\int f^{(i)} d\vec{xi} = 0 \\ \int \vec{xi} f^{(i)} d\vec{xi} = 0 \\ \int |\xi^2| f^{(i)} d\vec{xi} = 0 \\ \int |v^2| f^{(i)} d\vec{xi} = 0\end{gathered} \tag{1.70}$$

Just writing f in the expanded form, it seems plausible to expand in terms of Kn also the stress tensor ST and the thermal flow vector $\vec{Q}$:

$$ST = ST^{(0)} + \epsilon ST^{(1)} + \epsilon^2 ST^{(2)} + \dots \tag{1.71}$$

$$\vec{Q} = \vec{Q}^{(0)} + \epsilon \vec{Q}^{(1)} + \epsilon^2 \vec{Q}^{(2)} + \dots \tag{1.72}$$

The link with the macroscopic equations, and in particular with the Navier-Stokes equations, is obtained through the definition of $ST^{(1)}$ and $Q^{(1)}$.

1.10.1 Definition of first term $f^{(1)}$

With the aim of defining $ST^{(1)}$ and $Q^{(1)}$, the definition of the first term of f expansion as a function of macroscopic variables is necessary.

Let's begin by considering the Boltzmann equation, with BGK approximation, and replacing the expansion until the first order:

$$\frac{\partial f^{eq}}{\partial t} + \vec{\xi} \cdot \nabla f^{eq} + \frac{\vec{F}}{\rho} \cdot \nabla_{\xi} f^{eq} = -\frac{f^{(1)}}{\tau} \tag{1.73}$$

Dividing both sides by f^{eq} and then rewriting the derivative terms it reads:

$$\frac{\partial f^{eq}}{f^{eq} \partial t} + \vec{\xi}_1 \frac{\partial f^{eq}}{f^{eq} \partial \vec{x}_1} + \frac{\vec{F}}{\rho} \frac{f^{eq}}{f^{eq} \partial \vec{\xi}_1} = -\frac{f^{(1)}}{f^{eq}} \frac{1}{\tau}$$

$$-\tau \left[\frac{\partial \ln f^{eq}}{\partial t} + \vec{\xi}_1 \frac{\partial \ln f^{eq}}{\partial \vec{x}_1} + \frac{\vec{F}}{\rho} \frac{\ln f^{eq}}{\partial \vec{\xi}_1} \right] = \frac{f^{(1)}}{f^{eq}} \tag{1.74}$$

From the expression of the distribution function at equilibrium (Maxwell-Boltzmann Distribution) $\ln f^{eq}$ is:

$$\ln f^{eq} = \frac{3}{2} \ln\left(\frac{3}{4\pi}\right) + \ln \rho - \frac{3}{2} \ln e - \frac{3}{4e} |\vec{\xi} - \vec{u}|^2 \tag{1.75}$$

While $(\partial \ln f^{eq} / \partial \vec{x}_1)$ (third term in square brackets) is:

$$\frac{\partial \ln f^{eq}}{\partial x_1} = -\frac{3}{4e} \frac{\partial}{\partial \xi_1} (\xi_2 \xi_2 - 2\xi_2 u_2 + u_2 u_2) = -\frac{3v_1}{2e} \tag{1.76}$$

Whereas the function at equilibrium can be expressed through the ρ,$\vec{v}$ and e variables:

$$f^{eq} = f^{eq}(\rho(\vec{x},t), \vec{u}(\vec{x},t), e(\vec{x},t), \vec{\xi})$$

So it is possible to express the derivatives through the chain rule:

$$\begin{aligned}
\frac{\partial \ln f^{eq}}{\partial t} &= \frac{\partial \ln f^{eq}}{\partial \rho}\frac{\partial \rho}{\partial t} + \frac{\partial \ln f^{eq}}{\partial \vec{u}_2}\frac{\partial \vec{u}_2}{\partial t} + \frac{\partial \ln f^{eq}}{\partial e}\frac{\partial e}{\partial t} \\
\frac{\partial \ln f^{eq}}{\partial x_1} &= \frac{\partial \ln f^{eq}}{\partial \rho}\frac{\partial \rho}{\partial x_1} + \frac{\partial \ln f^{eq}}{\partial \vec{u}_2}\frac{\partial \vec{u}_2}{\partial x_1} + \frac{\partial \ln f^{eq}}{\partial e}\frac{\partial e}{\partial x_1}
\end{aligned} \tag{1.77}$$

The single derivative can be evaluated:

$$\begin{aligned}
\frac{\partial \ln f^{eq}}{\partial \rho} &= \frac{\partial}{\partial \rho}\ln \rho = \frac{1}{\rho} \\
\frac{\partial \ln f^{eq}}{\partial u_2} &= \frac{3v_2}{2e} \\
\frac{\partial \ln f^{eq}}{\partial e} &= -\frac{\partial}{\partial e}\left(\frac{3|v|^2}{4e} + \frac{3}{2}\ln e\right) = \frac{1}{e}\left(\frac{3|v|^2}{4} + \frac{3}{2}\right)
\end{aligned} \tag{1.78}$$

Now it is possible to substitute equations (1.77) and (1.78) in the equation for $f^{(1)}/f^{eq}$:

$$\begin{aligned}
\frac{f^{(1)}}{f^{eq}} &= -\tau\Bigg[\frac{1}{\rho}\left(\frac{\partial \rho}{\partial t} + (u_1+v_1)\frac{\partial \rho}{\partial x_1}\right) + \frac{3v_2}{2e}\left(\frac{\partial u_2}{\partial t} + (u_1+v_1)\frac{\partial u_2}{\partial x_1}\right) + \\
&\frac{1}{e}\left(\frac{3v^2}{2e} - \frac{3}{2}\right)\left(\frac{\partial e}{\partial t} + (u_1+v_1)\frac{\partial e}{\partial x_1}\right) - \frac{3}{2\rho e}F_1 v_1\Bigg]
\end{aligned} \tag{1.79}$$

The right-hand side is a development of f^{eq}, so Euler's equations are valid for expressing individual terms. Rewriting the conservation of mass equation:

$$\begin{aligned}
\frac{\partial \rho}{\partial t} + \frac{\partial \rho u_1}{\partial x_1} = 0 \implies \\
\left(\frac{\partial}{\partial t} + u_1\frac{\partial}{\partial x_1}\right)\rho = -\rho\frac{\partial u_1}{\partial x_1}
\end{aligned}$$

Momentum Equation:

$$\begin{aligned}
\frac{\partial \rho u_1}{\partial t} + \frac{\partial \rho u_1 u_2}{\partial x_2} = F_1 - \frac{\partial p}{\partial x_1} \implies \\
\left(\frac{\partial}{\partial t} + u_1\frac{\partial}{\partial x_1}\right)u_2 = \frac{1}{\rho}\left(-\frac{\partial p}{\partial x_2} + F_2\right) = \frac{1}{\rho}\left(-\frac{2\rho}{3}\frac{\partial e}{\partial x_2} - \frac{\partial \rho}{\partial x_2} + F_2\right)
\end{aligned}$$

Energy Equation:

$$\begin{aligned}
\frac{\partial \rho e}{\partial t} + \frac{\partial \rho u_1 e}{\partial x_1} = -p\frac{\partial u_1}{\partial x_1} \implies \\
\left(\frac{\partial}{\partial t} + u_1\frac{\partial}{\partial x_1}\right)e = -\frac{p}{\rho}\frac{\partial u_1}{\partial x_1} = -\frac{2e}{3}\partial u_1 \partial x_1
\end{aligned}$$

By appropriately replacing these relations in the equation for $f^{(1)}/f^{eq}$:

$$\frac{f^{(1)}}{f^{eq}} = -\tau\left[\left(\frac{3v^2}{4e} - \frac{5}{2}\right)\frac{v_1}{e}\frac{\partial e}{\partial x_1} + \frac{3}{2e}\left(v_1 v_2\frac{\partial u_2}{\partial x_1} - \frac{v_2^2}{3}\frac{\partial u_1}{\partial x_1}\right)\right] \tag{1.80}$$

Using the Kronecker δ the last term can be rewritten:

$$\left(v_1 v_2\frac{\partial u_2}{\partial x_1} - \frac{v_2^2}{3}\frac{\partial u_1}{\partial x_1}\right) = v_1 v_2\left[\frac{1}{2}\left(\frac{\partial u_2}{\partial x_1} + \frac{\partial u_1}{\partial x_2}\right) - \frac{1}{3}\delta_{12}\frac{\partial u_3}{\partial x_3}\right] \tag{1.81}$$

We can exstrat a tensor $SymST$ defined by:

$$SymST = \frac{1}{2}\left(\frac{\partial u_2}{\partial x_1} + \frac{\partial u_1}{\partial x_2}\right) - \frac{1}{3}\delta_{12}\frac{\partial u_3}{\partial x_3}$$

It is symmetric, in particular, is the symmetric part of *strain rate tensor.* With the procedure seen above we can define $f^{(1)}$:

$$f^{(1)} = -\tau f^{eq}\left[\left(\frac{3v^2}{4e} - \frac{5}{2}\right)\frac{v_1}{e}\frac{\partial e}{\partial x_1} + \frac{3}{2e}v_1 v_2 SymST\right] \tag{1.82}$$

1.10.2 Definition od $ST^{(1)}$ and $Q^{(1)}$

It is possible to evaluate $ST^{(1)}$ and $Q(1)$ through the moments of $f^{(1)}$:

$$\begin{aligned} ST^{(1)} &= -\int v_1 v_2 f^{(1)} d\vec{\xi} \\ &= \tau\left[\int\left(\frac{3v^2}{4e} - \frac{5}{2}\right)\frac{1}{e}\frac{\partial e}{\partial x_1}v_1 v_2 v_3 f^{eq} d\vec{\xi} + + \int \frac{3}{2e} SymST v_1 v_2 v_3 v_4 f^{eq} d\vec{\xi}\right] \end{aligned}$$

First integral is 0 because is a third order momentum, the second is:

$$\int v_1 v_2 v_3 v_4 f^{eq} d\vec{\xi} = \frac{4}{9}\rho e^2(\delta_{12}\delta_{34} + \delta_{13}\delta_{24} + \delta_{14}\delta_{23})$$

Substituing in the expression for $ST^{(1)}$:

$$\begin{aligned} ST^{(1)} &= \tau\frac{3}{2e}\frac{2}{9}\rho e^2 SymST(\delta_{12}\delta_{34} + \delta_{13}\delta_{24} + \delta_{14}\delta_{23}) \\ &= \frac{4}{3}\rho e\tau SymST(\delta_{12}\delta_{34} + SymST\delta_{13}\delta_{24} + SymST\delta_{14}\delta_{23}) \end{aligned}$$

The first term in parenthesys is 0 because of simmetry of SymST, instead the other two terms are equal to SymST. So the final expression is:

$$ST^{(1)} = \frac{4}{3}\rho e\tau SymST \tag{1.83}$$

From definition of $\vec{Q}$:

$$\begin{aligned} \vec{Q}^{(1)} &= \frac{1}{2}\int v_1 v^2 f^{(1)} d\vec{\xi} = \\ -\frac{\tau}{2}&\left[\int\left(\frac{3v^2}{4e} - \frac{5}{2}\right)\frac{1}{e}\frac{\partial e}{\partial x_1}v^2 v_1 v_2 f^{eq} d\vec{\xi} + \int \frac{3}{2e} SymST v^2 v_1 v_2 v_3 f^{eq} d\vec{\xi}\right] \end{aligned}$$

The second integral is 0, we have:

$$\begin{aligned} \vec{Q}^{(1)} &= -\frac{\tau}{2}\frac{\partial e}{\partial x_1}\left[\frac{3}{4e}\int v^4 v_1 v_2 f^{eq} d\vec{\xi} - \frac{5}{2}\int v^2 v_1 v_2 f^{eq} d\vec{\xi}\right] \\ &= -\frac{\tau}{2}\frac{\partial e}{\partial x_1}\left[\frac{1}{4e}\delta_{12}\int v^6 f^{eq} d\vec{\xi} - \frac{5}{6}\delta_{12}\int v^2 v_1 v_2 f^{eq} d\vec{\xi}\right] \end{aligned}$$

Calculating the integrals the final expression is:

$$\vec{Q}^{(1)} = -\frac{10}{9}\rho e\tau\frac{\partial e}{\partial x_1} \tag{1.84}$$

1.10.3 The Navier-Stokes Equation

Expressing the stress tensor with:

$$ST = ST^{eq} + ST^{(1)} \tag{1.85}$$

and the energy diffusion term with:

$$\vec{Q}^{(1)} = Q^{(eq)} + Q^{(1)} \tag{1.86}$$

It is possible to redefine the respective terms in the conservation equation of momentum and energy. The Navier-Stokes equation are obtained:

- Mass Conservation

$$\frac{\partial \rho}{\partial t} + \frac{\partial \rho u_1}{\partial x_1} = 0 \tag{1.87}$$

- Momentum Conservation

$$\frac{\partial \rho u_1}{\partial t} + \frac{\partial \rho u_1 u_2}{\partial x_2} = F_1 - \frac{\partial}{\partial x_2}\left(-\delta_{12} p + ST^{(1)}\right) \tag{1.88}$$

- Energy Conservation

$$\frac{\partial \rho e}{\partial t} + \frac{\partial \rho u_1 e}{\partial x_1} = \left(-\delta_{12} p + ST^{(1)}\right)\frac{\partial u_2}{\partial x_1} + \frac{\partial}{\partial x_1}\kappa\frac{\partial T}{\partial x_1} \tag{1.89}$$

where κ is the thermal conductivity, which has the expression:

$$\kappa = \frac{5}{3}\rho e R\tau = \frac{5}{2} p R\tau = \frac{5}{2}\rho R^2 T\tau \tag{1.90}$$

It is notable that the viscosity μ and thermal conductivity κ, macroscopic properties of the fluid, are defined here in function of relaxation time τ thanks to the kinetic theory and to the choice of BGK approxymation.

Chapter 2

Lattice Boltzmann Method

2.1 Basic Idea

Analytical solutions of Boltzmann Equation in practical cases are very difficult to find, so it's necessary to solve it numerically through an opportune discretization of distribution function. Function f depends on position $\vec{x} \in \mathbb{R}^3$, velocity $\vec{\xi} \in \mathbb{R}^3$ and time $t \in \mathbb{R}^+$, considering marching forward in time, each time steps it is necessary to consider a strategy of discretization for the vector space of configurations $\mathbb{R}^3 \times \mathbb{R}^3$. It plans to discretize the velocity domain first, with the choice of an appropriate set of velocities, and then the discretization of the space. In this way every point of the physical space is characterized by the number of possible velocities considered.
For the cases in question, characterized by a low Reynolds number and low Mach numbers, the gas can be considered isothermal. Furthermore, in the Boltzmann equation the external forces on the molecules will be neglected.
Indicated with T_0 the fluid temperature, it is possible to find a constant speed of sound c_0 and a consequent equation of state:

$$c_0^2 = \left(\frac{\partial p}{\partial \rho}\right) = \frac{k_B T_0}{m} \tag{2.1}$$

$$p = c_0^2 \rho \tag{2.2}$$

2.2 Equilibrium distribution function and discrete-velocity BGK Boltzmann Equation

Also the equilibrium distributiom function f^{eq} must be expressed as a function of the chosen set of velocities, to obtain this we consider an approximation of the function at equilibrium, or its expansion in u (mean fluid velocity) accurate to the second order ($O(u^2)$):

$$\begin{aligned} f^{eq} &= \rho \left(\frac{\rho}{2\pi p}\right)^{\frac{3}{2}} e^{-\rho|v|^2/2c_0^2} \\ &= {\frac{\rho}{2\pi c_0^2}}^{\frac{3}{2}} e^{-\rho|(\vec{\xi}-\vec{u})|^2/2c_0^2} \\ &= {\frac{\rho}{2\pi c_0^2}}^{\frac{3}{2}} e^{-\rho|(\vec{\xi}^2-2\vec{\xi}\vec{u}+\vec{u}^2)|/2c_0^2} \end{aligned}$$

Expanding with respect to the variable $\vec{u}$ until third term, it reads:

$$f^{eq} = \frac{\rho}{(2\pi c_0^2)^{\frac{3}{2}}} e^{-\vec{\xi}^2/2c_0^2} \left(1 + \frac{\xi_1 u_1}{c_0^2} + \frac{(\xi_1 u_1)^2}{2c_0^4} - \frac{u_1 u_1}{c_0^2}\right)$$

Discretizing with a set of velocity $\vec{\xi_i}$ for $i = 1, \dots, n$, in each point $(\vec{x}, t)$ $f(\vec{x}, \vec{\xi}, t)$ is discretized in n components $f(\vec{x}, t)_i$, and also $f^{eq}(\vec{x}, \vec{\xi}, t)$ begin $f^{eq}(\vec{x}, t)_i$. We can write f_i^{eq} as:

$$f_i^{eq} = \rho w_i \left(1 + \frac{\xi_{i1} u_1}{c_0^2} + \frac{(\xi_{i1} u_1)^2}{2c_0^4} - \frac{u_1 u_1}{c_0^2}\right) \tag{2.3}$$

where $w_i = e^{-(\vec{\xi_i}\vec{\xi_i})/2c_0^2}/(2\pi c_0^2)^{\frac{3}{2}}$.

Now the *discrete-velocity Boltzmann Equation* can be written:

$$\frac{\partial f_i}{\partial t} + \xi_i \frac{\partial f_i}{\partial \xi_i} = -\frac{1}{\tau}(f_i - f_i^{eq}) \tag{2.4}$$

In this phase the above equation is still continuous in physical space and in time.

2.2.1 Constrains for velocity set

The choice of the discretization of the velocity domain [18] must be such as to respect the equivalence of the moments for the distribution function in the continuous, the moments in the discrete case being summations. Equivalence involves constraints in the choice of velocities. Considering the moments at equilibrium, the following relations have to be valid:

$$\begin{aligned}
&\sum_i f_i^{eq}(\vec{x}, t) = \rho(\vec{x}, t) \\
&\sum_i \xi_{i1} f_i^{eq}(\vec{x}, t)\rho\vec{u}(\vec{x}, t) = \rho\vec{u}(\vec{x}, t) \\
&\sum_i \xi_{i1}\xi_{i2} f_i^{eq}(\vec{x}, t) \int \xi_1\xi_2 f^{eq} d\vec{xi} = M_{12}^{eq}(\vec{x}, t) \\
&\sum_i \xi_{i1}\xi_{i2}\xi_{i3} f_i^{eq}(\vec{x}, t) \int \xi_1\xi_2\xi_2 f^{eq} d\vec{xi} = M_{123}^{eq}(\vec{x}, t)
\end{aligned} \tag{2.5}$$

From the first equation:

$$\rho = \sum_i f_i^{eq} = \rho \left[\sum_i w_i + \frac{u_i}{c_0^2}\sum_i w_i \xi_{i1} + \frac{u_1 u_2}{2c_0^2}\left(\frac{1}{c_0^2}\sum_i w_i \xi_{i1}\xi_{i2} - \delta_{12}\sum_i w_i\right)\right] \implies$$

$$\implies \sum_i w_i + \frac{u_i}{c_0^2}\sum_i w_i \xi_{i1} + \frac{u_1 u_2}{2c_0^2}\left(\frac{1}{c_0^2}\sum_i w_i \xi_{i1}\xi_{i2} - \delta_{12}\sum_i w_i\right) = 1$$

This result is possible if:

$$\sum_i w_i = 1 \tag{2.6}$$

$$\sum_i \xi_{i1} w_i = 0 \tag{2.7}$$

$$\sum_i \xi_{i1}\xi_{i2} w_i = c_0^2 \delta_{12} \tag{2.8}$$

From the second equation it must be:

$$\frac{u_2}{c_0^2}\sum_i w_i \xi_{i1}\xi_{i2} + \left(1 - \frac{u_1 u_2}{2c_0^2}\right)\sum_i w_i \xi_{i1} + \frac{u_3 u_4}{2c_0^4}\sum_i w_i \xi_{i1}\xi_{i2}\xi_{i3} = u_1$$

Subsituing in equation (2.6) in the above equations:

$$\frac{u_2}{c_0^2}\sum_i w_i\xi_{i1}\xi_{i2} = u_2\delta_{12} = u_1$$
$$\sum_i w_i\xi_{i1} = 0$$

The equation for first order moment reads:

$$\sum_i \xi_{i1}\xi_{i2}\xi_{i3}w_i = 0 \tag{2.9}$$
$$\sum_i \xi_{i1}\xi_{i2}\xi_{i3}\xi_{i4}w_i = c_0^4(\delta_{12}\delta_{34} + \delta_{13}\delta_{24} + \delta_{14}\delta_{23}) \tag{2.10}$$

Let us consider the third equation for second order moment,

$$\begin{aligned} M_{12}^{eq} &= \rho u_1u_2 + \rho c_0^2\delta 12 = \sum_i \xi_{i1}\xi_{i2}f_i^{eq} \\ &= \rho\left[\left(1 - \frac{u_3u_3}{2c_0^2}\right)\sum_i w_i\xi_{i1}\xi_{i2} + \frac{u_3}{c_0^2}\sum_i \xi_{i1}\xi_{i2}\xi_{i3}w_i + \frac{u_3u_4}{2c_0^4}\sum_i \xi_{i1}\xi_{i2}\xi_{i3}\xi_{i4}w_i\right] \end{aligned}$$

Using equations (2.6) and (2.9), it follows:

$$\frac{u_3u_4}{2c_0^4}\sum_i \xi_{i1}\xi_{i2}\xi_{i3}\xi_{i4}w_i - \frac{u_3u_3}{2}\delta_{12} = \rho u_1u_2$$

That implies the constrain:

$$\sum_i \xi_{i1}\xi_{i2}\xi_{i3}\xi_{i4}w_i = c_0^4(\delta_{12}\delta_{34} + \delta_{13}\delta_{24} + \delta_{14}\delta_{23}) \tag{2.11}$$

Considering the fourth equation for third order moment. First of all we write the M_{123}^{eq}:

$$M_{123}^{eq} = \rho u_1u_2u_3 + \rho c_0^2(u_1\delta_{23} + u_2\delta_{13} + u_3\delta_{12})$$

Given the approximation used for f^{eq}, it is impossible to rigourously respect this moment, also the moment has to be approxymated with a discrete form of the moment M_a123^{eq}

$$M_{123}^{eq} = \rho c_0^2(u_1\delta_{23} + u_2\delta_{13} + u_3\delta_{12})$$

It involves the last constrain:

$$\sum_i \xi_{i1}\xi_{i2}\xi_{i3}\xi_{i4}w_i\xi_{i5}\xi_{i6} = 0 \tag{2.12}$$

The approxymation of the moment of third order M_{123}^{eq}, gives an error term of order $O(u^3)$, however from the comparison of the exact expression of M_{123}^{eq} , it turns out to be negligible if $u^2 << c_0^2$, i.e. for low Mach numbers, it is the case of interest for the pourpose of this work. Moreover, using the Chapman Enskog expansion, it is possible to show that the discrete velocities Boltzmann Equation with the above constrains, namely, equations (2.6),(2.9),(2.11),(2.12), can approxymate Navier-Stokes equation with second order accuracy.

2.2.2 Discretization of Physical Space - D2Q9 and D3Q19 lattice

The physical space is discretized with a regular Cartesian grid, called, as usual, *lattice.* In each *Eulerian point* of the mesh, we have to compute a discretized distribution function, this means compute all components corresponding to a chosen set of velocities. To indicate a set of velocity vectors, a typical abbreviation in DnQm, where n indicates the geometric dimension of the problem (from 1 to 3 for hydrodynamics purpose) whyle m is the number of velocities used. In this work we choose the typical D2Q9 set for 2D cases and the D3Q19 set for the tridimensional cases. For D2Q9, represented in fig.2.1, the possible magnitudes of the velocity vectors are:

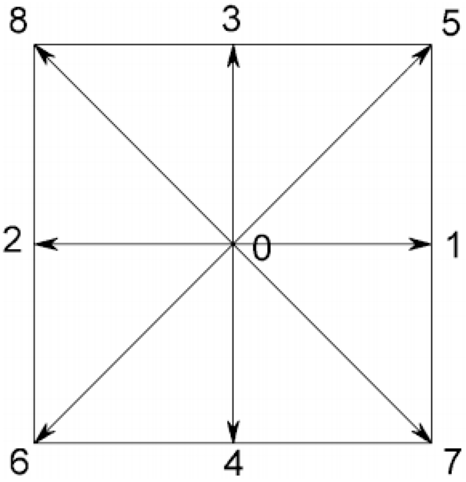

Figure 2.1: D2Q9 lattice

$$\xi_0 = 0, \quad \xi_{1-4} = \frac{\Delta x}{\Delta t}, \quad \xi_{5-8} = \sqrt{2}\frac{\Delta x}{\Delta t}$$

At this point it is necessary to calculate the weights w_i, noting that the equalities of the modules of the vectors involve the relationships:

$$w_1 = w_2 = w_3 = w_4$$
$$w_5 = w_6 = w_7 = w_8$$

From the constrains seen in the previous subsection:

$$\begin{aligned}
&w_0 + w_1 + w_5 = 1 \\
&\left(\frac{\Delta x}{\Delta t}\right)^2 (2w_1 + 4w_5) = c_0^2 \\
&\left(\frac{\Delta x}{\Delta t}\right)^4 4w_5 = c_0^4 \\
&\left(\frac{\Delta x}{\Delta t}\right)^4 (2w_1 + 4w_5) = 3c_0^4
\end{aligned}$$

This linear system of four equations is solved by:

$$\begin{aligned}
w_0 &= \frac{4}{9} \\
w_{1-4} &= \frac{1}{9} \\
w_{1-4} &= \frac{1}{36} \\
c_0 &= \frac{1}{\sqrt{3}}\left(\frac{\Delta x}{\Delta t}\right)
\end{aligned}$$

For the D3Q19 lattice, see fig. 2.2, the velocity magnitudes are:

$$\xi_0 = 0, \quad \xi_{1-6} = \frac{\Delta x}{\Delta t}, \quad \xi_{7-18} = \sqrt{2}\frac{\Delta x}{\Delta t}$$

with the same constrains (note that the third non zero constrain involves another equation) the weight w_i and c_0 are calculated:

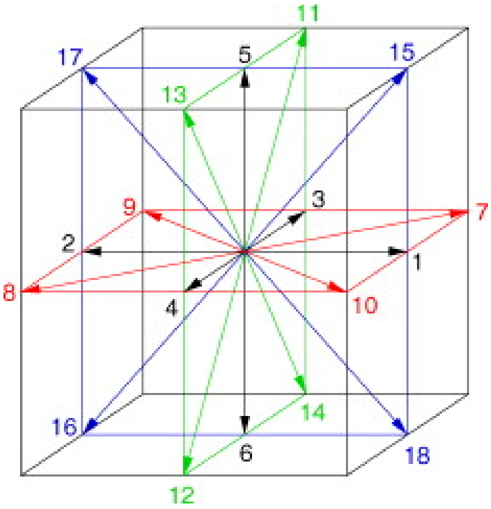

Figure 2.2: D3Q19 lattice

$$w_0 = \frac{4}{9}$$
$$w_{1-4} = \frac{1}{9}$$
$$w_{5-8} = \frac{1}{36}$$
$$c_0 = \frac{1}{\sqrt{3}}\left(\frac{\Delta x}{\Delta t}\right)$$

At this point it is possible to find the discretization in space and time to obtain the full discretized Boltzmann equation, called *Lattice Boltzmann equation*.
Let consider the Boltzmann Equation with BGK term:

$$\frac{\partial f}{\partial t} + \xi_1 \frac{\partial f}{\partial x_1} = -\frac{1}{\tau}(f - f^{eq})$$

It is an hyperbolic partial differenzial equation as well as the discrete velocity BGK Boltzmann Equation 2.4, so it is possible to study them using method of characteristics and defining a curvilinear coordinate s along the characteristic. The total derivative of f respect to s is:

$$\frac{\partial f}{\partial t}\frac{dt}{ds} + \frac{\partial f}{\partial x_1}\frac{dx_1}{ds} = -\frac{1}{\tau}(f - f^{eq})$$

This implies that:

$$\frac{dt}{ds} = 1 \quad \text{and} \quad \frac{dx_1}{ds} = \xi_1$$

Comparing with velocity discretized equation it must be:

$$\frac{dx_1}{ds} = \xi_i$$

The above relations allow to state that in each geometric lattice point, along the characteristic curves the function $f(\vec{x},t)$ can be written as $f(\vec{x}+\xi_i s, t+a)$, with $s \geq 0$. It is possible to integrate in a single time step, from 0 to $s = \Delta t$, both sides of equation; the left hand side is immediate

$$\int_0^{s=\Delta t} \left(\frac{df}{ds}\right) ds = f(\vec{x}+\xi_i \Delta t, t+\Delta t) - f(\vec{x},t)$$

The integral on right hand side is approximated usinf a simple first order formulation:

$$-\frac{1}{\tau}\int_0^{s=\Delta t} [f(\vec{x}+\xi_i s, t+s) - f^{eq}(\vec{x}+\xi_i s, t+s)]ds = -\frac{1}{\tau}\left[f(\vec{x},t) - f^{eq}(\vec{x},t)\right]$$

The first order *Lattice Boltzmann* equation is obtained:

$$f(\vec{x}+\xi_i \Delta t, t+\Delta t) - f(\vec{x},t) = -\frac{1}{\tau}\left[f(\vec{x},t) - f^{eq}(\vec{x},t)\right] \tag{2.13}$$

Even if this is a first order discretization it can be shown that the resulting numerical scheme corresponds to a discretization of second order accuracy in space and time for continuous Navier-Stokes model. Moreover the comparison with the continuos model leads to define the viscosity μ as:

$$\mu = c_0^2\left(\tau - \frac{1}{2}\right) \tag{2.14}$$

The equation 2.13 is fully explicit, this implies the possibility of implementing a very efficient computational solver, having a small number of operations to be performed to update over time the solution of f_i.

2.3 Lattice Boltzmann Simulations for Low Reynolds number

In the simulations performed with Lattice Boltzmann method is convenient to set $\Delta x = \Delta t = 1$, this choice determines a conversion between physical quantities (indicated with ph) and quantities for the method (indicated with LBM). A correct simulation must be carried out respecting the geometric ratios and, in the case of incompressible flows, also the Reynolds number. This conditions toghether with the stability condition related to the choise of relaxation time τ allow to correctly define a reference velocity for the simulation, u_{LBM}, and the viscosity μ_{LBM}. The passage from physical quantities to LBM ones and vice versa can be obtained easily. To analyze the stability method we can consider the simple case of a distribution function homogenous in space ($\nabla f(\vec{\xi},t) = 0$), it must be:

$$f_i(\vec{x}+\xi_i, t) = f_i(\vec{x},t) = f_i(x,y,z,t) \tag{2.15}$$

The Lattice Boltzmann equation becomes:

$$f_i(x,y,z,t+1) = \left(1 - \frac{1}{\tau}\right) f_i(x,y,z,t) + \frac{1}{\tau} f_i^{eq} \tag{2.16}$$

- With $\tau = 1$, in one time steps the solution $f_i(x,y,z) = f_i^{eq}$ is obtained, this is the optimal choice for τ.
- If $\tau > 1$ the solution tends to f_i^{eq} gradually more slowly.
- If $0.5 < \tau < 1$, $f_i(x,y,z)$ oscillates around $= f_i^{eq}$ with decaying amplitude.
- If $\tau > 0.5$, $f_i(x,y,z)$ oscillates around $= f_i^{eq}$ with increasing amplitude.

So we can consider $\tau = 0.5$ a stability limit. In all the simulations executed τ is setted near to a value close to 1. Knowing the value of τ it is possible to calculate the viscosity μ_{LBM} from equation (2.14). Since the spatial coordinates are given in lattice intervals, Reynolds number reference lenght L_{ref} is related to the lattice dimensions, so their choice, uniquely defines the reference velocity (called u_{max}) of a simulation. In fact to respect Reynolds number:

$$Re = \frac{L_{ref} u_{max}}{\mu} \implies u_{max} = \frac{Re \mu}{L_{ref}} \tag{2.17}$$

A well posed simulation has to respect also the limitation of Mach number: $Ma = u_{max}/c_0 << 1$, this implies an appropriate choise of L_{ref} and of the connected lattice dimensions.

2.3.1 Development of a 2d-parallel code and a 3d-parallel code

A 2d-parallel code and a 3d-parallel code are been developed, using Fortran90 language, and MPICH library. In the following section velocity vector is indicated with u symbol. The steps to perform a simulatons are as follows:

1. Reading of simulation parameters: lattice global dimension, reference lenght L_{ref}, relaxation time τ, Reynolds number, number of iteration to execute

2. Inizialization of fluid field setting an initial velocity and computation of f^{eq} in lattice points.

3. Set boundary conditions.

4. Starting main iteration loop to compute solution at time step n+1: Correction of f^{eq} to respect boundary conditions.

5. Collide step: compute velocity u from moments and the left hand side of equation (2.13).

6. Streaming step: update $f_i(n + 1)$ from Right hand side of (2.13).

7. Write solution to file output if requested.

8. Return to step 4

2.3.2 Boundary condition

Imposing the boundary conditions for the Lattice Boltzmann method means establishing some constraints regarding the values of the discretized distribution function at the boundary points of the lattice. This means to do a transfer from the conditions established through the fluid-dynamic variables, to conditions in correspondence with the lattice velocities. Therefore, relations will be obtained between the components of the distribution function for each physical boundary conditions.
In the code the following boundary conditions are defined and implemented:

- Wall boundary condition: in corrispondence of the lattice boundary points
- Fixed velocity at a wall
- Velocity inlet
- Pressure inlet and outlet
- Periodic conditions in opposite lattice boundary.

The boundary condition, or we could say the correction of f_i in internal lattice point, due to the presence of an obstacle is described in the next chapter.
The following is a brief description of the conditions implemented.

Wall lattice boundary

For the wall condition on boundary lattice we consider the so called “bounce back condition” [5]. It is used both for stationary boundary conditions and for moving walls; the basic hypothesis of the model is that the fluid particle in the node, meeting the solid wall, rebounds again in the fluid domain going to place in a known reticular position. The distribution function is propagated from an internal point to an external solid, it is refused and only during the propagation phase of the next iteration returns to the node from which it started. Consider the only two-dimensional case, referring to fig. 2.3 the scheme involves the following relations:

$$\begin{aligned} f_2 &= f_4 \\ f_5 &= f_7 \\ f_6 &= f_8 \end{aligned}$$

with f_4,f_7,f_8, are known after streaming process.

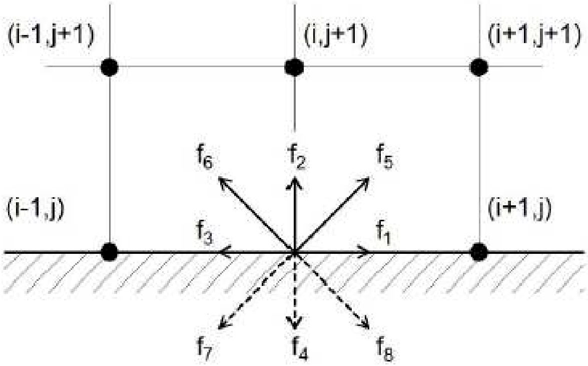

Figure 2.3: Bounce back

Fixed Velocity or pressure

The fixed speed condition is based on the Xou and He [9] method. With reference to the lattice D3Q19, at the boundary $z = 0$, the relations for the moments of f can be written:

$$\rho = f_0 + f_1 + f_2 + f_3 + f_4 + f_5 + f_6 + f_7 + f_8 + f_9 + f_{10} + f_{11} + f_{12} + f_{13} + f_{14} + f_{15} + f_{16} + f_{17} + f_{18} \quad (2.18)$$

$$\rho u_x = f_1 + f_7 + f_8 + f_9 + f_{10} - (f_2 + f_{11} + f_{12} + f_{13} + f_{14}) \quad (2.19)$$

$$\rho u_y = f_3 + f_7 + f_{11} + f_{15} + f_{16} - (f_4 + f_8 + f_{12} + f_{17} + f_{18}) \quad (2.20)$$

$$\rho u_z = f_5 + f_9 + f_{13} + f_{15} + f_{17} - (f_6 + f_{10} + f_{14} + f_{16} + f_{18}) \quad (2.21)$$

Because of the continuity equation, only three of the four variables ρ, u_x, u_y, u_z can be fixed as conditions, in this case the velocities components. So we have four equation equations and nine unknowns, the macroscopic variable ρ and the five value of f: $f_5 + f_9 + f_{13} + f_{15} + f_{17}$. Five other equations have to be defined. It is possible making the hypothesis that the deviation from the equilibrium function is null in the normal boundary direction, defining this deviation with $f_i^* = f_i - f_i^{eq}$ for the boundary in $z = 0$ it is:

$$\begin{aligned} &f_5^* = f_6^* \implies \\ &f_5 = f_6 + f_5^{eq} - f_6^{eq} = f_6 + \frac{1}{3}\rho u_z \end{aligned} \quad (2.22)$$

Other relations are related to momentum conservation in tangenzial direction to the wall. Using the deviation f_i^*, momentum conservation in x and y direction leads:

$$\begin{aligned} f_9^* &= f_{14}^* - N_x \\ f_{13}^* &= f_{10}^* + N_x \\ f_{15}^* &= f_{18}^* - N_y \\ f_{17}^* &= f_{16}^* + N_y \end{aligned} \quad (2.23)$$

where N_x, N_y are support variables that can be evaluated from the momentum conservation:

$$\begin{aligned} N_x &= \frac{1}{2}[f_1 + f_7 + f_8 - (f_2 + f_{11} + f_{12})] - \frac{1}{3}\rho u_x \\ N_y &= \frac{1}{2}[f_3 + f_7 + f_{11} - (f_4 + f_8 + f_{12})] - \frac{1}{3}\rho u_y \end{aligned} \quad (2.24)$$

The system is now closed and all variables computable.

The case of fixed pressure is very similar, in fact for the isothermal flows, is possible to write:

$$p = \rho c_s^2 \quad (2.25)$$

the density ρ is not a variable now, the unknown is normal velocity u_z, while the tangential components are null or known. The system that has to be solved for the unknown internal lattice distribution function is the same of the cae of the fixed velocity.

Periodic condition - Parallel Implementation

A periodic boundary condition for a coupled of opposite lattice bounds, is simply implemented overwriting the unknown components f_i relative to a bound with the known ones, calculated after the streming phase, in the points of the opposite one.

For our code the condition is intrinsic to the choice of lattice parallelization. In fact the LBM algorithm is totally explicit and has a local character, this allows to divide it into Cartesian blocks and entrust the computation of the collide and streming phases of the block points to a thread, i.e. a processor. Is possible to implement this logic with calls to the MPI routines defining in input settings of the simulation the number of processors N_{cpu-x},N_{cpu-y},N_{cpu-z} in the three coordinate directions.
The lattice decomposition operates through the definition of an *MPI vitual topology*, through which the Cartesian structure communicator is setted. At each new iteration the functions f_i values on the common boundaries between two blocks are communicated from each block to the adjacent one forward and backward in the three coordinate directions (3d case). It is an efficient collective comunication. For the blocks having boundary coinciding with those of the latex, a periodic communication with the opposite matching lattice boundary points is automatically set as option of the Cartesian structure, see fig. 2.4

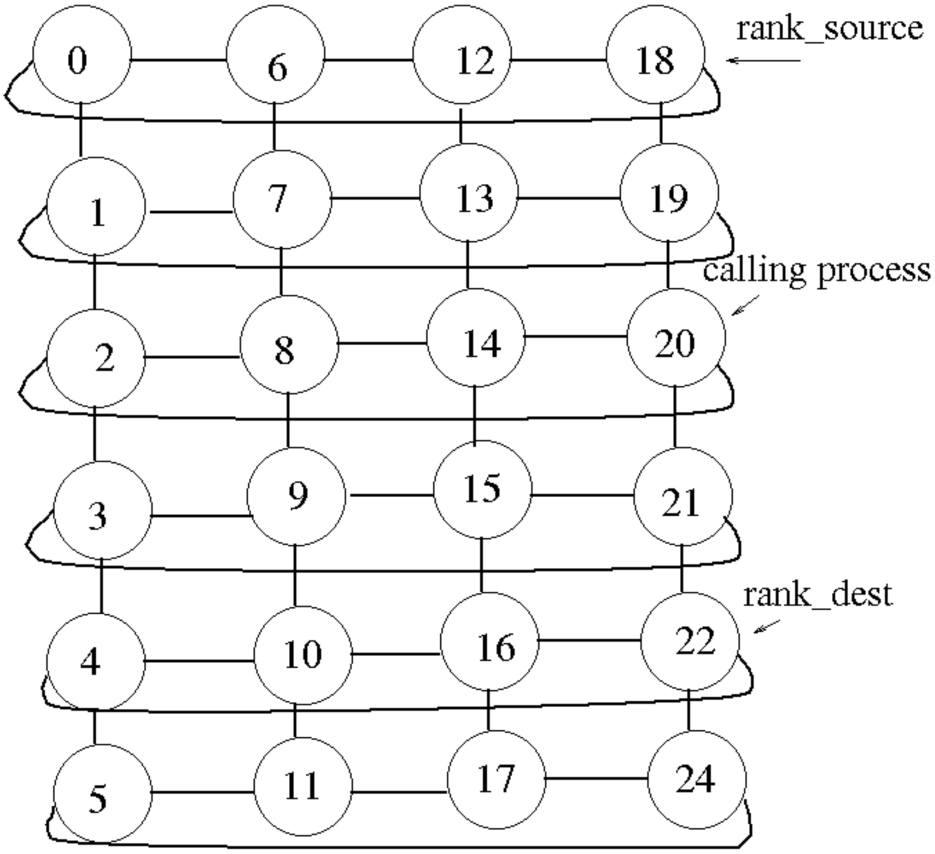

Figure 2.4: MPI cartesian comunicator and comunication

2.4 Validation and Results: Lid Driven Cavity

In this chapter we present a single 3D test with the aim of validating the Lattice Boltzmann calculation code in the part concerning fluid dynamics, considering the other validation tests carried out in the presence of obstacles in the following chapters. The test choosen is a 3D Lid Driven Cavity, a classical test for evaluation of new code accuracy in case of incompressible flow.
The test consists of a volume of fluid enclosed in a cube of side L, in which a wall is considered in motion

with a constant velocity u_{max}, the Reynolds number is referred to the length of the side of the cube, and to the velocity u_{max}. The entire lattice delimits the volume of the cube with the predicted boundary conditions of zero velocity for five of the six walls and velocity equal to u_{max} for the moving wall. u_{max} is obtained from the Reynols number and from the choice of the parameter $\omega = 1/tau = 1$, from which it is possible to derive the viscosity value in Lattice-Boltzmann units Three different tests were performed, all with Reynolds number equal to 100 but considering a discretization of the cube side in a number of intervals nx equal to 50, 100 and 200. Given that in Lattice Boltzmann units $L = nx$, this choice influences the viscosity value and the velocity value of the movable wall u_{max}. The results are compared with those producted Napolitano and Pascazio [40] The velocity components are plotted on three lines:

1. $x = y = 0.5$, $z \in [0, L]$
2. $x = z = 0.5$, $y \in [0, L]$
3. $y = z = 0.5$, $x \in [0, L]$

With the orientation of the domain as in fig.2.5a. We can observe the good agreement with the reference results and the influence of the discretization of the domain.

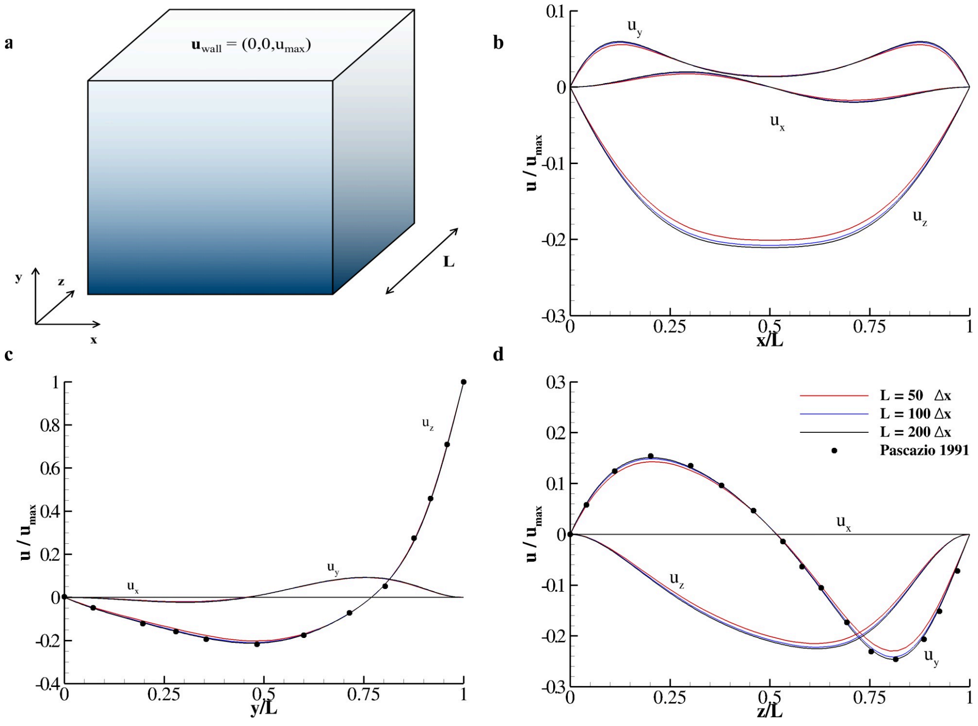

Figure 2.5: Lid driven cavity - results

Chapter 3

Immersed Boundary Method - Transport of rigid particles in low Reynolds Number flows

In the LBM under consideration, the presence of obstacles within the fluid field is considered through the immersed boundary technique [74] [10] [39]. It consists in superimposing on the lattice, or *Eulerian grid*, a second grid called *Lagrangian* grid which is the discretization of the obstacle immersed in the fluid. In the next paragraphs it is described how this grid influences the distribution function in proximity of the Lagrangian points, and therefore propagating inside the lattice thus constituting a further condition of wall. The obstacle is a solid immersed body with a structure surface discretized in N_t triangular elements. Each triangle centroid defines a *Lagrangian markers*; on this points one has to applied the no-slip condition and then from this points a force term is transfered back to *Eulerian grid points.* This force term is introduced on the right hand side in the Lattice Boltzmann equation as a *forcing term.*

$$f(\vec{x}+\xi_i\Delta t, t+\Delta t) - f(\vec{x},t) = -\frac{\Delta t}{\tau}\left[f(\vec{x},t) - f^{eq}(\vec{x},t)\right] + \Delta t\vec{F}_{ib} \tag{3.1}$$

3.1 Procedure to define the forcing term

In order to correctly impose the wall baundary condition, an adequate resolution is required for the discretization of the immersed surface, that is, the distances between the Lagrangian points must be comparable with the distances Δx between the nodes of the lattice. For the test cases in this work a good choice is a distance of about $0.7 \cdot \Delta x$.

For each Lagrangian marker the closest lattice point is identified, then is defined a *support domain*, that is a cube centered in the Lagrangian marker with a side of $r_w = 2.6\Delta x$. The support domain consists of $N_e = 9$ points of the lattice in two dimensions, and $N_e = 19$ or $N_e = 27$ in three dimensions. Once the velocities on the lattice Eulerian points of the support domain have been defined, it is possible to transfer the values on the Lagrangian point. A Moving Least Square procedure is used to build a transfer function [11], because it is able to provide a smooth solution preventing problems of accuracy, due, for example, to the curvature or intrinsic discontinuities of the structure. After the transfer, it is possible to define a forcing for Lagrangian point and then retransfer it to Eulerian points of the support domain.

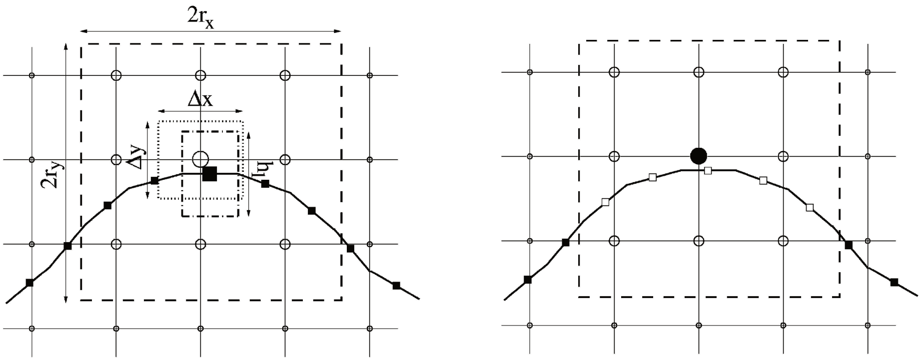

(a) (b)

Figure 3.1: (a): Support domain for a given Lagrangian marker; the squares indicate the points of the Lagrangian grid, while the circles indicate the 9 points Eulerians included in the support domain. White squares indicates Lagrangian points involved in calculating the forcing term.

The reconstruction procedure steps are based on the work of M.D. deTullio and G.Pascazio [14], and are provided in the following:

1. Compute the intermidiate velocity in the Eulerian grid points, which is computed from solution at time level n.

2. Compute the velocity of each Lagrangian marker through the MLS method:

$$\vec{U}_L(\vec{x}_L) = \sum_{k=1}^{N_e} \Phi_k^l(\vec{x}_L)\vec{\xi}_k,$$

where $\vec{\xi}_k$ indicates the velocity at the k-th Eulerian point associated with the marker and Φ is the transfer operator obtained minimizing with respect to $a(x_L)$ a weighted L2-norm as follows:

$$J = \sum_{k=1}^{N_e} W\left(\vec{x} - \vec{x}_L\right)\left[\vec{p}^T(\vec{x}_k)\vec{a}(\vec{x}) - \vec{\xi}_k\right]^2,$$

where p^T is a basis function vector and $\vec{a}(\vec{x})$ is a vector of coefficients defined by the equation:

$$\sum_{k=1}^{N_e} \Phi_k^l(\vec{x}_L)\vec{\xi}_k = \vec{p}^T(\vec{x}_k)\vec{a}(\vec{x}),$$

$W\left(\vec{x} - \vec{x}_L\right)$ is a weight function. In this thesis a linear basic function is considered for $p^T = (1, x, y, z)$ and an exponential weight function:

$$\begin{cases} e^{(-r_k/\alpha)^2}, \text{if} & r_k \leq 1 \\ 0, \text{if} & r_k > 1. \end{cases} \tag{3.2}$$

where, $\alpha = 0.3$ and r_k is the distance between the Lagrangian point and the associated k-th Eulerian point normalised over the size of the support domain, r_w:

$$rk = \frac{|\vec{x}_k - \vec{x}_L|}{r_w}.$$

3. Compute the volume force $\vec{F}_L$ for all Lagrangian markers:

$$\vec{F}_L = \frac{U_b - U_l}{\Delta t},$$

   where U_b is the velocity imposed as boundary condition on the marker points.

4. Transfer back $\vec{F}_L$ to the N_e Eulerian lattice points associated with the marked point for each of them, using the same interpolation procedure backwards, and imposing that the total force acting on each single Eulerian point is not changed by the transfer. To obtain this the volume force of a Lagrangian point is calculated as follow:

$$f_{ib}^k = \sum_{l=j}^{N_l} c_j \phi_k^j F_{jL}$$

   where N_L is the number of Lagrangian points associated with eulerian point k. The scaling factor c_j allows the equivalence of the forces before and after the transport, and takes into account the discretization of the immersed surface and the lattice spacing Δx, in terms of volumetric ratio. Indicating with ΔV_e the volume of the single lattice cell and with ΔV_l the volume defined by the area of the triangle A_l of the immersed surface multiplied by a lenght h_l , $\Delta V_l = h_l * A_l$ where h_l id defined by:

$$h_l = \sum_{k=1}^{N_e} \phi_k^j \Delta x$$

   with these relations:

$$c_l = \frac{\Delta V_l}{\sum_{k=1}^{N_e} \Delta V_{ke}}$$

5. Compute the term F_{ib} following the work given by Guo (2002) [12] [2] [4]:

$$F_{ib} = \left(1 - \frac{1}{2\tau}\right) w_i$$

6. Substitution F_{ib} in equation (3.1) for each eulerian Lattice node, recompute distribution function. In this way the forcing term due to presence of the obstacle is transfered to time level $n+1$.

3.2 Fluid-Structure Interaction for rigid body

The total force and total moment acting on the immersed body are evaluated in time by sum of the viscous and pressure stresses over all the tringles that discretize the body surface. For each element, the pressure and the velocity are evaluated in a probe point on the normal $\vec{n}_l$ of the tringle in the positive direction (external for a closed surface) of each triangular element, is possible to set the probe distance from triangle centroid between $0.5\Delta x$ and $1.5\Delta x$, the procedure for calculating the pressure and the velocity is the same of the MLS alghoritm. With velocity on centroid and at the point probe position, is possible to calculate the velocity derivative in normal direction need to evaluate the shear stress. Obtained the pressure p_p value at the probe point, the pressure at marker point is calculated considering the acceleration of the marker itself:

$$p_l = p_p + \frac{\vec{u}_l(t+\Delta t) - \vec{u}_l(t)}{\Delta t} \vec{n}_l$$

$$\vec{F}(t) = \sum_{j=1}^{N_L} (\bar{\tau}_{jl} \cdot \vec{n}_{jl} - p_j \vec{n}_j) A_{jl}$$

$$\vec{M}(t) = \sum_{j=1}^{N_L} \left[\vec{r}_{jl} \times (\bar{\tau}_{jl} \cdot \vec{n}_{jl} - p_{jl} \vec{n}_{jl}) \right] A_{jl}$$

Given the computed values of $F(t)$ and $M(t)$, the linear and angular accelerations are obtained, $u'_c = du(t)/dt = F(t)/M_c$ and $\omega'_c(t) = M(t)/I_C$, with M_c the particle mass and I_c the inertia moment. The linear and angular velocity of the immersed particle are computed as:

$$\vec{u}_c(t) = \frac{2}{3} \left[2\vec{u}_c(t - \Delta t) - \frac{1}{2} u_c(t - 2\Delta t) + \vec{u}'_c(t) \right]$$

$$\omega_c(t) = \frac{2}{3} \left[2\vec{\omega}_c(t - \Delta t) - \frac{1}{2} \omega_c(t - 2\Delta t) + \vec{\omega}'_c(t) \right]$$

After moving the particle the alghoritm restart computing the distribution function at time level $n + 1$. This results in a weak coupling between fluid solution and structure reaction, however it is stable and usable as long as the velocity fluctuations are not too large [16].

3.3 Validation 1: Rotational spheroid of different shape in shear flow

The first group of tests in this chapter concerns the rotational behavior of spheroids immersed in Couette flows. The problem it is widely described in th work of H.Huang at al. (2012) [41]. Furthermore, it was possible to test the behavior for a Reynolds $Re < 1$ number and compare the results of this case with the analytical solution called Jefferey Orbit based on the hypothesis of minimum dissipation energy and valid up to Reynolds numbers of the order of 10^-2. For all the testes the fluid domain, is still a cube, oriented as in fig. (addref) the boundaries are two mobile walls at $y = y_{min}$ and $y = y_{max}$ with opposite velocity of magnitude u_{max}, two boundaries with conditions of periodicity at $z = z_{min}$ and $z = z_{max}$ and two walls $z = z_{min}$ and $z = z_{max}$ with velocity $u_x = u_x = 0$ and $u_z = -u_{max} + (2y/y_{max})u_{max}$. The Reynolds number id defined by:

$$Re = \frac{4Gd^2}{\nu}$$

where $G = 2u_{max}/L_y$ and d is the lenght of semi-major axis.

3.3.1 Test1 Prolate spheroid

A prolate spheroid with axes ratio of 2 is immersed in a Couette flow. The side of the fluid domain has a lenght 4 times the one of major axis of the spheroid. The spheroid is oriented with the minor axis parallel with x axis (vorticity direction) The major semiaxis has a length set at $30\Delta x$, this means that the length of a domain side is $240 * \delta x$. The Reynolds number is set to a value of $0, 5$, in this condition the flow causes a rotation around the x axis with a time variable rotation velocity. The solution is compared with the one provided by the analytical function of Jeffrey in his 1922 work 3.2, see fig. (3.2)·

3.3.2 Test2 Oblate spheroid

An oblate spheroid with minor semi axis of $0.5d$ is immersed in the same domain with one of the major axis oriented as vorticity direction. The studies of Ding and Aidun (1998) [42] and Zettner and

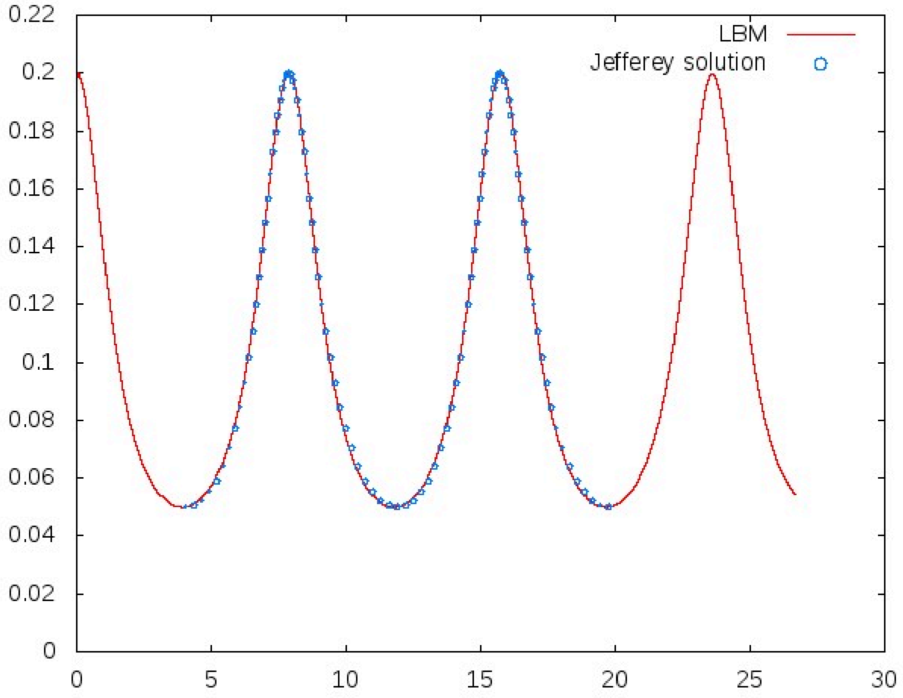

Figure 3.2: Comparison rotational velocity computed by LBM-IB code and the solution provided by Jeffrey relation.

Yoda (2001) [43] establish the existence of critical Reynolds number beyond which the spheroid ceases to rotate, in particular the work of Huang at al.(2012) arrive at a relation between the period T and the numeber Re:

$$T = C(Re_c - Re)^{-1/2} \tag{3.3}$$

with $Re_c \sim 80$ and $C \approx 180$. The result obtained with LBM code are in in fig, 3.3, for three values of Reynolds number: $Re = 50$, $Re = 70$,$Re = 90$. Other simulations with different values of Reynold number between $Re = 50$ and $Re = 90$ are performed to match relation (3.3) and to evaluate the crital Reynolds Number Re_c and the constant C.

The results are shown in fig. 3.4 We obtained a good agreement with a value of $Re_c = 83.2$ and $C = 178.5$.

3.4 Single sphere settling under gravity

The test is the simulation of motion of a sphere falling under gravity in a closed container. Ten Cate and al. [45] have performed a set of experiments based on particle image velocimetry, providing an accurate measure of both the sphere trajectory and velocity from the initial condition with null velocity until rest at the bottom of the channel. The fluid dynamic similitude involves the respect of geometry ratio between box dimensions and sphere diameter, Reynolds number Re and Froude number Fr defined as follow:

$$Re = \frac{\rho D u_{inf}}{\mu}$$

$$Fr = \frac{u_{inf}}{\sqrt{gD}}$$

Where D is the sphere diameter, g is gravity acceleration and u_{inf} is the sedimentation velocity of a sphere in an infinite medium. In order to determine u_{inf}, the relation for drag coefficient C_d of Abraham

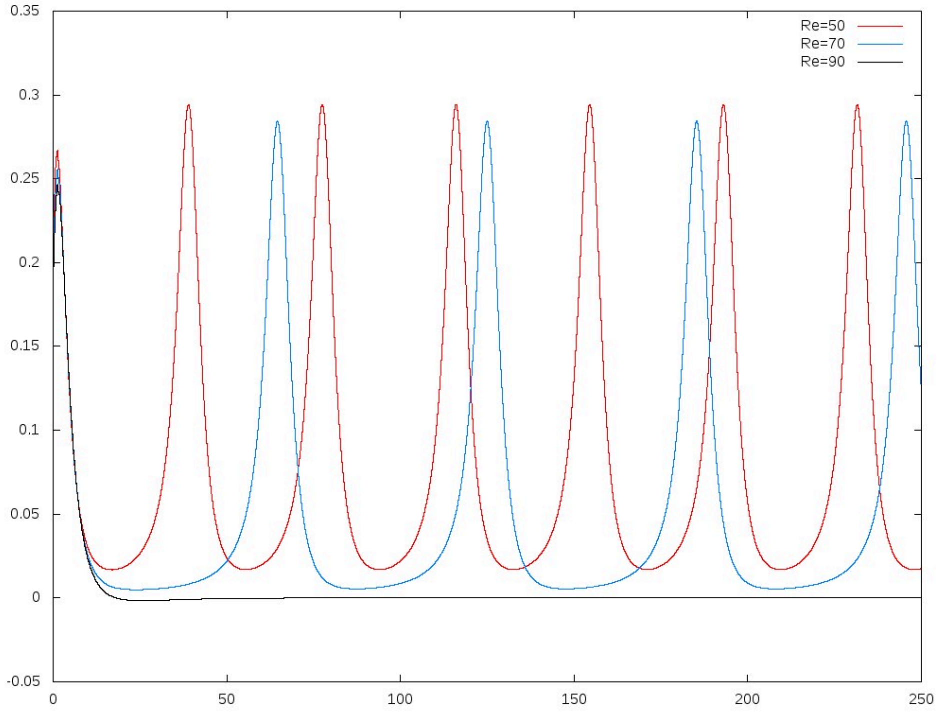

Figure 3.3: rotational velocity function of Reynold number Re, the simulation for $Re = 90$ (black curve) shows a zero constant rotational velocity ($Re > Re_c$)

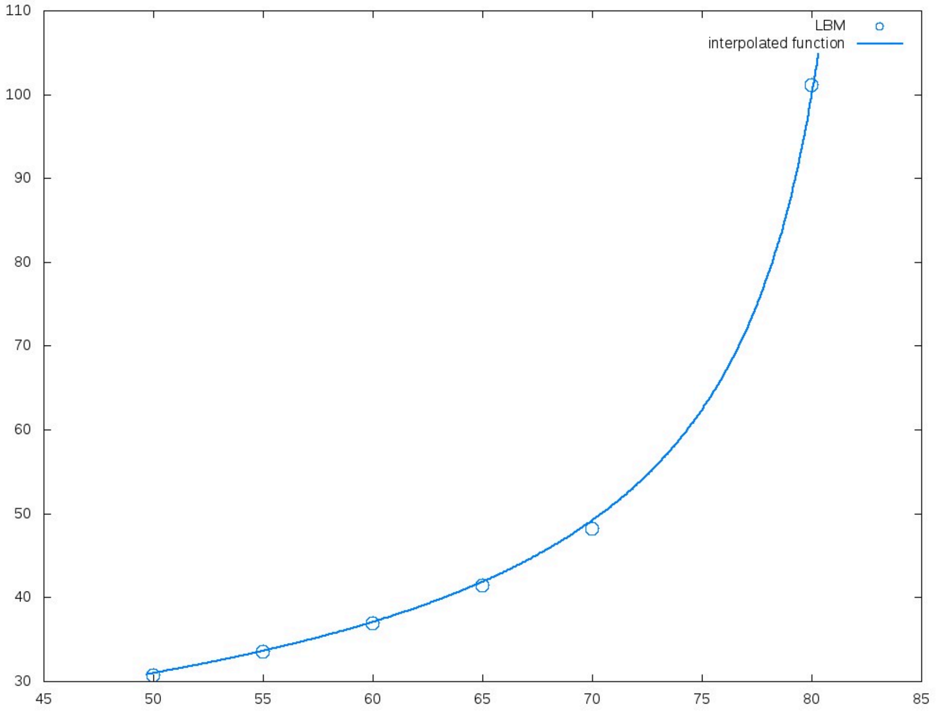

Figure 3.4: Period T function of Reynolds Number for the case of oblate spheroid in shear flow.

1970 [46] is used

$$C_d = C_0 \left(1 + \frac{\delta_0}{\sqrt{Re}}\right)^2 \tag{3.4}$$

Re	γ	u_{inf}	Fr_{inf}
1.5	1.155	0.038	0.0991
4.1	1.161	0.060	0.156
11.6	1.164	0.091	0.237
31.9	1.167	0.128	0.334

Table 3.1: Settings for the case of a sphere settlings under gravity in a closed container

Using the values $C_0\delta_0^2 = 24$ and $\delta_0 = 9.06$, obtaining:

$$u_{inf} = \sqrt{\frac{4gD}{3C_d}(\gamma - 1)} \tag{3.5}$$

Where γ is the density ratio $\gamma = \rho_s/\rho_f$, ρ_f and ρ_s are the fluid and solid (sphere) densities. The computational domain is a box with dimensions $10.67D \times 6.67D \times 6.67D$. Four simulations are performed with the conditions provided in table 3.1. The lattice dimensions $N_x \times N_y \times N_z$ $400 \times 400 \times 640$, this mean a diameter of the sfere of $D_{LBM} = 60$. The sphere sedimentation velocity and trajectory are reported in fig. 3.5, where is shown a comparison with the experimental data of ten Cate el al. [45]

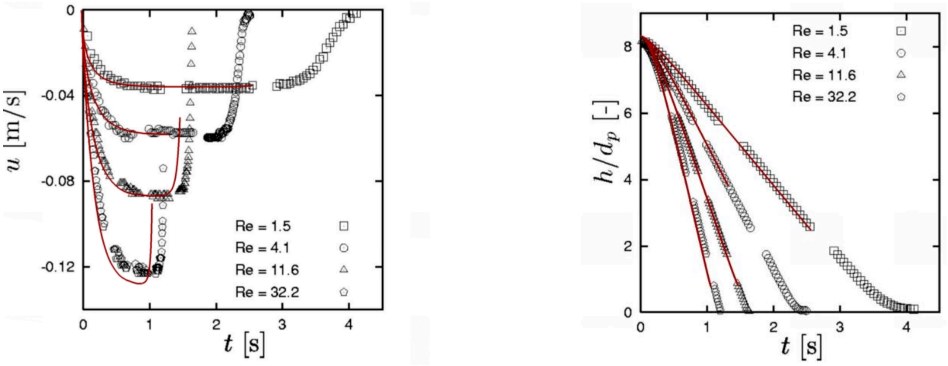

(a)

(b)

Figure 3.5: Sphere under gravity test: comparison of results computed and esperimental ones by ten Cate et al.[45]

Number of CPU	Grid Dimension	Total Simulation Time
1	$100 \times 100 \times 100$	$1680s$
8	$200 \times 200 \times 200$	$1780s$
64	$400 \times 400 \times 400$	$1937s$

Table 3.2: Parallel performance for different lattice dimensions and CPUs used

3.4.1 Computing parallel performance

The last test is been repeated in different condition to test the performance of implementation for parallel computing. In the first set of simulations the number of processors involved is changing with lattice dimension, the results are in tab 3.2. Other simulations are performed with a fixed lattice dimension and changing the number of parallel threads to verify the speed up. The results are shown in fig. 3.6

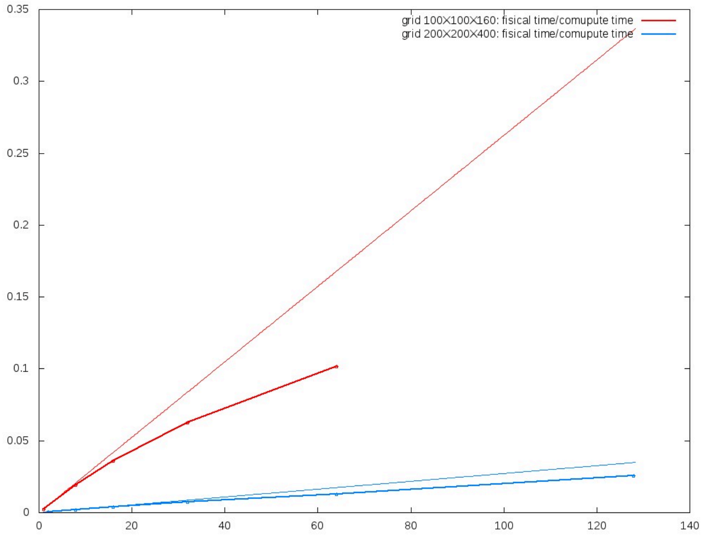

Figure 3.6: Parallel performance: Speedup

Chapter 4

Model for deformable immersed particles

The final objective of the work is the development of a method to study the case of the transport of particles or deformable capsules immersed in Low Reynolds Flows. After having developed a lattice Boltzmann Method for the solution of the fluid domain (lattice) and an alghorithm that solves the case of immersed contours, the final step of this work consists in the introduction of an alghorithm of fluid structure interaction that allows to calculate displacement and deformation of immersed bodies. The immersed body of our actual interest have a boundary surface of membrane type, we consider the internal of the body contains a fluid. The model used is described below.

4.1 Spring-network model

The deformable behavior of the bodies under the calculated loads obtained by solving the flow as described in the previous chapter, is described through a spring-network model. It is based on principle of minimum energy [47]. As we yet discribed the body is discretized with N_l triangles,the idea is to consider the triangles' edges as spring, see fig. 4.1-a The mass of each triangle is considered concentrated in the vertices and uniformly distributed among them. The structure is considered a membrane with a constant thickness.

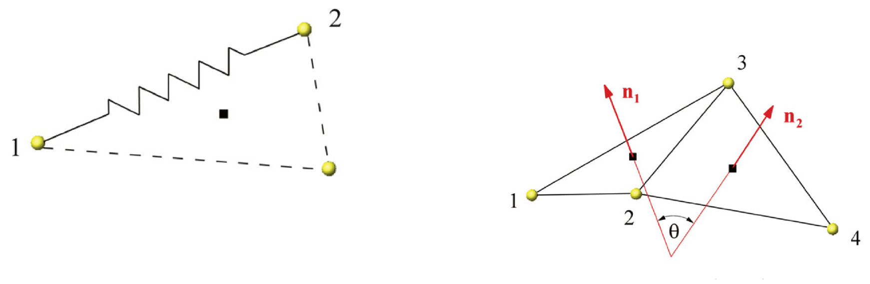

(a) (b)

Figure 4.1: Spring-network model. (a) Spring between two nodes. (b) Two adjacent triangles with normals vectors for bending potential.

For a linear element, the elastic energy is described by:

$$E^e = \frac{k_e}{2}(l - l_0)^2 = \frac{k_e}{2}(s)^2$$

where E^e is the potential energy, k_e is the elastic constant, l is the spring lenght and l_0 the stress-free configuration, so s is the elememt deformation.
For each edge of lenght l the elastic constant is obtained by the model of Van Gelder [48] :

$$k^e = \frac{E^Y h \sum_i A_i}{l^2}$$

where E^Y is the Young modulus for the materials, h is the membrane thickness, i identifies the triangle sharing the selected edge, and A_i is the triangle area. In our cases each edge belongs to two triangles. So we can write:

$$k^e = \frac{E^Y h(A_1 + A_2)}{l^2}$$

The nodal forces corresponding to the elastic energy for nodes 1 and 2 connected by an edge (fig.4.1-a) are obtained considering the derivative of the potenzial energy with respect to displacement:

$$\begin{aligned}\vec{F}_1^e &= -k_e s \frac{\vec{x}_1 - \vec{x}_2}{|\vec{x}_1 - \vec{x}_2|} \\ \vec{F}_2^e &= -k_e s \frac{\vec{x}_2 - \vec{x}_1}{|\vec{x}_1 - \vec{x}_2|}\end{aligned}$$

With this model is considered also the stress related to out-of-plane deformation of two adiacent triangles sharing an edge, this is taken in account by definition of a bending spring. The corrisponding energy involves four nodes. The free elastic energy of the local surface consisting of two triangles, when they were complanar given by:

$$E^b = k_b(1 - \vec{n}_1 \dot{\vec{n}}_2) = k_b(1 - \cos\theta)$$

where $\vec{n}_1$ and $\vec{n}_2$ are the unit vector normal to the triangles elements, see fig. 4.1-b, θ is the angle between these vectors and k_b is the bending constant. If the triangle has a non zero angle in the undeformated condition, the bending energy is given by [49]:

$$E^b = k_b\left[1 - \cos\left(\theta - \theta_0\right)\right]$$

where θ_0 is the angle value in the stress free configuration. About the bending constant k_b, it is related to the equivalent averaged bending modulus of the structure B by the relation [66]:

$$k_b = B\frac{2}{\sqrt{3}}$$

The nodal forces, obtained from the energy derivative are given by:

$$\begin{aligned}F_1^b &= \beta_b\left[b_{11}(\vec{n}_1 \times \vec{x}_{32}) + b_{12}(\vec{n}_2 \times \vec{x}_{32})\right] \\ F_2^b &= \beta_b\left[b_{11}(\vec{n}_1 \times \vec{x}_{13}) + b_{12}(\vec{n}_1 \times \vec{x}_{34} + \vec{n}_2 \times \vec{x}_{13}) + b_{22}(\vec{n}_2 \times \vec{x}_{34})\right] \\ F_3^b &= \beta_b\left[b_{11}(\vec{n}_1 \times \vec{x}_{21}) + b_{12}(\vec{n}_1 \times \vec{x}_{42} + \vec{n}_2 \times \vec{x}_{21}) + b_{22}(\vec{n}_2 \times \vec{x}_{42})\right] \\ F_4^b &= \beta_b\left[b_{11}(\vec{n}_1 \times \vec{x}_{23}) + b_{12}(\vec{n}_2 \times \vec{x}_{23})\right]\end{aligned}$$

with:

$$b_{11} = -\frac{\cos\theta}{|\vec{n}_1|^2}$$
$$b_{12} = \frac{1}{|\vec{n}_1|^2|\vec{n}_2|^2}$$
$$b_{22} = -\frac{\cos\theta}{|\vec{n}_2|^2}$$

and

$$\beta_b = k_b \frac{\sin\theta\cos\theta_0 - \cos\theta\sin\theta_0}{\sqrt{1-\cos^2\theta}}$$

It is possible to introduce other potencial energy terms related to the triangle area changing, global or for each triangle, and related to global volume changing [47], [51], [52]. At this point it is possible to compute the displacement of each single node, and conseguently the deformed configuration of the membranous body is obtained and its displacement in the fluid field. The dynamic equation of motion is given:

$$m_n\vec{x}_i = \vec{F}_i^e + \vec{F}_i^b + \vec{F}_i^f + \vec{F}_i^g \tag{4.1}$$

Where $\vec{F}_i^f$ is the hydrodinamc force and $\vec{F}_i^g$ is the gravity force. For the hydrodynamic loads it must be considered also the contribute due to the presence of fluid in the internal side of the surface, the procedure to calculate it is the same seen in chapter 3, in particular the force on the j-th marker lagrangian point in the (addref formula) is modified as:

$$F_j^f = \left[(\bar{\tau}_j^+ - \bar{\tau}_j^-)\cdot\vec{n}_j^+ + (p_j^+ - p_j^-)\vec{n}_j^+)\right]$$

where the subscript $(+)$ indicates quantities calculated for the external side, indeed the suscript $(-)$ indicate the internal side of body surface The equation (4.1) is solved through an explicit velocity Verlet alghoritm, which has proved to be more stable than an explicit euler integration in this work case studies.

4.2 2D Tests and Results: comparison of Kinematic and dynamic forcing strategies

In the following 2D tests, the method involving the combined Lattice Boltzmann and Immersed Boundary seen in chapteers 2 and 3, together with the deformable model seen in the previous sections, named *Dynamic IB* is used to predict the transport of inertial deformable capsules. The results are compared with those obtained from conventional approach, named LBM – *Kinematic IB*, where capsules move with the same velocity of the surrounding fluid. Several test cases have been considered for assessing the accu-racy and efficiency of the Dynamic over Kinematic IB scheme, including the stretching of circular capsules in shear flow, the transport in a plane Poiseuille flow of circular and biconcave capsules, with and with-out inertia. The results are published in the paper [56]:
Kinematic and dynamic forcing strategies for predicting the transport of inertial capsules via a combined lattice Boltzmann – Immersed Boundary method by A.Coclite, S.Ranaldo, M.D. de Tullio b, P. Decuzzi and G. Pascazio, in Computers and Fluids 180 (2019).

4.2.1 Stretching of a circular capsule in shear flow

First, the two proposed IB schemes are validated against the data published for the dynamics of a deformable capsule in a shear flow by Sui et al. . Referring to fig.4.2 a, a circular capsule of diameter d is placed at the center of a square box with the side length $H = 10d$. The capsule diameter is discretized by $40\Delta x$ and the average length of the linear elements composing the membrane boundary is equal to $0.3\Delta x$. The imposed shear rate is $y = 2u_{max}/H$, with u_{max} the velocity magnitude of the top and bottom walls, and the resulting Reynolds number is $Re = \gamma d^2/\nu$ $(= 0.05)$. The behavior of the capsule is regulated by the elastic constant k_s , which is computed through the dimensionless shear rate $G = \nu_{ref}\rho_{ref}\gamma d/k_s$, and by the bending resistance modulus, $E_b = k_b/k_s r^2$. Lastly, the mass of the capsule is determined considering the solid vesicles as dense as the surrounding fluid, $\rho_s/\rho_f = 1$. The flow field is initialized with a linear velocity profile given by $u_x(t = 0) = \gamma(y - H/2) = 2u_{max}(y - H/2)/H$, $u_y(t = 0) = 0$. The accuracy of the two IB schemes is characterized by computing the time variation of the Taylor deformation parameter, $D_{xy} = (a - b)/(a + b)$, where a and b correspond to the major and minor radii of the capsule. This parameter is plotted in Fig.4.2 b for $E_b = 0$, $G = 0.0125, 0.04$, and 0.125. The solid lines are for the Dynamic IB scheme, the dashed lines are for the Kinematic IB scheme, the black dots are for the benchmark data by Sui et al.. An excellent agreement is found for the smaller shear rates $(G = 0.0125 and G = 0.04)$. The relative error with respect to benchmark data:

$$\epsilon_{Dyn/Kin} = \frac{D_{xy,Dyn/kin} - D_{xy,Sui}}{D_{xy,Sui}}$$

is smaller then 1% for both schemes. Note that the slight increase in relative error with the nondimensional shear rate is due to the constitutive model used for the capsule membrane. Indeed, it is well known that a spring model is accurate for small deformations with respect to the original configuration. Then, the bending resistance of the capsule is varied (E_b = 0,0.025, 0.05, 0.1 and 0.2) having fixed $G = 0.04$. Results are provided in fig.4.2 d, and the corresponding relative error is reported in fig.4.2 e. Even in this case, the relative error is well confined within 1%. Given the weak coupling between the structural and fluid solution in time, the results for capsules with stiffer membranes may suffer of numerical instabilities. Indeed, the fluid may experience large displacement gradients due to the elastic response of relatively rigid capsules (see $E_b = 0.2$ in fig.4.2 d). It is noteworthy that the *Dynamic IB*, which is well suited for $\rho_s/rho_f > 1$, can accurately reproduce the benchmark results even in the case of $\rho_s/rho_f = 1$. The equilibrium configurations of the capsules obtained by the *Dynamic IB* and *Kinematic IB* are drawn in fig.4.2 f. for $E_b = 0$, $G = 0.0125, 0.04$, and 0.125. Collectively, these data indicate that the two IB schemes return almost identical results within the tested ranges of G and E_b . Importantly, for the case in hand, the computational time needed by the *Dynamic IB* scheme to perform 10000 time steps was about 7% higher than that required by the Kinematic IB scheme, with a computational domain of 4000000 points.

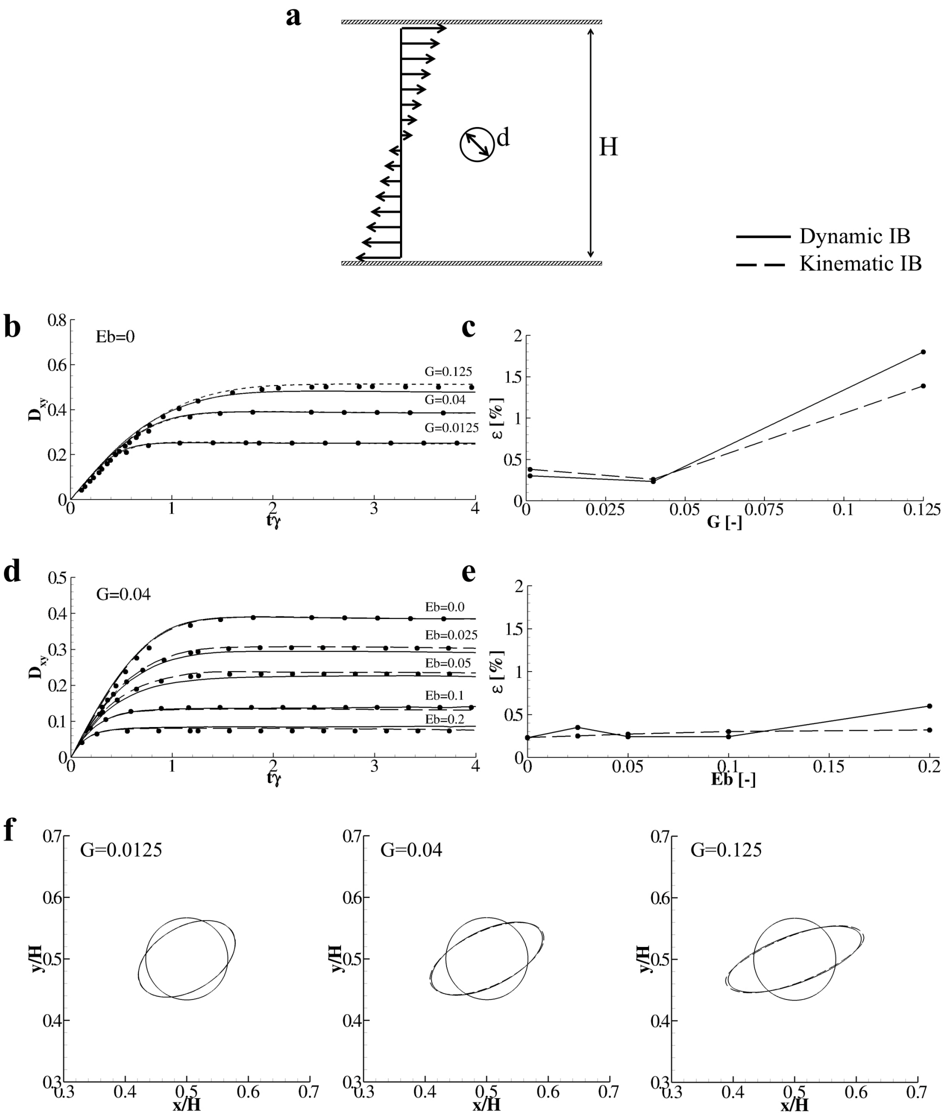

Figure 4.2: Deformation of a circular capsule in shear flow.
a. Schematic representation of a circular capsule under linear shear flow.
b. Variation of the Taylor parameter over time as function of the dimensionless shear rate G ($E_b = 0$).
c. Relative error (%) with respect to the benchmark data obtained by varying G for $E_b = 0$.
d. Variation of the Taylor parameter over time as function of the bending stiffness $E_b(G = 0.04)$.
e. Relative error (%) with respect to the benchmark data obtained by varying E_b for $G = 0.04$.
f. Configurations of circular capsules for $E_b = 0$ and $G = 0.0125$,0.04, and 0.125 as compared to the initial unperturbed configuration (circle). (Solid line: Dynamic IB; Dashed line: Kinematic IB; Symbols: benchmark data by Sui et al.)

4.2.2 Transport of a circular capsule in a plane-Poiseuille flow

The dynamics of a capsule with $\rho_s/\rho_f = 1$ within a plane-Poiseuille flow is considered. The capsule has a diameter of $7\mu m$ and is immersed in a 2D channel with a height $H = 15\mu m$ and a lenght uqual $3H$. A sketch of the physical problem is drawn in fig.4.3 a. Three different initial positions of the capsule within the channel are considered, whereby the center of the capsule can be at 6.5, 7.5 and $8.5\mu m$ away from the lower wall. The capsule surface is discretized with a network of linear elements with an average length equal to $0.3\Delta x$. Simulations are run at $Re = 0.01$ and with four capillary numbers, namely

$= u_{max}\nu_{ref}/k_s = 10^{-1}$, 10^{-2}, 10^{-3}, and 10^{-4}. In the initial condition, the flow field is at rest with $\vec{u} = 0$ amd $p = p_{ref}$. The plane-Poiseuille flow is established by imposing a parabolic longitudinal velocity profile at the inlet section, $u_x(x = 0) = -u_{max}(|1 - y/H|^2 - 1)-$, and a constant pressure at the outlet section, $p(x = 3H) = p_{ref}$. This, indeed, implies the realization of the plane-Poiseuille linear pressure drop between the inlet and the outlet sections:

$$\frac{\partial p}{\partial x} = -u_{max} 2 \rho_{ref} \mu_{ref} \frac{4}{H^2}.$$

In this case, the comparison between the two IB schemes is provided in terms of the capsule perimeter variation with respect to its original configuration, $\delta p(t) = (p(t) - p_0)/p_0$ and of the swelling ratio, S_w, defined as the ratio between the capsule area $A(t)$ at time t and the area associated with a circle of perimeter p, used as reference $(S_w(t) = A(t)/p^2(t)/4\pi$. A direct comparison of the capsule membrane at different time points is also provided for the two IB schemes. Even in this case, the two IB schemes are in good agreement within the small deformations range, $10^{-4} \leq Ca \leq 10^{-2}$. Quantitatively, the difference between the two schemes is computed by the relative error at $tu_{max}/H = 2.0$, $\epsilon = (\delta p_{Dyn} - \delta p_{kin})/\delta p_{kin}$. This error depends on the considered capillary number:
$\epsilon(Ca = 10^{-4}) = 0.988 \times 10^{-4}$,$\epsilon(Ca = 10^{-3}) = 3.61 \times 10^{-4}$,$\epsilon(Ca = 10^{-2}) = 1.313 \times 10^{-3}$, $\epsilon(Ca = 10^{-1}) = 3.80 \times 10^{-3}$.
Interestingly, the transient dynamics prescribed by the two IB schemes differs for $Ca = 10^{-2}$ and 10^{-1} whereas the capsule shapes almost perfectly overlap for $Ca \leq 10^{-2}$.
It should be here emphasized that the hydrodynamic stresses associated with the fluid pressure field in the first instants of the simulation are small but certainly not null. Therefore, while in the Dynamic IB scheme capsules start to deform following the external hydrostatic pressure already at time zero, in the *Kinematic IB* scheme the initial zero velocity field results in a null velocity of the Lagrangian markers on the capsule surface, which consequently cannot feel the external pressure. This fundamental difference between the two schemes is responsible for the differences observed in capsule shapes within the initial time steps. It is worth noting that, in the case of large deformations, the authors needed to refine the Lagrangian mesh in order to ensure a Lagrangian spacing always higher than the Eulerian one during the transport dynamics of the capsule. This is strictly required for the Dynamics IB scheme in order to correctly impose the no-slip conditions, avoiding "holes" on the body surface. The linear springs network used for $Ca = 10^{-1}$ has an average length equal to $0.2\Delta x$. These trends are also confirmed by analyzing the swelling ra- tio distributions in time. In particular, S_w indicates how much the particles deviates from the circular shape ($S_w = 1$) reaching the final *bullet-like* configuration. Five capsule configurations, corresponding to different time instants, for $Ca = 10^{-1}$ and 10^{-4}, are shown for both schemes in fig.4.3 d and e, for three different initial locations within the channel. A good agreement is confirmed for $Ca = 10^{-4}$, whereas a slight difference is observed for $Ca = 10^{-1}$, in agreement with the behavior already documented for δp and S_w.

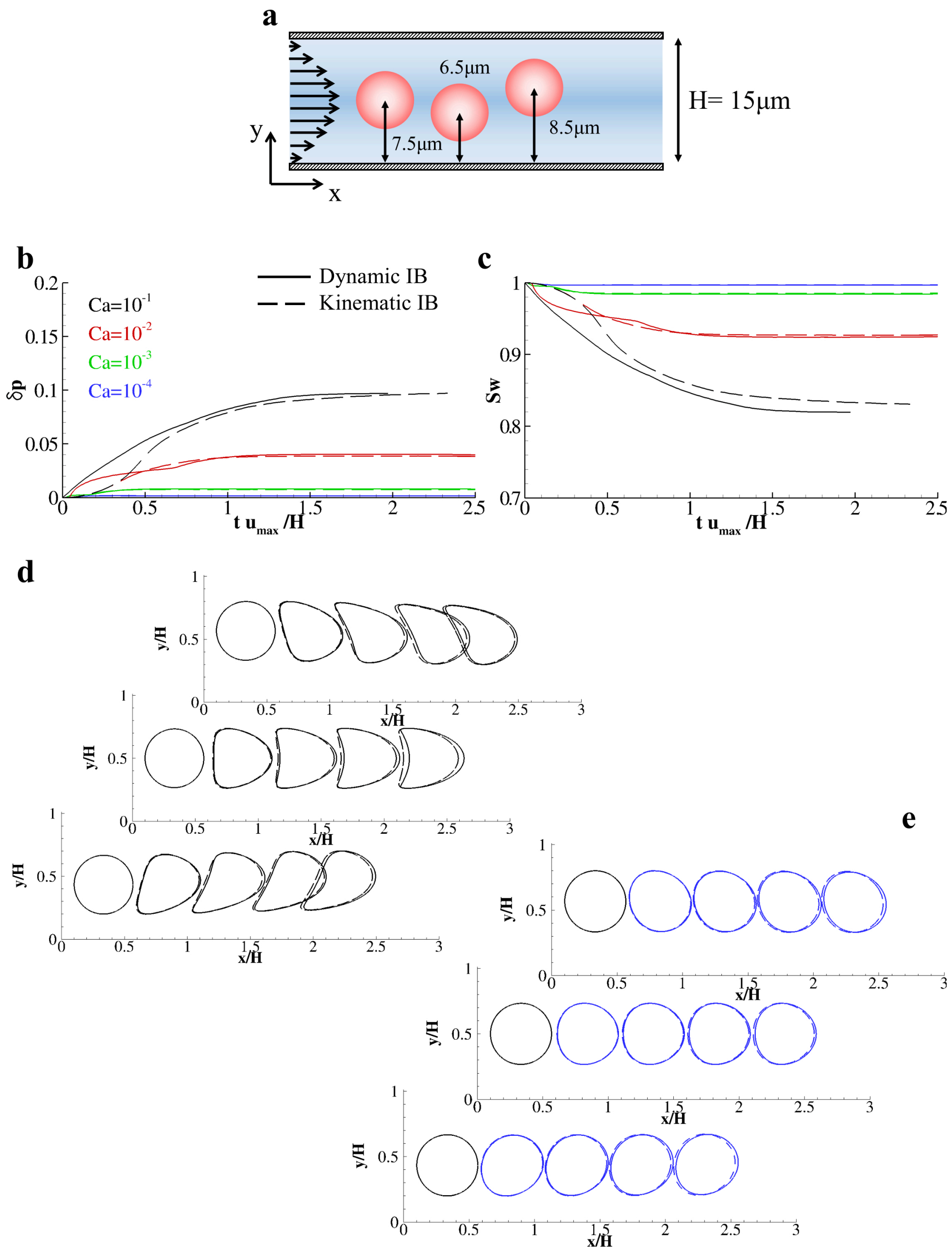

Figure 4.3: Transport of a circular capsule in plane-Poiseuille flow.
a. Schematic representation of circular capsules in a rectangular channel located at different distances from the bottom wall.
b. Variation of the capsule relative perimeter over time as function of the capillary number Ca.
c. Variation of the capsule swelling ratio over time as function of the capillary number Ca.
(d,e). Capsules for $Ca = 10^{-1}$ (d) and $Ca = 10^{-4}$ (e) taken at $tu_{max}/H_{max} = 0$, 0.5, 1.0, 1.5, 2.0. (Solid line: Dynamic IB; Dashed line: Kinematic IB).

4.2.3 Transport of a biconcave capsule in a plane-Poiseuille flow

In the same channel and with the same initial and boundary conditions of the previous test case, the behavior of biconcave capsule is also studied fig.4.4 a. The stress-free biconcave shape is obtained as the

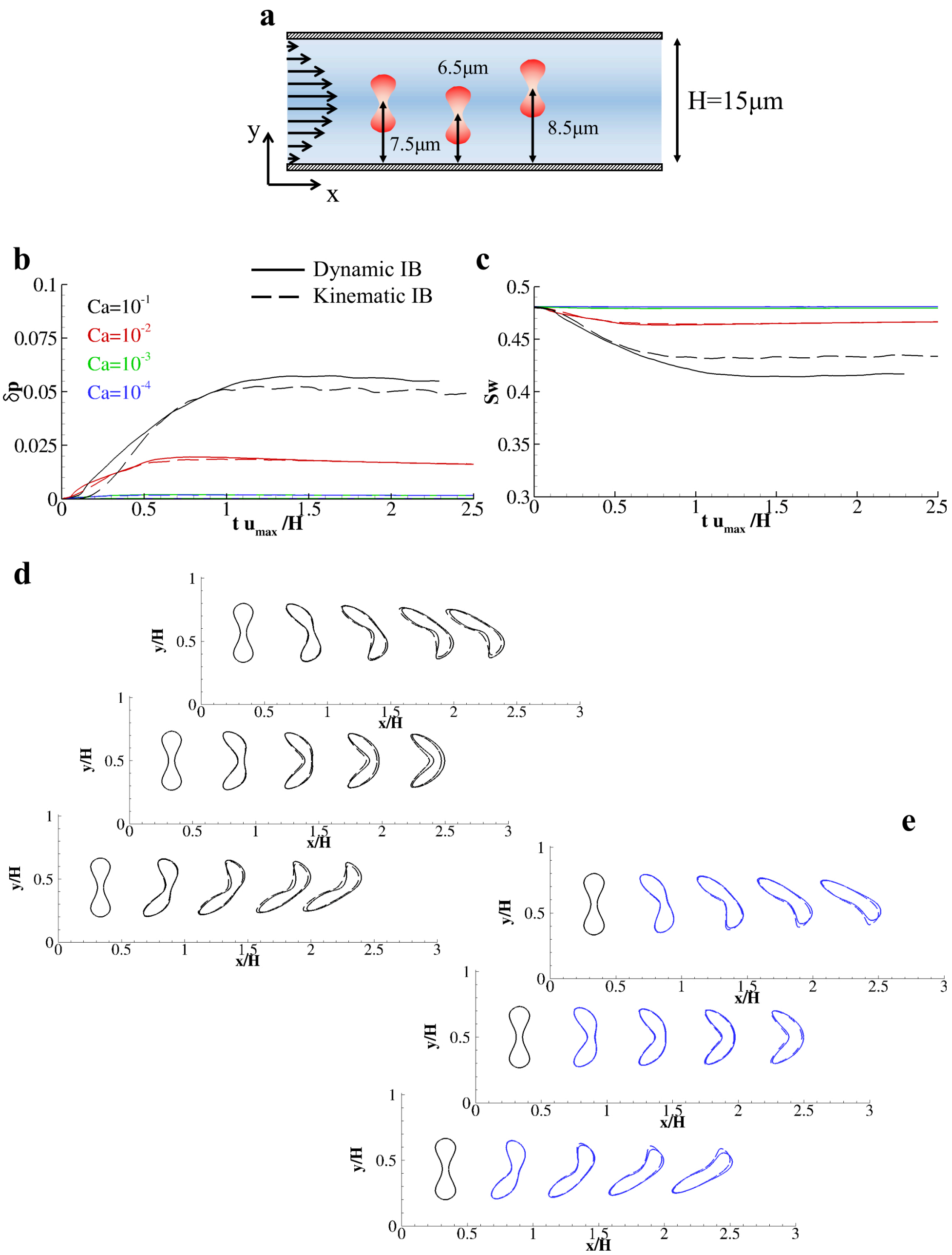

Figure 4.4: Transport of a biconcave capsule in plane-Poiseuille flow.

a. Schematic representation of biconcave capsules in a rectangular channel located at different distances from the bottom wall.

b. Variation of the capsule relative perimeter over time as function of the capillary number Ca.

c. Variation of the capsule swelling ratio over time as function of the capillary number Ca

(d,e). Capsules for $Ca = 10^{-1}$ (d) and $Ca = 10^{-4}$ (e) taken at tu_{max}/H_{max} = 0,0.5, 1.0, 1.5, 2.0. (Solid line: Dynamic IB; Dashed line: Kinematic IB).

parametrization of the median section of a capsule, resembling a red blood cell,

$$\begin{cases} x = a\alpha \sin(q) \\ y = a\frac{\alpha}{2}\left(0.207 + 2.003 \sum^2 q - 1.123 \sin^4 q\right) \cos q \end{cases}$$

where a is 0.122, α is equal to $3.5\nu m$, and the parameter q varies within $[-0.5\pi, 1.5\pi]$. For the above parametrization, the swelling ratio in the stress-free configuration is equal to 0.481. The major axis, the initial perimeter, and the solid mesh discretization are fixed within this simulation. Also in this case, the two IB schemes predict a similar behavior fig.4.4 b and c. The time variation of δp obtained with the two schemes overlaps for $Ca = 10^{-4}$, and $Ca = 10^{-3}$. Interestingly, the stretching of the biconcave capsule is about half of that obtained in the case of the circular capsule. This feature can be addressed considering the unique shape of red blood cells that would maximize the area-to-volume ratio. fig.4.4 d and e provide the qualitative comparison between the capsule shapes as predicted by the two IB schemes.

4.2.4 Transport of multiple biconcave cells in plane-Poiseuille flow

In this test case, sixteen biconcave capsules are transported in a plane-Poiseuille flow at $Re = 0.01$ (fig.4.5 a). Collisions among the capsules are modeled through a potential field centered in each Lagrangian markers that limits to Δx the minimum separation distance between two interacting markers. Precisely, two-body interactions are modeled through a repulsive potential centered in each vertex of the immersed particles. The repulsive force is such that the minimum allowed distance between two adjacent particles is Δx. The force $\vec{F}_1^{pp}$ acting on the vertex 1, at a distance d_{12} from the vertex 2 of an adjacent particle, is directed in the inward normal direction identified by $\vec{n}_1^-$ and is given by:

$$\vec{F}_1^{ip} = \frac{10^{-4}}{8\sqrt{2}} \sqrt{\frac{\Delta x}{d_{1,2}^5}} \vec{n}_1^- .$$

The elastic modulus of the capsules is $Ca = 10^{-2}$, to recover the physiological relevant conditions. The total amount of fluid enclosed by the membranes is about 30% of the total computational domain area (fig. 5a), thus reproducing a 30% hematocrit. Contour plots for the velocity components and pressure field at $2tu_{max}/H$ are provided for both the Kinematic and Dynamic IB schemes. A qualitative good agreement between the two schemes for the velocity fields is documented in fig.4.5 b, c and fig.4.5 d, e, for the horizontal and vertical velocity components, respectively. Some differences are instead observed for the pressure contours, as shown in Fig.4.5 f and g. Precisely, the pressure fields appear quite similar when the interaction potential between cells is active (cells with other cells in their neighborhoods) and differs when the hydrodynamics alone dominates the transport (see black circles in fig. 4.5 f and g). Interestingly, three different capsule behaviors can be identified depending on the relative location of the capsule within the flow field: bulk capsule, whereby capsules are surrounded by other capsules; front capsule, referring to capsules moving at the head of the shoal; rear capsule, related to capsules moving at the back of the shoal (Fig.4.6 a). As compared to bulk capsules, front and rear capsules stretch about 1.4 and 0.8% more, for both IB schemes (Fig.4.6 b). Indeed, hydrodynamics stresses generated within the meniscus between two adjacent capsules locally oppose deformations.

Despite the complex dynamics depicted in this test case, the agreement between the two IB schemes continues to be confirmed. Specifically, the relative errors between the two solutions is computed using δp and returns $\epsilon(front) = 0.683 \times 10^{-3}$,$\epsilon(bulk) = 1.64 \times 10^{-3}$, and $\epsilon(rear) = 0.622 \times 10^{-3}$, depending on the capsule location. The time distribution of swelling ratio and perimeter variation show similar behaviors, drawing a picture in which, overall, bulk capsules are less stressed than the front and rear capsules (Fig.4.6 c). Finally, for this test case, accounting for a domain of 540000 Eulerian points and 16000 Lagrangian markers distributed over 16 biconcave capsules, the computational time needed by the Dynamic IB scheme to perform 10000 time steps was about 16.7% higher than that required by the Kinematic IB scheme.

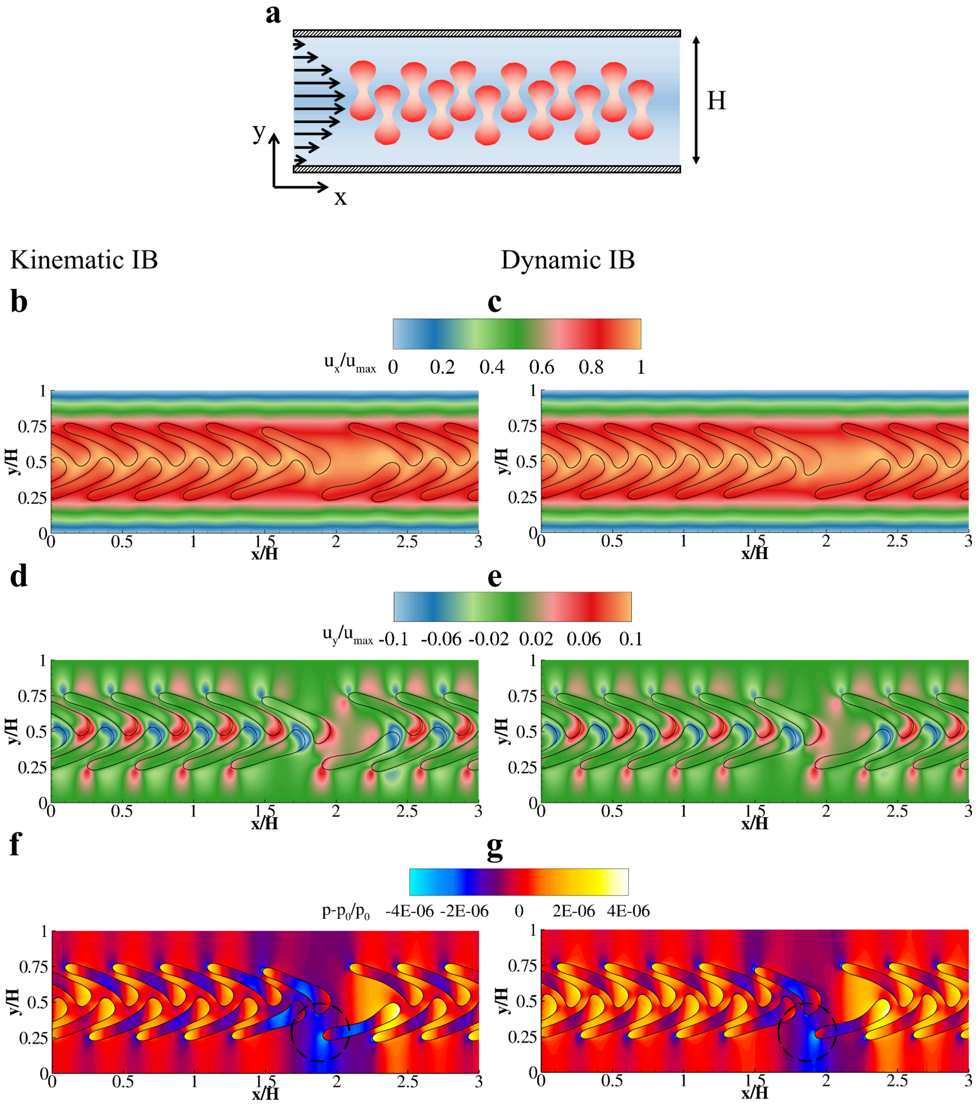

Figure 4.5: Transport of multiple biconcave capsules in a plane-Poiseuille flow.
a. Schematic representation of biconcave capsules in the rectangular channel.
(b,c). Contour plot of the horizontal velocity component.
(d,e). Contour plot of the vertical velocity component.
(f,g). Contour plot of the relative pressure with enlighten the two zones in which the two approaches differ (black dashed circles).

4.2.5 The role of inertia in the transport of a circular capsule in linear and parabolic flows

The role of the inertia is assessed by computing the behavior of a circular capsule for different values of the membrane density in two different configurations: the dynamics of the capsule with $Ca = 10^{-3}$, $E_b = 0.1$ in a Couette flow (linear flow) and the detachment of a capsule from the wall in a plane-Poiseuille flow (parabolic flow). Note that this specific simulation can easily be performed using the Dynamic IB scheme, while the standard Kinematic IB scheme can solely be used for $\rho_s/rho_f = 1$. Firstly, a linear laminar flow is established in a rectangular computational domain by moving the upper wall ($y = H$) with $u_{max} = \nu Re/H$ ($Re = 10, H = 100\Delta x$). The diameter of the particle is $d = 0.25H$ (Fig.4.7 a) and the membrane thickness equals $0.01d$. The rationale of this test case is to elucidate the role of capsule inertia

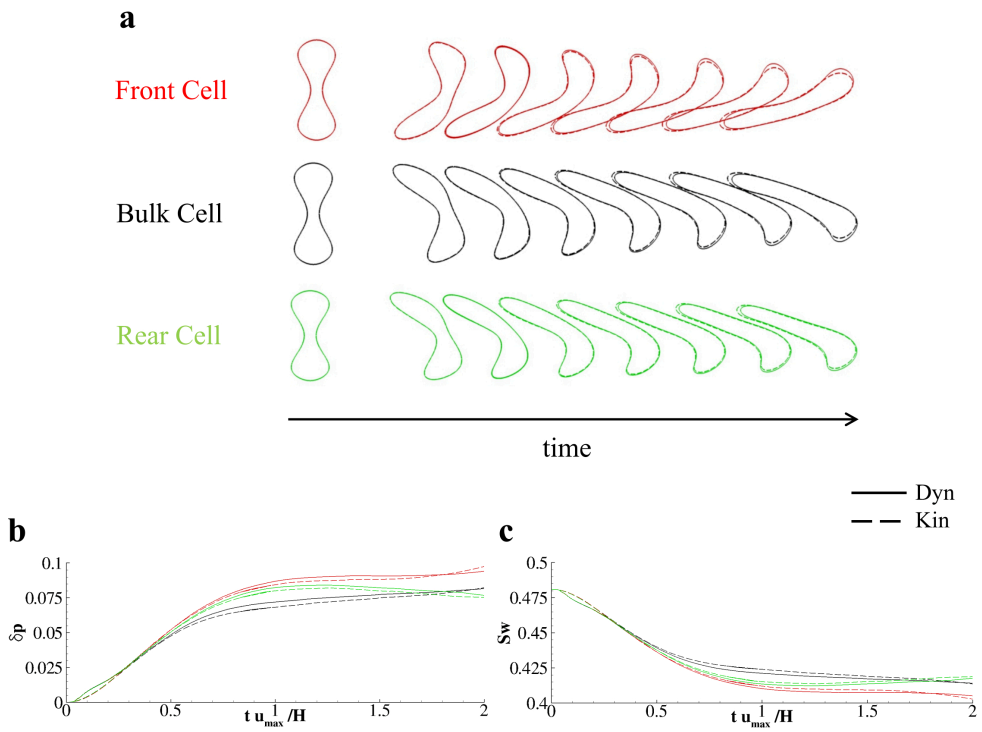

Figure 4.6: Biconcave capsules regimens in Poiseuille Flows.

a. Front, Bulk, and Rear cells successive configurations for $Ca = 10^{-2}$ taken from $tu_{max}/H_{max} = 0$ to $tu_{max}/H_{max} = 2$ with nondimensional time interval equal to 0.25.

b. Perimeter variation distributions over time for the Front, Bulk, and Rear cells.

c. Swelling ratio distributions over time. (Solid lines: Dynamic IB scheme; Dashed lines: Kinematic IB scheme).

as the sole independent parameter of the simulation. Indeed, an increase of the membrane mass reflects into an increase of the capsule inertia. This is expected to facilitate the lateral migration of the capsule by increasing the rotational lift component. As expected, all capsules reach the theoretical equilibrium position of $0.5H$ regardless of their mass as depicted in Fig.??b. As previously studied by the authors, the pressure field across the particle boundary is one of the components of the total lift acting on the immersed body: capsules tend to generate a symmetric pressure field across their boundary. Such fields are drawn for a representative capsule with $\rho_s/rho_f = 2$ taken at two different time instants, namely one as soon as the capsule reaches the equilibrium height (Fig.4.7 c) and the other in the end of the capsule journey (Fig.4.7 d). Lastly, the distributions of δp and S_w are reported in Fig.4.7 e and f. Interestingly, the capsules deform almost immediately after being released and keep their deformed configuration for all the lateral migration process due to the linearity of the velocity flow field. The role of the inertia is further demonstrated studying the detachment of a single capsule in a parabolic flow with $Re = 10^{-2}$ (Fig.4.8 a). In particular, as the ratio between the capsules and the surrounding fluid increases, the distributions of δp and S_w deviate more from the case of membranes having the same fluid density (Fig.4.8 b and c). Indeed, a capsule would move towards different flow regions of higher velocities if it lags the flow or, in other words, if the slip velocity between the capsule and the undisturbed fluid is greater than zero. The velocity of the undisturbed flow is the velocity that the fluid would have if no particle was immersed in. Such parameter, u_x, slip, depends on the inertia moment of the immersed body, so that, in this case, on the membrane mass. Increasing the inertia causes an increase of the time needed to equilibrate the slip velocity profile across the immersed bodies, as demonstrated in Fig.4.8 d [24]. Here, the distribution of u_x, slip is taken at $tu_{max}/H = 1.5$ along the capsules boundaries by varying counterclockwise the radial coordinate θ . Notably, the larger displacement between these distributions is found in the lower region of the particles, around $3/4\pi$. In this zone, the particles are navigating along streamlines with lower velocity (not strong velocity gradients), while pressure stresses are large and induce lubrication lift (Fig.??d and e). These differences are qualitatively depicted in Fig.4.8 f where five membrane configurations, taken at subsequent five time instants, are presented.

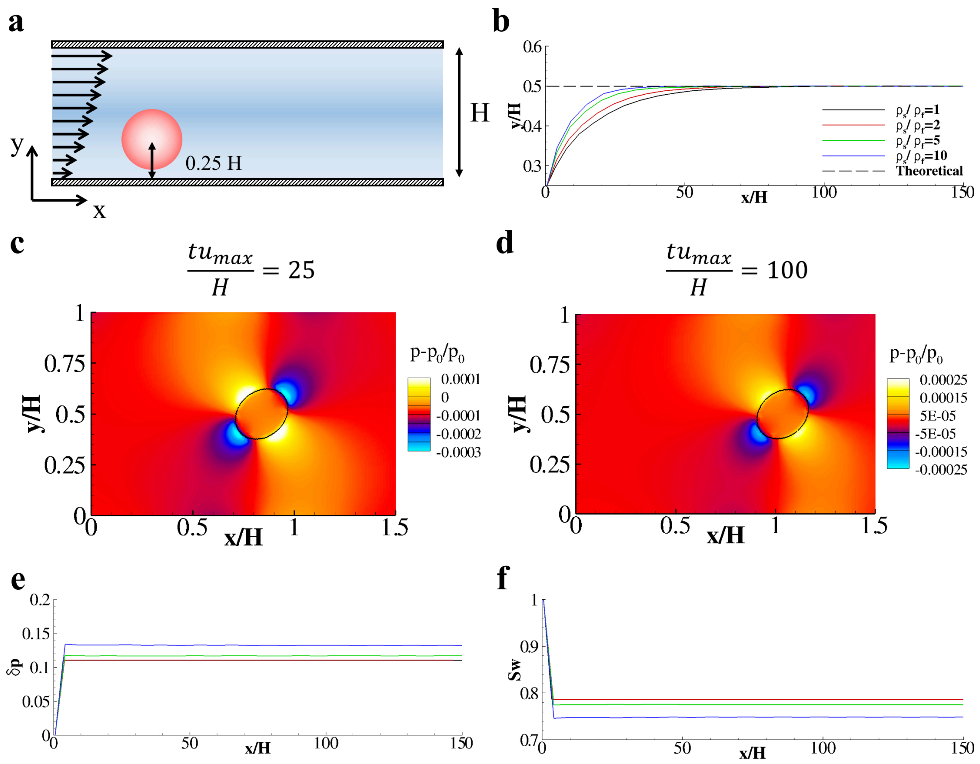

Figure 4.7: The role of inertia in the transport of a circular capsule in a linear flow.
a. Schematic representation of an initially resting circular capsule in a rectangular channel with centroid at $0.25H$ from the bottom wall.
b. Trajectory of the centroid of the circular capsule for different values of the relative density ρ_s/ρ_f.
c. Pressure field around the circular capsule for $\rho_s/\rho_f = 2$ taken at $tu_{max}/H = 25$.
d. Pressure field around the circular capsule for $\rho_s/\rho_f = 2$ taken at $tu_{max}/H = 100$.
e. Variation of the capsule relative perimeter over time as function of the relative density ρ_s/ρ_f.
f. Variation of the capsule swelling ratio over time as function of the relative density ρ_s/ρ_f.

4.3 2D Test and Results: Adhesion Model

A fundamental step in the rational design of vascular targeted particles is the firm adhesion at the blood vessel walls. It is demonstrated that the model predicts with good accuracy the rolling velocity of tumor cells over an endothelial layer in a microfluidic channel. The particle surface is decorated with ligand molecules, mediating specific adhesive interaction with counter-molecules (receptors) distributed over the vessel walls. These interfacial molecular adhesive forces are computed through a probabilistic approach determining bond formation and destruction over the entire particle surface (Sun and Munn 2008). The near-wall dynamics of circular and elliptical particles, with two aspect ratios, is analyzed at three Reynolds numbers (Re = 0.01,0.1, 1.0), for three different densities of the surface ligands and two different values of the ligand-receptor chemical affinity. A direct comparison between computational

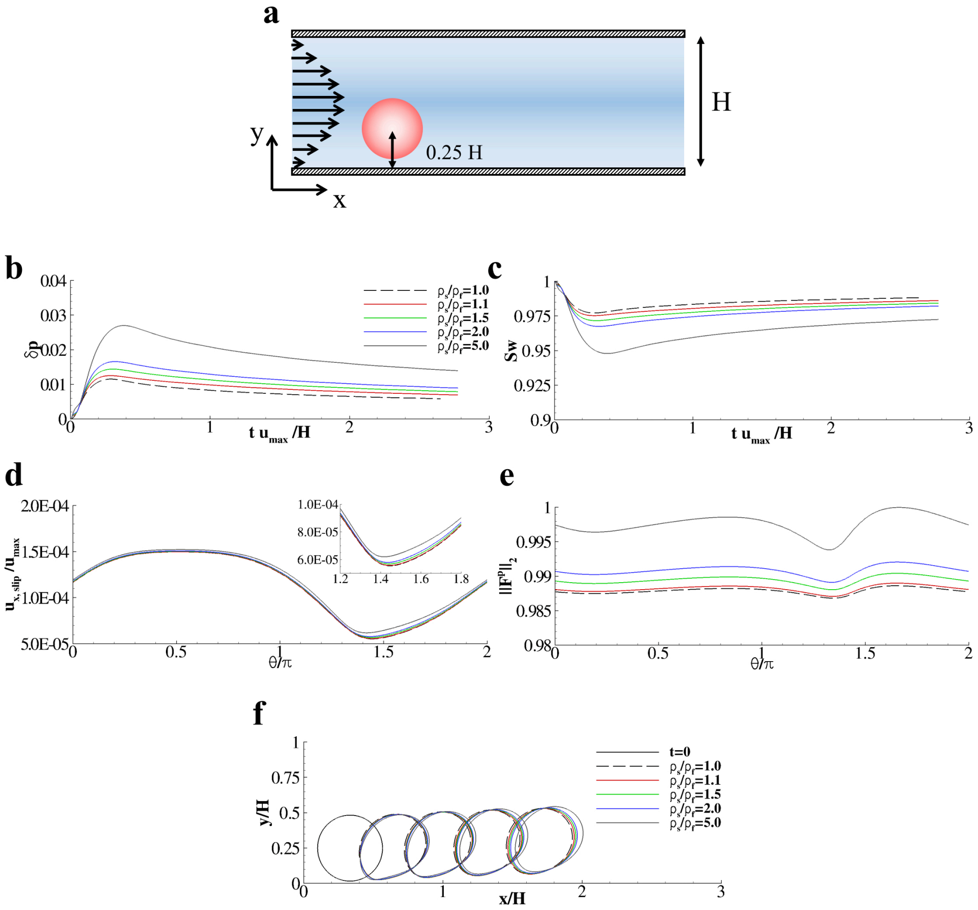

Figure 4.8: The role of inertia in the transport of a circular capsule in plane-Poiseuille flow.
a. Schematic representation of circular capsules in a rectangular channel initially in contact with the bottom wall.
b. Variation of the capsule relative perimeter over time as function of the relative density ρ_s/ρ_f.
c. Variation of the capsule swelling ratio over time as function of the relative density ρ_s/ρ_f.
d. Longitudinal slip velocity measured on the capsules perimeter at $tu_{max}/H = 2.0$ for different values of the relative density ρ_s/ρ_f.
e. Module of the pressure force measured on the capsules perimeter at $tu_{max}/H = 2.0$ for different values of the relative density ρ_s/ρ_f.
f. Capsules for different values of the relative density ρ_s/ρ_f taken at $tu_{max}/H = 0$, 0.5, 1.0, 1.5, 2.0.

predictions and experimental measurements is also presented. Particle–wall interaction maps are derived d in terms of particle geometries (circular, elliptical with aspect ratios 2 and 3), surface ligand densities (0.3, 0.5, 0.7 and 0.9), ligand-receptor bond strengths (1 and 2) and Reynolds numbers ($Re = 0.01$,0.1 and 1.0). Depending on these conditions, four different particle–wall interaction regimens are identified, namely not adhering, rolling, sliding and firmly adhering particles. The proposed computational strategy can be efficiently used for predicting the near-wall dynamics of particles with arbitrary geometries and surface properties and represents a fundamental tool in the rational design of particles for the specific delivery of therapeutic and imaging agents. This model and results are published in paper[**?**]:
Predicting different adhesive regimens of circulating particles at blood capillary walls, by A. Coclite,H. Mollica, S. Ranaldo, G. Pascazio, M.D. de Tullio,P. Decuzzi. In Microfluid Nanofluid (2017) 21:168

4.3.1 Wall-Particle Interaction

The adhesion model used in the present work is based on the works by Sun et al. (2003, 2008). Ligand and receptor molecules are distributed over the particle and vessel wall surfaces, respectively. Ligand molecules are modeled as linear springs which, by interacting with wall receptor molecules, tend to establish bonds (ligand-receptor bonds) and support a mechanical force $f_{l,b}$ given as:

$$\vec{f_{l,b}} = \sigma(y_l - y_{cr,eq})\vec{n_l}$$

with y_l the bond lenght, $y_{cr,eq}$ the equilibrium bond lenghtand σ the spring constant. The receptor density is assumed uniform; the solid wall is supposed completely covered by receptive molecules. In the present model, all springs have the same spring constant, σ. The total adhesive force, $\vec{F_b}$ is obtained by integrating $\vec{f_{l,b}}$ over the particle perimeter. Bonds can be only generated if the minimum separation distance between the particle boundary and the wall is smaller than a critical value, $y_{cr} = 6.8 \times 10^{-3}H$. The equilibrium bond length, resulting in a null force, is chosen as $y_{cr,eq} = 0.5y_{cr}$. All lengths are normalized by the channel height, H. The linear spring constant is computed in 2 lattice units and non-dimensionalized through the term $\rho_{ref}\nu^2/H$, where ρ_{ref}, H, and ν, are reference density, length and kinematic viscosity, respectively. The bond formation is regulated by a forward probability function

$$P_f = 1 - exp(-K_f Nl\Delta t)$$

with K_f forward bond rate and Nl the number of ligand actually probing the surface (number of active elements) over the total number of linear elements. At each time step, a pre-existing bond can be destroyed according to the reverse probability function

$$P_r = 1 - exp\left[-k_{r0}exp\left(\frac{(\sigma-\sigma^*)(y_l - y_{cr,eq})^2}{2K_bT}\right)\Delta t\right]$$

Here k_{r0} is the reverse bond rate, σ^* is the equilibrium spring constant (taken as 0.5σ), anf K_BT is the thermal potential (Sun et al. 2003; Sun and Munn 2008). The equilibrium spring constant σ^* enables to model two different classes of ligand-receptor bonds: 'slip' bonds for $\sigma > sigma^*$, where forces exerted on the bond facilitate disentanglement, and 'catch' bonds for $\sigma < sigma^*$, where forces exerted on the bond facilitate entanglement. Here, by fixing $\sigma^* = 0.5\sigma$, slip bonds are considered which are far more common in the case of leukocyte and cancer cell rolling/adhesion (Marshall et al. 2003). A Van der Waals-like potential is implemented to model the particle–wall interaction. The force $\vec{F_w}$ is so applied along the solid walls positive normal directions into the particle centroid (Sun et al. 2003)

$$\vec{F_w} = \frac{H_k}{8\sqrt{2}}\sqrt{\frac{r}{\epsilon^5}}\vec{n}$$

being $\vec{n}$ the solid wall normal direction unit vector, H_k the Hamaker constant, r the particle radius and ϵ the separation distance between the particle and the wall. The Hamaker constant is non-dimensionalized through the term $\rho_{ref}H\nu^2$.

4.3.2 Cell rolling in a capillary flow

To reproduce typical capillary flow conditions, a single-channel microfluidic chip is realized in PDMS, following standard fabrication procedures (fig.4.9 a) (Manneschi et al. 2016). The resulting microfluidic chip has a channel with width $W = 210\nu m$, height $H = 42\nu m$ and length $L = 2.70cm$. Top and side views as well as an optical microscopy image of the chip are presented in fig.4.9 a. 10^{-6} colon rectal

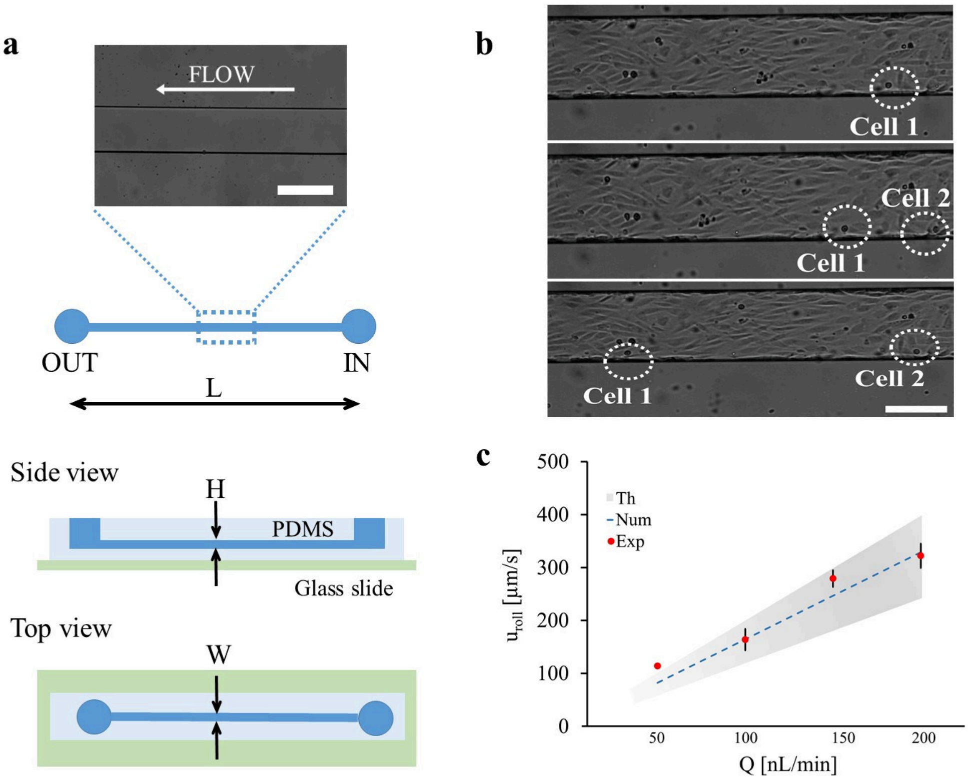

Figure 4.9: HCT-15 cells rolling on an HUVEC monolayer into a single-channel microfluidic chip. a Schematic representation of the single-channel microfluidic chip with definition of the main geometric quantities. From top to bottom: bright field epi-fluorescent microscope image of the region of interests (scale bar $250\mu m$); side and top views of the chip ($L = 2.7cm$, $H = 42\mu m$, $W = 210\mu m$). b Representative images of HCT-15 cells rolling over a confluent monolayer of HUVECs (×10 magnification, scale bar $250\mu m$). c Rolling velocity of HCT-15 under four different flow conditions (50, 100, 150 and $200nL/min$) estimated via numerical and theoretical analyses.

tumor cells (HCT-15) are injected in the endothelialized channel via a syringe pump at different flow rates, namely $Q = 50, 100, 150$ and $200nL/min$. The vascular transport of HCT-15 cells is monitored for about $15min$ using a fluorescent microscope, and the rolling velocity is estimated within the region of interest. Note that the considered flow rates Q correspond to physiological and tumor characteristic wall shear rates S, namely $S = 13.5, 27, 40.5$ and $54s^{-1}$ ($S = 6Q/(WH^2)$). Also, the corresponding mean flow velocities U are $94.48, 188.9, 283.4$ and $377.9\nu m/s$ ($U = Q/(WH)$), respectively. Still images of cells rolling over the endothelial monolayer within the chamber are presented in fig.4.9 b, at different time points. The rolling velocity u_r is defined as the ratio between the distance traveled by the cell and the period of observation and is derived by post-processing the fluorescent microscopy images. As shown in fig.4.9 c, the rolling velocity (red dots) increases linearly as the flow rate Q grows ($R2 = 0.966$), ranging from 113.9 ± 4.13 for $50nL/min$ to 322.2 ± 22.8 for $200nL/min$. This was expected and confirmed by theoretical and numerical predictions. The theoretical rolling velocity u_{th} is derived assuming the cell as a rigid sphere of diameter d rolling in a rectangular channel pushed by a flow with rate Q, as derived for a channel of rectangular cross section (Bird 2002), so that

$$u_{th} = \frac{3}{2}\frac{Q}{WH}\left[1 - \left(1 - \frac{d}{H}\right)^2\right]$$

Considering that the diameter of HCT-15 cells ranges between 14 and $20/num$ ($d = 15 \pm 3\nu m$), it results in $u_{th} = 83.15 \pm 19.7, 166.1 \pm 39.4, 249.0 \pm 59.1$ and $333.0 \pm 78.7\nu m/s$, for each of the four considered flow rates. This rolling velocity is also estimated using the present LB–IB model assuming the cell as a circular particle, settled at a distance $3 \times 10^{-3}H$ from the wall and with a ligand density 0.3. The assumed ligand density value of 0.3 returns a good agreement between the experimental and numerical predictions for the cell rolling velocity over four different flow rates. The ligand density represents the ratio between the number of ligand molecules on the circulating cell and the number of receptor molecules distributed over the endothelial cells lining the blood vessel walls. As expected, both the numerical and theoretical rolling velocities vary linearly with Q and are in very good agreement with each other ($R^2 = 0.994$). The experimental, theoretical and numerical rolling velocities are all plotted in fig.4.9 c, for the four flow rates Q. Given the variation in cell diameter, shadowed areas are used to present the rolling velocities, whose upper and lower limits are associated with the bigger and smaller cell diameters, respectively. The present LB–IB model accurately predicts the rolling velocity of tumor cells over a wide range of flow rates.

4.3.3 Modeling the adhesion dynamics of near-wall circulating particles

In this section, the adhesive dynamics of particles circulating in close proximity of the blood vessel walls is predicted employing the present LB–IB computational approach. Vascular adhesion is assessed in terms of physiological parameters, such as the local hemodynamic conditions Reynols number $Re = Hu_{max}/\nu$, based on the upper wall velocity, u_{max}, the capillary height, H, and the reference kinematic viscosity, ν_{ref} ; particle parameters such as the particle shape circular and elliptical; and density of ligand molecules (ρl) decorating the particle perimeter. The computational domain resembles the near-wall region in a capillary flow and is limited at the bottom ($y = 0$) by a fixed wall (the vessel wall in a blood capillary) and at the top ($y = H$) by a moving wall (interface between the cell-free layer and the core of the blood capillary) (fig.4.10 a). Within this domain, a linear shear rate is imposed and the upper wall has a velocity u_{max}. The height H of the computational domain coincides with the height of the microfluidic chip used before for the experimental validation. The computational domain is confined within the area $[0, 10H] \times [0, H]$, where H is discretized with 200 points. Periodic boundary conditions are imposed on the two sides ($x = 0 and x = 10H$); zero slip velocities are imposed at the bottom ($u = 0$) and top ($u = u_{max}$) walls so that the linear flow field follows the relationship $u_x(0, y) = u_{max}y/H = (Re \cdot \nu_{ref}/H)y/H$. Particles,initially at rest, are paced in the computational domain at a separation distance from the bottom wall equal to $y_0 = 3 \times 10^3 H$. Three different geometries are considered for the particles, namely circular, elliptical with an aspect ratio 2 and elliptical with an aspect ratio 3 (fig.4.10 a). The characteristic size is chosen as to keep constant the total area enclosed by the particle, namely $A = 0.025H^2$. Thus, the circular particle has a diameter of $0.18H$, and the elliptical particles have axial lengths equal to $0.25H \times 0.125H$ and $0.31H \times 0.103H$, respectively. On the particle perimeter, ligand molecules are uniformly distributed with a density ρ_l of $0.3, 0.5, 0.7$ and 0.9 (fig.4.10 b, c). On the vessel walls, a receptor density equal to 1 is imposed. The ligand-receptor bonds are characterized by an adhesive bond strength σ and a biochemical affinity $k_f/k_{r,0} = 8.5 \times 103$.

4.3.4 Vascular adhesion dynamics for circular particles

Data on the adhesive dynamics of circular particles are shown in fig.4.11, for $Re = 0.01, 0.1$ and 1.0. A circular particle, initially settled in close proximity of the vessel wall ($y_0 = 3.0 \times 10^3 H$) (fig.4.11 a), rapidly forms ligand-receptor bonds initiating the adhesion process. Note that the initial separation distance y_0 is smaller than the critical distance for bond formation ($y_{cr} = 6.8 \times 10^3 H$; dashed lines in fig. 4.11). The equilibrium position of the particle with respect to the wall is given by y_{min}, the minimum

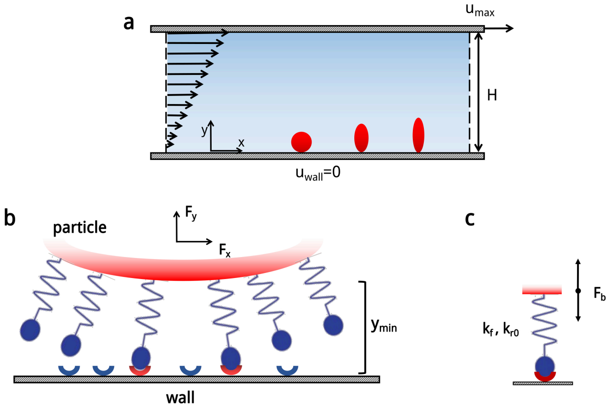

Figure 4.10: Particle transport in a linear laminar flow. a Schematic representation of the computational domain. b Ligand distributed over the particle perimeter interacting with receptors distributed over the vessel wall. c Ligand-receptor bond modeled as a spring with characteristic forward k_f and reverse k_{r0} strengths.

separation distance, which is plotted in fig.4.11 b, f, respectively, for $Re = 0.1$ and 1.0. The particle with a ligand density $\rho_l = 0.3$ moves away from the wall returning an equilibrium separation distance $y_{min} = 7.6 \times 10^{-3}H$, which is larger than the critical distance for bond formation. Thus, for $\rho_l = 0.3$ and smaller, the ligand density is insufficient to induce the formation of any stable bonds and the particle moves away from the wall not adhering particle. For larger ligand densities, the separation distance at equilibrium reduces returning values of $6.67 \times 10^{-3}H$, $6.29 \times 10^{-3}H$ and $6.3 \times 10^{-3}H$, for $\rho_l = 0.5$, 0.7 and 0.9, respectively. These are all cases where the equilibrium position is smaller than the critical bond distance y_{cr} , and stable ligand-receptor bonds are formed. Indeed, as ρ_l increases, the hydrodynamic forces exerted over the particle are redistributed over a larger number of ligands, thus diminishing the deformation of each ligand-receptor bonds and moving the particle closer to the wall (fig.4.11 b, f). As documented in Fig.4.11 c, g, the percentage of active ligands increases with ρ_l; in other words, the number of closed ligand-receptor bonds grows with the number of ligands decorating the particle perimeter. Note that, since ligand-receptor binding is defined in a statistical manner, the number of bonds oscillates over time around an average value. For $\rho_l = 0.3$, the number of active bonds is zero (not adhering particle), whereas it grows to $0.020, 0.036$ and 0.048, for $\rho_l = 0.5, 0.7$ and 0.9, respectively. Oscillations in the number of active ligands appear as bands in fig.4.11 c, g. It is here important to highlight that, due to the small region of contact between a circular particle and the wall, only a small number of ligand-receptor bonds are formed even in the case of high ligand densities. As from fig.4.11 c, g, the percentage of active ligands is equal to 2% for $\rho_l = 0.5$ and grows only up to $\sim 5\%$ for $\rho_l = 0.9$.

The kinematic parameters, namely the angular rotation θ and longitudinal velocity u_x of the particle, are presented in the remaining insets of fig.4.11. The variation of θ over time is given in fig.4.11 d, h. It shows a steady and linear increase in θ, thus implying a constant angular velocity Ω of the particle over the wall—rotating, not adhering particle. The rotational velocity reduces as the number of ligand-receptor bonds increases and is equal to $\Omega H/u_{max} = 0.29$,0.25, 0.125 and 0.125, respectively, for $\rho_l = 0.3$, 0.5, 0.7 and 0.9, at $Re = 0.1$. For larger Reynolds numbers ($Re = 1.0$), the angular velocity Ω exhibits a negligible variation with ρ_l, possibly because of the larger hydrodynamic dislodging forces. In this condition, $\Omega H/u_{max}$ is equal to 0.29, 0.284, 0.280 and 0.280.

Finally, the normalized longitudinal velocity u_x/u_{max} of the particle is plotted versus time in fig.4.11 e, i. Even for this physical quantity, oscillations appear around an average value, following what has been already reported for the number of active ligands. Oscillations are larger for the smaller Reynolds numbers. Indeed, for $Re = 0.1$, the average longitudinal velocity is nearly zero in the case of $\rho_l = 0.7$ and 0.9 and grows up to 4.08×10^{-2} for $\rho_l = 0.5$. For $\rho_l = 0.3$, the normalized longitudinal velocity is 4.80×10^{-2} with no oscillation in that the particle is not adhering to the wall and travels as a rigid body passively transported by the blood flow. For $Re = 1.0$, oscillations are smaller and the longitudinal velocity higher due to the larger hydrodynamic dislodging forces. For $Re = 0.01$, all particles exhibiting a ligand density $\rho_l \geq 0.5$ have zero rotational and longitudinal velocity, implying that these particles can form stable bonds with the wall—firmly adhering particles. Differently, particles with $\rho_l < 0.5$ roll without adhering to the wall—rolling, not adhering particles.

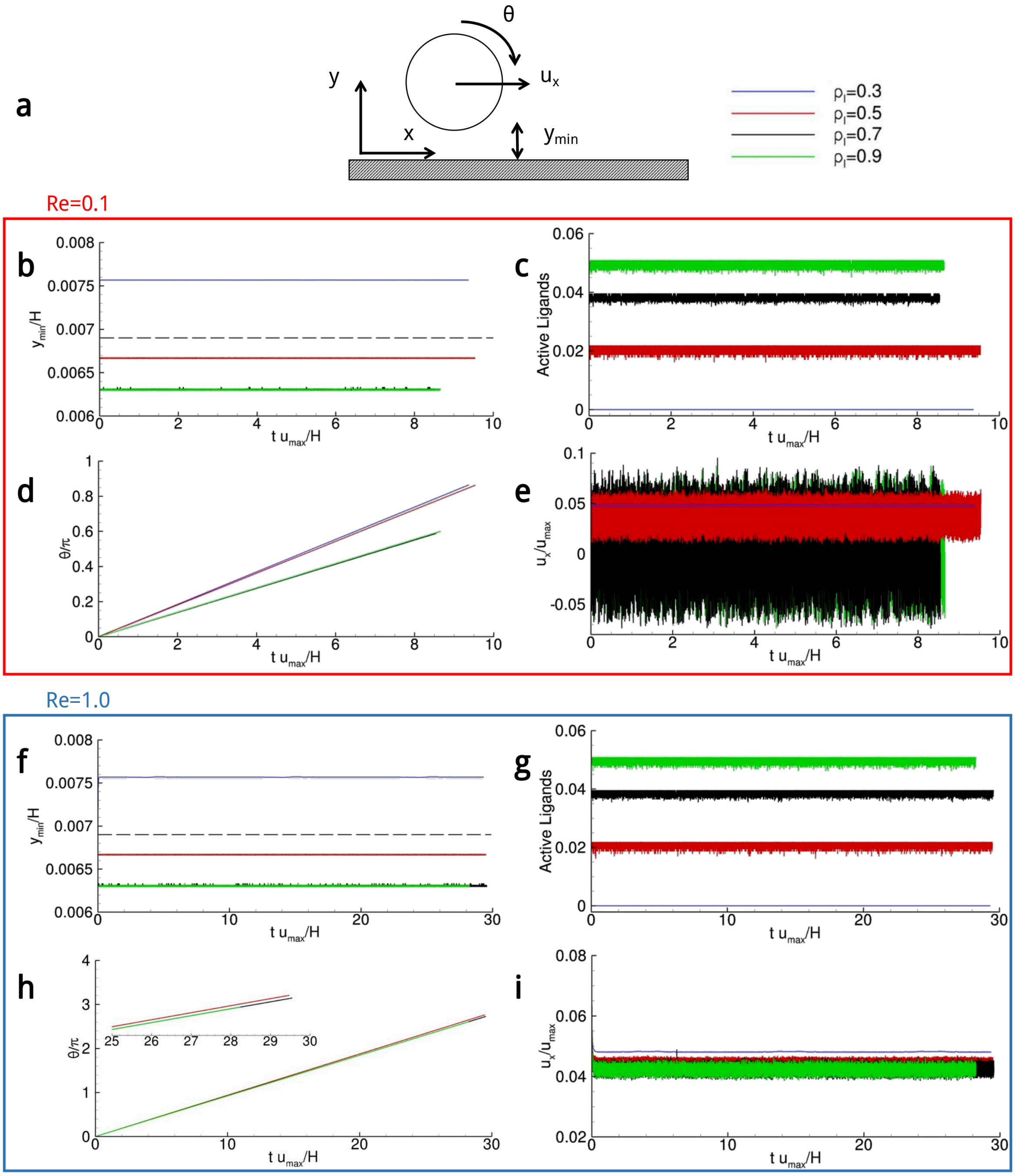

Figure 4.11: Vascular adhesion of circular particles ($\sigma = 2$). a Schematic representation of the problem. b, f Particle separation distance from the wall versus time. The dashed line corresponds to y_{cr}. c, g Active over total number of ligands versus time. d, h Angular rotation, θ, versus time where the inset presents a magnified view within the interval $25 \leq tu_{max} \leq 30$. e, i Normalized rolling velocity versus time.

4.3.5 Vascular adhesion dynamics for elliptical particles

Data on the adhesive dynamics of elliptical particles are shown in fig. 4, for $Re = 0.01$, 0.1 and 1.0 and for aspect ratios equal to 2 and 3. The elliptical particle, initially settled in close proximity of the vessel wall ($y_0 = 3.0 \times 10^3 H$) and with its major axes pointing orthogonally to the wall, rapidly forms ligand-receptor bonds initiating the adhesion process (fig. 4a). Note that the separation distance y_0 is smaller than the critical distance for bond formation ($y_{cr} = 6.8 \times 10^{-3}H$). At low Reynolds number, the adhesion dynamics of elliptical particles is qualitatively similar to that of circular particles. As shown in fig. 4b, the equilibrium position y_{min} is rapidly reached and preserved for the whole simulation period. At first, an abrupt variation in y_{min} is observed, which is related to the initial orientation of the particle with respect to the flow field and its sudden rotation. Also, as compared to circular particles, the equilibrium position y_{min} is slightly higher for a given ligand density ρ_l. This could possibly be ascribed to higher hydrodynamic forces exerted over elliptical particles. Very differently, at $Re = 1.0$ and for sufficiently low ligand densities ($\rho_l = 0.3$), firm deposition of elliptical particles on the wall is impaired and the dislodging forces are strong enough to induce a periodic particle rotation over the wall—rolling, not adhering particle. This is shown in fig. 4f where y_{min}/H oscillates and stays constant (transient adhesion), only for a small portion of the observation time.

Furthermore, the number of closed ligand-receptor bonds is larger for elliptical particles at all given ρ_l, but for $\rho_l = 0.3$ (fig. 4c, g). Indeed, elliptical particles expose a larger portion of their perimeter to the wall allowing for a larger percentage of ligands to be engaged with their counter-molecules (receptors) on the wall (> twofold). Also note that, for $\rho_l = 0.3$, the number of closed ligand-receptor bonds is equal to zero for both circular and elliptical particles.

The angular rotation θ is plotted in fig. 4d, h. For $Re = 0.1$ (fig. 4d), particles move from the original vertical position ($\theta = 0$) and progressively deposit on the wall tending to the more stable configuration $\theta = \pi/2$. This rotation occurs quite abruptly for ρ_l larger than 0.3. Differently, for $Re = 1.0$ (fig. 4h), the rolling and not adhering particle ($\rho_l = 0.3$ and $Re = 1.0$) shows a continuously growing θ with spikes in angular velocities Ω (local derivative of θ with respect to time) corresponding to a quasi-vertical position of the particle. For larger ligand densities, θ reaches the steady-state value of $\theta = \pi/2$, implying that the particle does not rotate anymore after laying down on the wall. Finally, the normalized longitudinal velocity u_x/u_{max} is plotted in fig. 4e, i. For all considered cases, the velocity is not zero but constant for the whole observation period besides for the rolling and not adhering particle (fig. 4i). The not zero velocity implies that the not rotating elliptical particles, once deposited horizontally over the wall, tend to slide longitudinally breaking old bonds at the trailing edge, forming new bonds at the leading edge and along the particle body—sliding, not adhering particles. Indeed, the larger the number of active ligands, the lower the sliding velocity of the particle.

For Re $= 0.01$, all particles exhibiting a ligand density $\rho_l \geq 0.5$ have zero rotational and longitudinal velocity, implying that these particles can form stable bonds with the wall—firmly adhering particles. Differently, particles with $\rho_l < 0.5$ roll without adhering to the wall—rolling, not adhering particles.

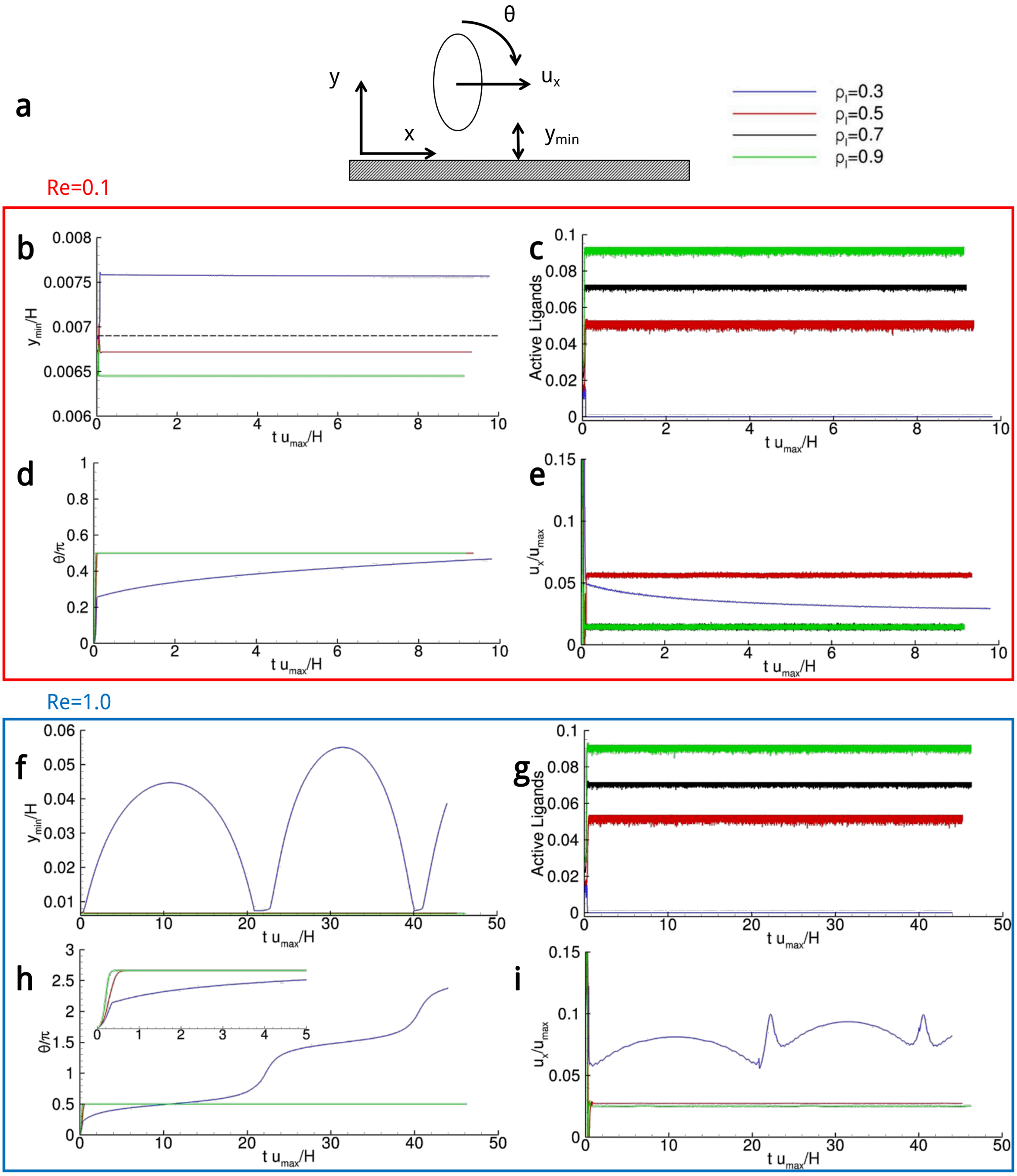

Figure 4.12: Vascular adhesion of elliptical particles ($\sigma = 2$). a Schematic representation of the problem. b, f Particle separation distance from the wall versus time. The dashed line corresponds to y_{cr}. c, g Active over total number of ligands versus time. d, h Angular rotation, θ, versus time where the inset presents a magnified view within the interval $0 \leq tu_{max} \leq 5$. e, i Normalized rolling velocity versus time.

4.3.6 Particle–wall interaction regimens

As described, depending on the flow and particle properties, different regimens of particle–wall interaction can be documented: firmly adhering, rolling, sliding and not adhering particles. This is summarized in figs.4.13 and 4.14, where the rolling velocity u_{roll}/u_{max} and probability of adhesion Pa are presented as a function of the considered three different shapes—circular and elliptical with aspect ratios 2 and 3, ligand densities ρ_l ranging from 0.3 to 0.9, Reynolds numbers varying from 0.01 to 1.0, and bond strength σ equal to 1 (soft bond) and 2 (rigid bond). figure 4.13 presents a contour plot for the normalized rolling velocity u_{roll}/u_{max}, whereas fig.4.14 gives a contour plot for the probability of adhesion, Pa. This quantity is defined as the ratio between the number of active bonds and the maximum number of bonds that can be closed at any given time during the adhesion process and represents the likelihood of forming stable bonds at the particle–wall interface. The maximum number of bonds is readily calculated as a function of the particles geometry and orientation with respect to the wall. Both physical quantities (u_r and Pa) are affected in a similar fashion by the flow and particle properties. Specifically, low Reynolds numbers and high ligand densities (upper-left area) are associated with zero rolling velocities and firmly adhering particles. Indeed, under these conditions, the hydrodynamic dislodging forces are moderately low (low Re) and are readily balanced by the high adhesive interactions (high ρ_l). At the other extreme, high Reynolds numbers and low ligand densities (lower-right area) are associated with not adhering particles. Under these conditions, the hydrodynamic dislodging forces (high Re) cannot be balanced by the adhesive interactions (low ρ_l).

In between these two limiting conditions, particles are observed to move relatively to the substrate. With circular particles and elliptical particles at moderate ρ_l, continuous rolling over the wall is documented. On the other hand, with elliptical particles at high ρ_l, longitudinal sliding over the wall is observed. Note that rolling of elliptical particles is limited by their larger rotational inertia. However, longer bonds may facilitate rolling and slender particles as depicted in fig.4.15. Finally, adhesion is favored by stronger bonds in that, for fixed dislodging forces, higher σ are associated with lower ligand-receptor bond energies ($\propto F_b^2/\sigma$).

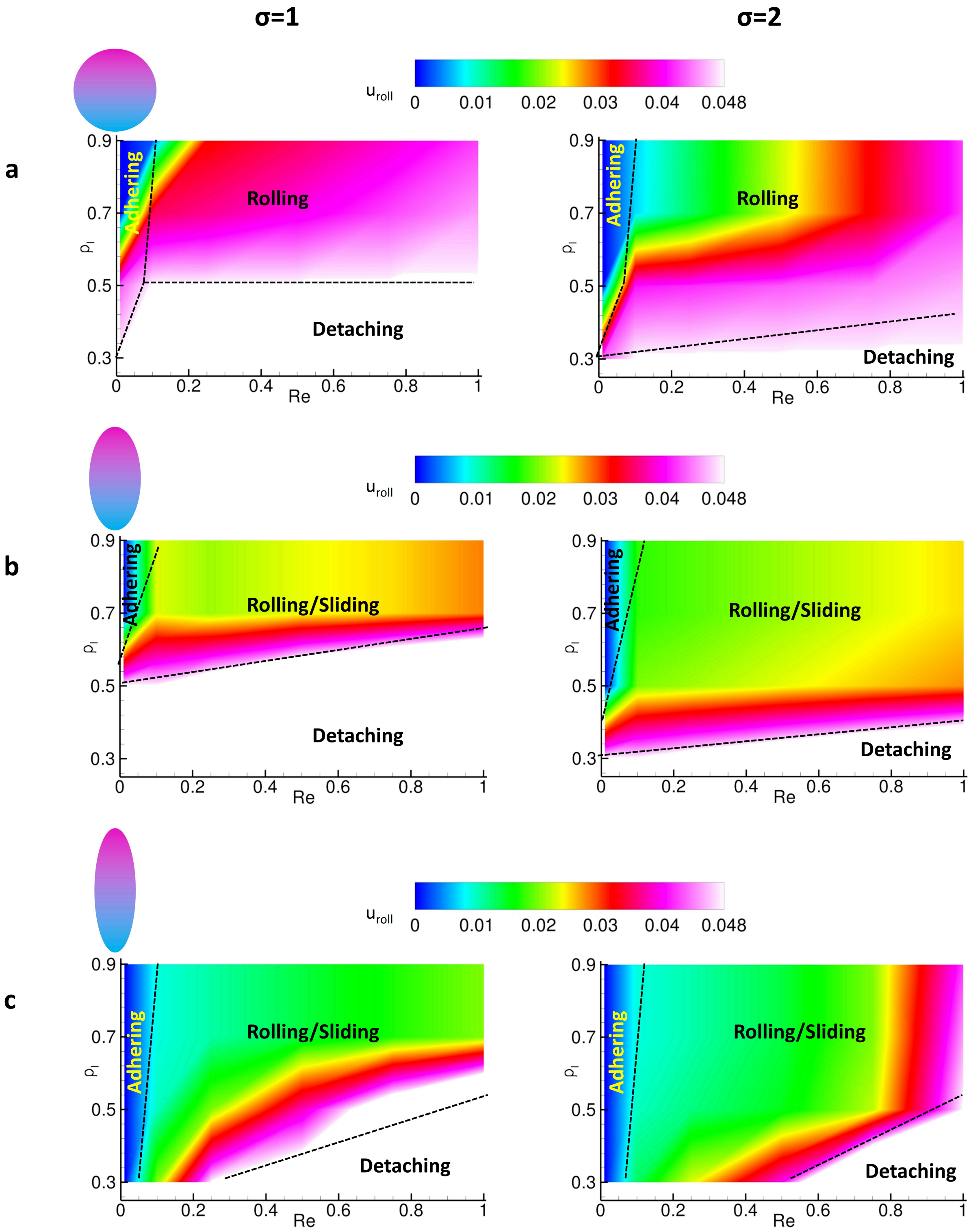

Figure 4.13: Contour plots for the rolling velocity. a Circular particle transport with soft ($\sigma = 1$) and rigid ($\sigma = 2$) ligand-recep- tor bonds. b Elliptical particle, with aspect ratio 2, transport with soft ($\sigma = 1$) and rigid ($\sigma = 2$) ligand-receptor bonds. c. Elliptical particle, with aspect ratio 3, transport with soft ($\sigma = 1$) and rigid ($\sigma = 2$) ligand-receptor bonds.

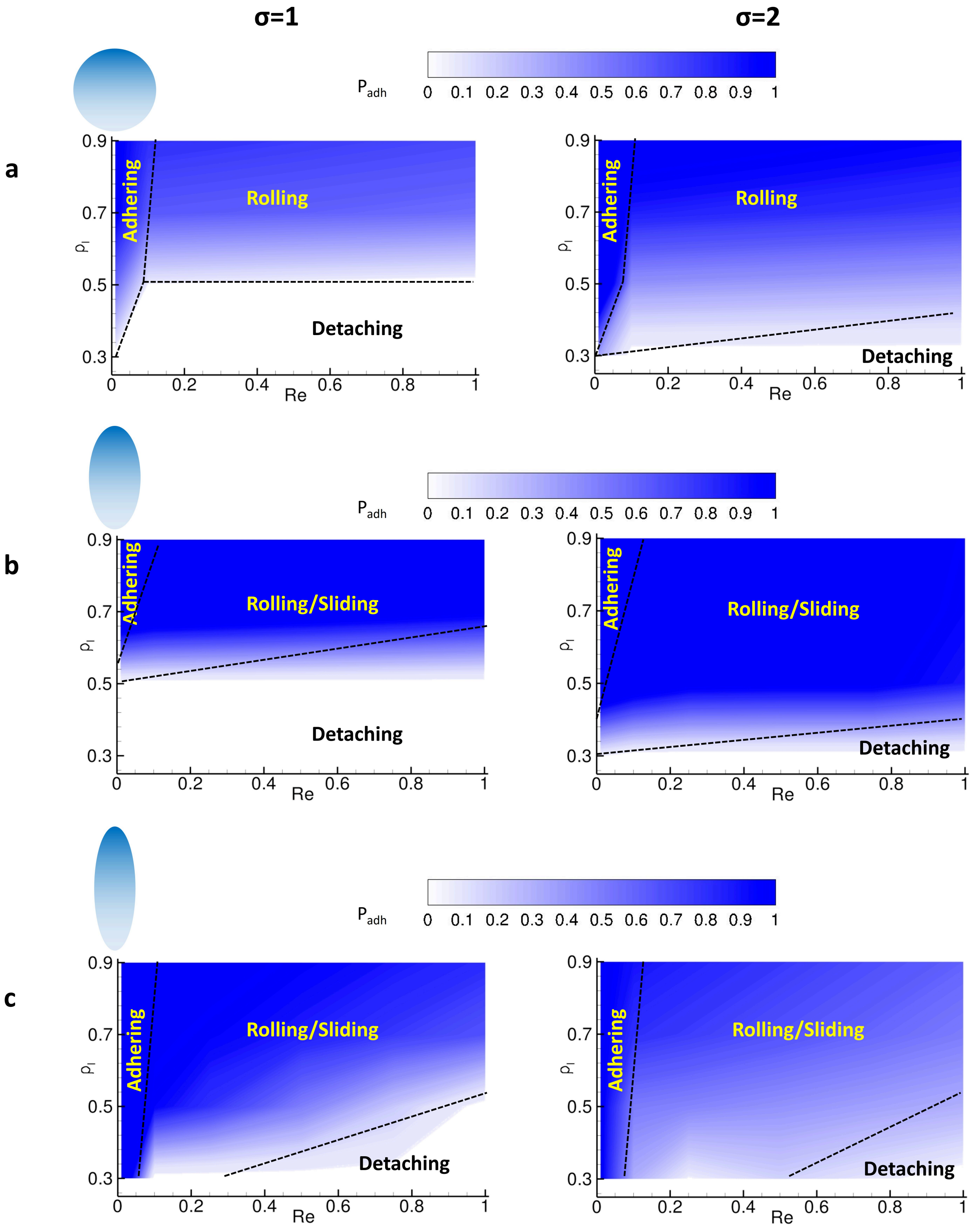

Figure 4.14: Contour plots for the probability of adhesion. a Circular particle transport with soft ($\sigma = 1$) and rigid ($\sigma = 2$) ligand-receptor bonds. b Elliptical particle, with aspect ratio 2, transport with soft ($\sigma = 1$) and rigid ($\sigma = 2$) ligand-receptor bonds. c Elliptical particle, with aspect ratio 3, transport with soft ($\sigma = 1$) and rigid ($\sigma = 2$) ligand-receptor bonds.

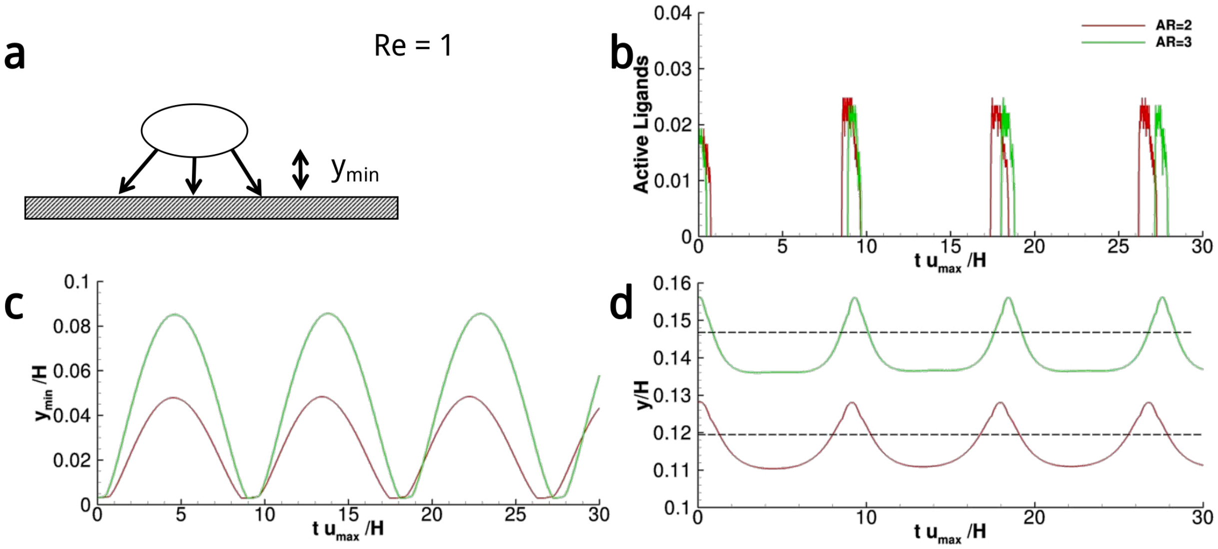

Figure 4.15: Vascular transport of elliptical particles with different critical bond length. a Schematic representation of the problem. b Active over total number of ligands versus time. c Particle separation distance from the wall versus time. d Centroid lateral position versus time.

4.4 Deformable capsule in shear flow

The last test of this work involves the simulation of a deformable sphere in a shear flow. The case was investigated by Lac et al.[53] the capsule subjected to hydrodynamic loads undergoes a deformation such as to change its shape. The capsule is considered a membrane fill of fluid. It reaches a steady shape around which the membrane rotates. This rotation was also described for red blood cells, and is called the tank-treading motion. The main dimensionless parameter is capillary number C_a defined as:

$$Ca = \frac{\rho \mu u_{max} D}{k_{el}} \tag{4.2}$$

where ρ is the reference density, μ is the viscosity, D is the diameter of the capsule and k_{el} is the elastic constant of the membrane. The test is conducted at a Reynolds number value of $Re = 0.01$ and capillary number $Ca = 0.5$. The lattice is a cubic box with a dimension of the side of L_{LBM} of 150. The capsule is positioned in the center of the latice box and has an initial diameter of $D = 40$. The comparison result is the evolution in time of the dimension ratio in the two direction orthogonal to vorticity direction in our setting it id $D_{yz} = D_y/D_z$. Figure 4.16 shows the results, and some explanation output image.

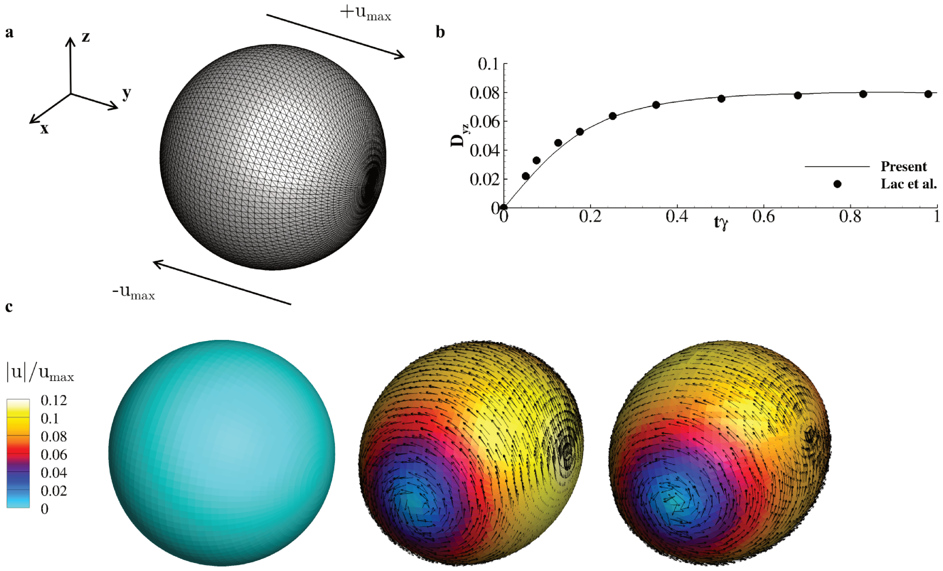

$t\gamma = 0.0$ $t\gamma = 0.25$ $t\gamma = 1.0$

Figure 4.16: Membrane Capsule Deformation in shear flow

Conclusions

This thesis describes the development work of a parallel three-dimensional model for the simulation of low Reynolds number flow to analyze dynamics of micro- and nano-particles navigating the flow. A set of models have been selected, according to their capabilities to solve the object problems, these models were implemented and tested.

- For the solution of the flow field, a parallel Lattice Boltzmann Method (LBM) have been developed onto the square (D2Q9) and the cubic lattice (D3Q19). The quality of the proposed model was validated against the literature results when computing a lid driven cavity with three different grid resolutions and Reynolds numbers.

- An Immersed Boundary (IB) method was implemented to simulate the presence of bodies surrounded by the flow.

- The same IB method has been used to compute the hydrodynamic stresses acting on an immersed rigid or deformable particle. The combined Lattice Boltzmann-Immersed Boundary method represents a good compromise between accuracy and computational burden into the simulation of rigid and deformable moving particles.

- Since the fluid–structure interaction has often been investigated through kinetic models, in which the immersed particles motion depends only on the velocity field surrounding them, the peculiar novelty and improvement is to consider a dynamic fluid–structure interaction method, for which the motion is solved considering the hydrodynamics forces exchanged through the body boundaries. This allows the author to study a number of biomedical cases with the accuracy that some physical phenomena require, as for example the deformation of blood borne cells.

- Several two–dimensional and three–dimensional tests have been shown the improvement of the final dynamics model.

- The method has been validated through several tests showing an excellent agreement with experimental data or already validated numerical solutions.

- Parallel implementation capabilities are tested and performance evaluated with good results in terms of speed and scalability.

Finally, the proposed method is a promising computational tool especially for biomedical applications.

Bibliography

[1] Ferziger J.H,,Peric M., *Computational Methods for Fluid Dynamics - Springer*, 2001

[2] Alessandro Coclite, Marco Donato de Tullio, Giuseppe Pascazio, and Paolo Decuzzi. A combined Lattice Boltzmann and Immersed boundary approach for predicting the vascular transport of differently shaped particles *Computers & Fluids*, 136:260–271, sep 2016.

[3] Loeb L.B. *The Kinetic Theory of Gases - Dover*, 1934

[4] Timm Kruger, Halim Kusumaatmaja, Alexandr Kuzmin, Orest Shardt, Goncalo Silva, and Erlend Magnus Viggen. *The Lattice Boltzmann Method: Principles and Practice* 2017.

[5] A. A. Mohammed *Lattice Boltzmann Method: Fundamentals and Engineering Applications with Computer Codes.* 2012.

[6] T.Kruger, F.Varnik, and D.Raabe. Particle stress in suspensions of soft objects *Philosophical transactions. Series A, Mathematical, physical, and engineering sciences*, 369(1945):2414–21, jun 2011.

[7] P.L. Bhatnagar, E.P. Gross, and M.Krook. A model for collision processes in gases. I. Small amplitude processes in charged and neutral one-component systems. *Physical Review*, 94(3):511–525, 1954.

[8] Martin Hecht and Jens Harting. Implementation of on-site velocity boundary conditions for D3Q19 lattice Boltzmann simulations. *Journal of Statistical Mechanics: Theory and Experiment*, 2010(01):P01018, jan 2010.

[9] Qisu Zou and Xiaoyi He. On pressure and velocity boundary conditions for the lattice Boltzmann BGK model. *Physics of Fluids*, 9(6):1591–1598, jun 1997.

[10] Charles S. Peskin. The immersed boundary method. *Acta Numerica*, 11:479–517, jan 2002.

[11] Marcos Vanella and Elias Balaras. A moving least squares reconstruction for embedded-boundary formulations. *Journal of Computational Physics*, 228(18):6617–6628, oct 2009.

[12] Zhaoli Guo, Chuguang Zheng, and Baochang Shi. Discrete lattice effects on the forcing term in the lattice Boltzmann method *Physical Review E*, 65(4):046308, apr 2002.

[13] Julien Favier, Alistair Revell, and Alfredo Pinelli. A Lattice Boltzmann-Immersed Boundary method to simulate the fluid interaction with moving and slender flexible objects. *Journal of Computational Physics*, 261:145–161, 2014.

[14] M.D. deTullio and G.Pascazio. A moving-least-squares immersed boundary method for simulating the fluid–structure interaction of elastic bodies with arbitrary thickness. *Journal of Computational Physics*, 325:201–225, nov 2016.

[15] Allen Van Gelder. Approximate Simulation of Elastic Membranes by Triangulated Spring Meshes. *Journal of Graphics Tools*, 3(2):21–41, jan 1998.

[16] Qun Zhang and Toshiaki Hisada. Studies of the strong coupling and weak coupling methods in FSI analysis. 2029(May 2004):2013–2029, 2013.

[17] Huilin Ye, Zhiqiang Shen, and Ying Li. Computational modeling of magnetic particle margination within blood flow through LAMMPS. *Computational Mechanics*, nov 2017.

[18] R.Benzi, S.Succi, and M.Vergassola. The lattice Boltzmann equation: theory and applications. *Physics Reports*, 222(3):145–197, dec 1992.

[19] Ahmed, F., et al., Internal Viscosity-Dependent Margination of Red Blood Cells in Microfluidic Channels. *Journal of biomechanical engineering*, 2018. 140(6): p. 061013. 33

[20] Fedosov, D.A., et al., Predicting human blood viscosity in silico. *Proc Natl Acad Sci U S A*, 2011. 108(29): p. 11772-7.

[21] Hossain, S.S., T.J. Hughes, and P. Decuzzi, Vascular deposition patterns for nanoparticles in an inflamed patient-specific arterial tree. *Biomech Model Mechanobiol*, 2014. 13(3): p. 585-97.

[22] Nabil, M., P. Decuzzi, and P. Zunino, Modelling mass and heat transfer in nano-based cancer hyperthermia. *R Soc Open Sci*, 2015. 2(10): p. 150447.

[23] Stone, H.A., A.D. Stroock, and A. Ajdari, Engineering flows in small devices: microfluidics toward a lab-on-a-chip. *Annu. Rev. Fluid Mech.*, 2004. 36: p. 381-411.

[24] Sun, X. and M. Sakai, Numerical simulation of two-phase flows in complex geometries by using the volume-of-fluid/immersed-boundary method. *Chemical Engineering Science*, 2016. 139: p. 221-240.

[25] Maiti, R. and K. Nigam, Gas-liquid distributors for trickle-bed reactors: a review. *Industrial & Engineering Chemistry Research*, 2007. 46(19): p. 6164-6182.

[26] Lai, M.-C., Y.-H. Tseng, and H. Huang, An immersed boundary method for interfacial flows with insoluble surfactant. *Journal of Computational Physics*, 2008. 227(15): p. 7279-7293.

[27] Ihitfield, C.A. and R.J. Hawkins, Immersed boundary simulations of active fluid droplets. *PloS one*, 2016. 11(9): p. e0162474.

[28] Patel, H., et al., A coupled Volume of Fluid and Immersed Boundary Method for simulating 3D multiphase flows with contact line dynamics in complex geometries. *Chemical Engineering Science*, 2017. 166: p. 28-41.

[29] Navarro-Jiménez, J.M., et al., Large deformation frictional contact analysis with immersed boundary method. *Computational Mechanics*, 2018: p. 1-18.

[30] Svenning, E., A. Mark, and F. Edelvik, Simulation of a highly elastic structure interacting with a two-phase flow. *Journal of Mathematics in Industry*, 2014. 4(1): p. 7.

[31] Tian, F.-B., et al., Fluid–structure interaction involving large deformations: 3D simulations and applications to biological systems. *Journal of computational physics*, 2014. 258: p. 451-469.

[32] Peskin, C.S., Flow patterns around heart valves: a digital computer method for solving the equations of motion. 1972, Sue Golding Graduate Division of Medical Sciences, Albert Einstein College of Medicine, Yeshiva University.

[33] Connell, B.S.H. and D.K.P. Yue, Flapping dynamics of a flag in a uniform stream. *Journal of Fluid Mechanics*, 2007. 581: p. 33-68.

[34] Sawada, T. and T. Hisada, Fluid–structure interaction analysis of the two-dimensional flag-in-wind problem by an interface-tracking ALE finite element method. Computers & Fluids, 2007. 36(1): p. 136-146.

[35] Peskin, C.S., Numerical analysis of blood flow in the heart. *Journal of computational physics*, 1977. 25(3): p. 220-252.

[36] Kruger, H., Computer simulation study of collective phenomena in dense suspensions of red blood cells under shear. 2012: *Springer Science & Business Media*.

[37] Feng, Z.G. and E.E. Michaelides, The immersed boundary-lattice Boltzmann method for solving fluid-particles interaction problems. *Journal of Computational Physics*, 2004. 195(2): p. 602-628. 3520.

[38] Zhang, J., P.C. Johnson, and A.S. Popel, An immersed boundary lattice Boltzmann approach to simulate deformable liquid capsules and its application to microscopic blood flows. *Physical biology*, 2007. 4(4): p. 285.

[39] De Rosis, A., S. Ubertini, and F. Ubertini, A Comparison Between the Interpolated Bounce-Back Scheme and the Immersed Boundary Method to Treat Solid Boundary Conditions for Laminar Flows in the Lattice Boltzmann Framework. *Journal of Scientific Computing*, 2014. 61(3): p. 477-489.

[40] M. Napolitano, G.Pascazio, A numerical method for the vorticity-velocity Navier-Stokes equations in two and three dimensions. *Computers & Fluids* ,1991, Vol. 19, Issues 3–4,p. 489-495

[41] Haibo Huang, Xin Yang, Manfred Krafczyk and Xi-Yun Lu, Rotation of spheroidal particles in Couette flows. *J. Fluid Mech.*, 2012, vol. 692, pp. 369–394.

[42] AIDUN C. K., LU Y. & D ING E. Direct analysis of particulate suspensions with inertia using the discrete Boltzmann equation. *J. Fluid Mech.*,1998, 373, 287–311.

[43] ZETTNER C. M., YODA M. Moderate-aspect-ratio elliptical cylinders in simple shear with inertia. *J. Fluid Mech.*, 2001 442, 241–266.

[44] Jefferey G.B. The motion of ellipsoidal particles immersed in a viscous fluid. *Proc. R. Society London* 1922. A 102, 161-179.

[45] A. ten Cate, C.H. Nieuwstad, J.J. Derksen, and Van den Akker H.E.A. Particle imaging velocimetry experiments and lattice-boltzmann simulations on a single sphere settling under gravity. *Physics of Fluids*,2002, 14:4012–4025.

[46] F. Abraham. Functional dependence of drag coefficient of a sphere on Reynolds number. *Physics of Fluids*,1970, 13:2194.

[47] M. Tanaka, S. Wada, M. Nakamura, Computational Biomechanics-Springer, 2012.

[48] A. Van Gelder, Approximate simulation of elastic membranes by triangulated spring meshes. *J. Graph. Tools 3*, 1998 21–42.

[49] Y. Kantor, D.R. Nelson, Phase transitions in flexible polymeric surfaces. *Phys. Rev.*,1987 A 36 4020–4032.

[50] J. Li, M. Dao, C.T. Lim, S. Suresh, Spectrin-level modeling of the cytoskeleton and optical tweezers stretching of the erythrocyte. *Biophys. J.*,2005, 88 3707–3719.

[51] Nakamura, M., S. Bessho, and S. iada, Spring-network-based model of a red blood cell for simulating mesoscopic blood flow. *Int J Numer Method Biomed Eng*, 2013. 29(1): p. 114-28.

[52] Fedosov, D.A., B. Caswell, and G.E. Karniadakis, Systematic coarse-graining of spectrin-level red blood cell models. *Comput Methods Appl Mech Eng*, 2010. 199(29- 32): p. 1937-1948.

[53] Lac E., Barthes-Biesel D., PeleKasis N.A., Tsampoulos J., Spherical capsules in three-dimensional unbounded Stokes flows: effect of the membrane constitutive law and onset of buckling *J. Fluid Mech.*, 2004, vol. 516, pp. 303–334.

[54] Fadlun, E.A., et al., Combined immersed-boundary finite-difference methods for three-dimensional complex flow simulations. *Journal of Computational Physics*, 2000. 161(1): p. 35-60.

[55] Coclite, A., et al., Predicting different adhesive regimens of circulating particles at blood capillary walls. *Microfluidics and Nanofluidics*, 2017. 21(11): p. 168.

[56] A.Coclite, S.Ranaldo, M.D. de Tullio b, P. Decuzzi and G. Pascazio, Kinematic and dynamic forcing strategies for predicting the transport of inertial capsules via a combined lattice Boltzmann – Immersed Boundary method. *Computers and Fluids*, 180 (2019) pp. 41–53.

[57] Coclite, A., G. Gonnella, and A. Lamura, Pattern formation in liquid-vapor systems under periodic potential and shear. *Phys Rev E Stat Nonlin Soft Matter Phys*, 2014. 89(6): p. 063303.

[58] Liu, G.-R. and Y.-T. Gu, An introduction to meshfree methods and their programming. *Springer Science & Business Media*, 2005.

[59] uian, Y.H., D. Dhumieres, and P. Lallemand, Lattice Bgk Models for Navier-Stokes Equation. *Europhysics Letters*, 1992. 17(6bis): p. 479-484.

[60] Shan, X.i., X.F. Yuan, and H.D. Chen, Kinetic theory representation of hydrodynamics: a way beyond the Navier-Stokes equation. *Journal of Fluid Mechanics*, 2006. 550: p. 413-441.

[61] De Rosis, A., S. Ubertini, and F. Ubertini, A partitioned approach for two-dimensional fluid-structure interaction problems by a coupled lattice Boltzmann-finite element method with immersed boundary. *Journal of Fluids and Structures*, 2014. 45: p. 202- 215.

[62] Suzuki, K., K. Minami, and T. Inamuro, Lift and thrust generation by a butterfly-like flapping wing-body model: immersed boundary-lattice Boltzmann simulations. *Journal of Fluid Mechanics*, 2015. 767: p. 659-695.

[63] Iang, Y., et al., An immersed boundary-lattice Boltzmann flux solver and its 37applications to fluid-structure interaction problems. *Journal of Fluids and Structures*, 2015. 54: p. 440-465.

[64] Peskin, C.S., The immersed boundary method. Acta numerica, 2002. 11: p. 479-517. 37. Pozrikidis, C., Effect of membrane bending stiffness on the deformation of capsules in simple shear flow. *Journal of Fluid Mechanics*, 2001. 440: p. 269-291.

[65] Skalak, R., et al., Strain energy function of red blood cell membranes. *Biophys J*, 1973. 13(3): p. 245-64.

[66] Dao, M., J. Li, and S. Suresh, Molecularly based analysis of deformation of spectrin network and human erythrocyte. *Materials Science & Engineering C-Biomimetic and Supramolecular Systems*, 2006. 26(8): p. 1232-1244.

[67] Fedosov, D.A., et al., Multiscale modeling of red blood cell mechanics and blood flow in malaria. *PLoS Comput Biol*, 2011. 7(12): p. e1002270.

[68] Guyot, Y., et al., Immersed Boundary Models for Quantifying Flow-Induced Mechanical Stimuli on Stem Cells Seeded on 3D Scaffolds in Perfusion Bioreactors. *PLoS Comput Biol*, 2016. 12(9): p. e1005108.

[69] Ye, S.S., et al., Two-dimensional strain-hardening membrane model for large 38deformation behavior of multiple red blood cells in high shear conditions. *Theor Biol Med Model*, 2014. 11(1): p. 19.

[70] Buxton, G.A., et al., Newtonian fluid meets an elastic solid: coupling lattice Boltzmann and lattice-spring models. *Phys Rev E Stat Nonlin Soft Matter Phys*, 2005. 71(5 Pt 2): p. 056707.

[71] Ahlrichs, P. and B. Dunweg, Lattice-Boltzmann simulation of polymer-solvent systems. *International Journal of Modern Physics C*, 1998. 9(8): p. 1429-1438.

[72] Kruger, T., F. Varnik, and D. Raabe, Efficient and accurate simulations of deformable particles immersed in a fluid using a combined immersed boundary lattice Boltzmann finite element method. *Computers & Mathematics with Applications*, 2011. 61(12): p. 3485-3505.

[73] Bagchi, P., Mesoscale simulation of blood flow in small vessels. *Biophysical journal*, 2007. 92(6): p. 1858-1877.

[74] Mittal, R. and G. Iaccarino, Immersed boundary methods. *Annu. Rev. Fluid Mech.*, 2005. 37: p. 239-261.

[75] Sui, Y., et al., Transient deformation of elastic capsules in shear flow: effect of 39membrane bending stiffness. *Physical Review E*, 2007. 75(6): p. 066301.

[76] Pozrikidis, C., Numerical simulation of the flow-induced deformation of red blood cells. *Annals of Biomedical Engineering*, 2003. 31(10): p. 1194-1205.

[77] Shi, L., T.-i. Pan, and R. Glowinski, Deformation of a single red blood cell in bounded Poiseuille flows. *Physical Review E*, 2012. 85(1): p. 016307.